Winter 2002

Finite Element Modal Formulation for Panel Flutter at Hypersonic Speeds and Elevated Temperatures

Guangfeng Cheng
Old Dominion University

FINITE ELEMENT MODAL FORMULATION FOR PANEL FLUTTER

AT HYPERSONIC SPEEDS AND ELEVATED TEMPERATURES

by

Guangfeng Cheng
B.S. July 1992, Beijing University of Aeronautics and Astronautics
M.S. April 1995, Beijing University of Aeronautics and Astronautics

A Dissertation Submitted to the Faculty of
Old Dominion University in Partial Fulfillment of the
Requirement for the Degree of

DOCTOR OF PHILOSOPHY

ENGINEERING MECHANICS

OLD DOMINION UNIVERSITY
December 2002

Approved by:

_____
Chuh Mei (Director)

_____
Colin Britcher (Member)

_____
Gene Hou (Member)

ABSTRACT

FINITE ELEMENT MODAL FORMULATION FOR PANEL FLUTTER
AT HYPERSONIC SPEEDS AND ELEVATED TEMPERATURES

Guangfeng Cheng
Old Dominion University, 2002
Director: Dr. Chuh Mei

A finite element time domain modal formulation for analyzing flutter behavior of aircraft surface panels in hypersonic airflow has been developed and presented for the first time. Von Karman large deflection plate theory is used for description of the structural nonlinearity and third order piston theory is employed to account for the aerodynamic nonlinearity. The thermal loadings of uniformly distributed temperature and temperature gradients across the panel thickness are incorporated into the finite element formulation. By applying the modal reduction technique, the number of governing equations of motion is reduced dramatically so that the computational time of direct numerical integration is dropped significantly. All possible types of panel behavior, including flat, buckled but dynamically stable, limit cycle oscillation (LCO), periodic motion, and chaotic motion can be observed and analyzed. As examples of the applications of the proposed methodology, flutter responses of isotropic, specially orthotropic and laminated composite panels are investigated. Special emphasis is put on the boundary between LCO and chaos, as well as the routes to chaos. A systematic mode filtering procedure that helps mode selection without specific knowledge of the complex mode shapes is presented and illustrated. Influences of aerodynamic parameters, including aerodynamic damping and Mach number, on the panel flutter responses are studied. The importance of nonlinear aerodynamic terms is examined in detail. The

supporting conditions and panel aspect ratio on the onset condition of chaos are also investigated as an illustration of optimization among different design options.

Several mathematical tools, including the time history, phase plane plot, Poincaré map, and bifurcation diagram are employed in the chaos study. The largest Lyapunov exponent is also evaluated to assist in detection of chaos. It is found that at low or moderately high nondimensional dynamic pressures, the fluttering panel typically takes a period-doubling route to evolve into chaos, whereas at high nondimensional dynamic pressure, the route to chaos generally involves bursts of chaos and rejuvenations of periodic motions. Various bifurcation behaviors, such as the Hopf bifurcation, pitchfork bifurcation, and transcritical bifurcation, are observed.

On the basis of the successful applications presented, the proposed finite element time domain modal formulation and the mode filtering procedure have proven to be an efficient and practical design tool for designers of hypersonic vehicles.

ACKNOWLEDGMENTS

I would like to express my deepest gratitude and appreciation to my advisor, Dr. Chuh Mei, for his invaluable guidance, encouragement, and advice on research and life attitudes. I deem it a great fortune to have such a knowledgeable and warmhearted professor as my advisor.

Special thanks are also extended to my Guidance and Dissertation Committee members, Dr. Jeng-Jong Ro, Dr. Donald Kunz, Dr. Colin Britcher, and Dr. Gene Hou, for their suggestions and kindly help.

I am indebted to all my family members. I thank my parents for understanding and supporting me to travel such a great distance to America to learn science. To my wife, Chunhua, I sincerely appreciate and cherish your neverending love and care.

It is also my great pleasure to thank my colleagues and good friends, Bin Duan, Jean-Michel Dhainaut, and Xinyun Guo, for all their discussions and support.

Guangfeng Cheng

December 2002

TABLE OF CONTENTS

LIST OF TABLES

LIST OF FIGURES

LIST OF SYMBOLS

a, b	panel length and width
$\bar{a}, \bar{b}$	BFS element length and width
[A]	in-plane stiffness matrix
[A1]	linear aerodynamic influence matrices
[A2]	quadratic aerodynamic influence matrices
[a], [A_a]	element and system aerodynamic influence matrices
[$\bar{A}$]	modal aerodynamic influence matrices
[B]	coupling stiffness matrix
C_a	aerodynamic damping coefficient
[C]	interpolation function matrix
[D]	bending stiffness matrix
E	Young's modulus
g_a	nondimensional aerodynamic damping
G	shear modulus
[g], [G]	element and system aerodynamic damping matrices
[G1]	linear aerodynamic damping matrices
[G2]	quadratic aerodynamic damping matrices
[$\bar{G}$]	modal aerodynamic damping matrix
H	panel thickness
[H]	displacement function matrix
[k], [K]	element and system stiffness matrices
[$\bar{K}$]	modal linear stiffness matrix

$[K_{qq}]$	modal nonlinear stiffness matrices
L	panel length
M	Mach number
M_r	Flow parameter, $M_\infty (h/a)$
M_∞	free stream Mach number
[m], [M]	element and system mass matrices
$[\overline{M}]$	modal mass matrix
{N}, {M}	force and moment resultant vectors
[n1], [N1]	element and system first-order nonlinear stiffness matrices
[n2], [N2]	element and system second-order nonlinear stiffness matrices
p_a	aerodynamic pressure
p_∞	undisturbed pressure of gas
q	dynamic pressure / modal coordinate
{p}, {P}	element and system force vectors
{q}	modal coordinate vector
[Q]	lamina reduced stiffness matrix
$[\overline{Q}]$	transformed lamina reduced stiffness matrix
r	panel thickness-width ratio
To	average temperature
T_1	temperature gradient across panel thickness
u, v	in-plane displacements
V	airflow velocity
w, W	element and system panel transverse deflections

x, y, z	Cartesian coordinates
{X}	state vector

Greek symbols

α	thermal expansion coefficient
β	$\sqrt{M_\infty^2 - 1}$
γ	ratio of specific heat, $\gamma = 1.4$
η	modal participation factor
Δ	incremental value
{ε}	strain vector
ϕ	fiber orientation angle
{ϕ}, {Φ}	element and system eigenvector
[Φ]	modal matrix
{κ}	bending curvature vector
λ	nondimensional dynamic pressure
μ	air-panel mass ratio
ν_{12}, ν_{21}	Poisson's ratios
θ	lamination angle
[θ]	slope matrix
ρ	mass density
{σ}	stress vector
ω	frequency

Subscripts

a	air
b	bending
cr	critical
m	membrane / composite matrix
Nb	stiffness matrices due to $\{N_b\}$
NL	nonlinear
Nm	stiffness matrices due to $\{N_m\}$
NΔT	stiffness matrices due to $\{N_{\Delta T}\}$
u, v, w	in-plane and transverse displacements
ΔT	thermal

CHAPTER I

INTRODUCTION

1.1 Preview of Panel Flutter

The very first observation of panel flutter can be traced back to the mid-1940s. The German V-2 rockets encountered flutter problems that resulted in shaking off of the metal skin when the rockets flew at supersonic speed. Structural failures due to flutter have been reported extensively in aircraft, space shuttles, missiles, rockets, and bridges, whenever high speed airflow is involved.

The panel flutter phenomenon is typically self-excited or self-sustained oscillations of the external skin of a flight vehicle when exposed to airflow along its surface. The origin of this kind of structural instability is the interaction between a fluid, the airflow, and a solid, the panel. The unsteady aerodynamic pressure does work on the structure and this leads to frequency coalescence, a specific symbol of flutter, between certain vibration modes of the panel. Resonance of the coalesced modes amplifies the vibration amplitude of the panel so that the panel is fluttering by way of limit cycle oscillations (LCO) or chaotically.

Study of panel flutter falls into the domain of aeroelasticity (Bisplinghoff et al.[1]) in sense that it results from the interactions among inertial, aerodynamic, and elastic forces. Besides panel flutter, there exists another flutter behavior, called wing flutter, which

---

The journal model used for this dissertation is the *AIAA Journal.*

addresses flutter of thin panel/shell wing due to aerodynamic pressure on both sides of the structure. Panel flutter occurs in structures like aircraft and spacecraft skin panels that experience aerodynamic pressure at one side with the other side adjacent to a cavity, as shown in Fig. 1.1. Fundamental theories and physical understanding of panel flutter can be found in many books, such as Dowell [2], Librescu [3], and some of the review and survey papers in literature that followed.

Deformed panel shape

Airdynamic press

Airflow

Cavity
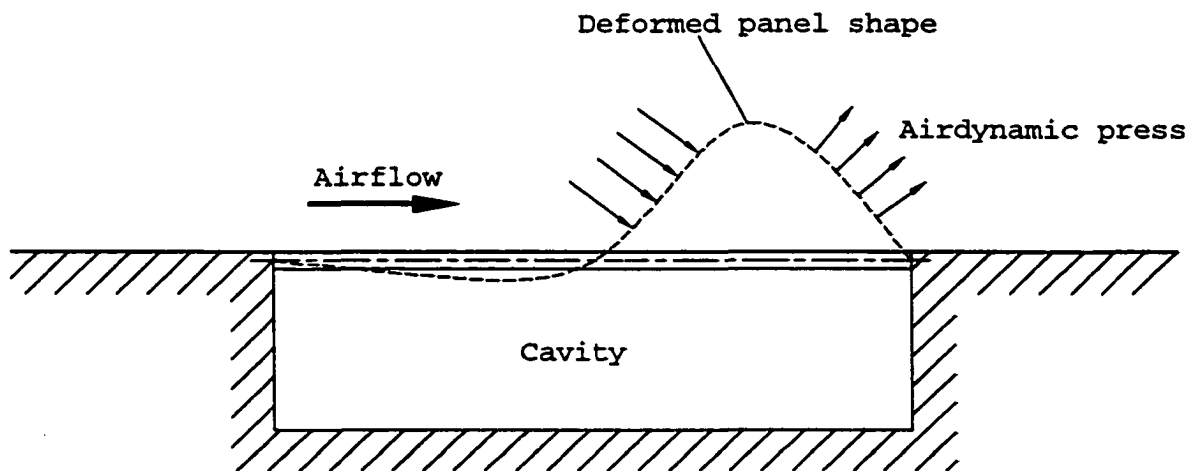
Fig. 1.1 Illustration of panel flutter

Prevention or suppression of flutter has long been recognized as an essential design criterion in high speed flight vehicles, such as the High-Speed Civil Transport (HSCT), the National Aero-Space Plane (NASP), the X-33 Advanced Technology Demonstrator, the Reusable Launch Vehicle (RLV), the Joint Strike Fighter (JSF), the X-38 Spacecraft, the X-43 Hyper-X program and recently the Quiet Supersonic Platform (QSP) program sponsored by DARPA. Extensive research on flutter analyses and related experiments have provided a series of tools for designers. Nowadays, due to dramatic advances in computer hardware and software, designers depend more and more on

analytical/numerical tools. The strong demand for more powerful, accurate and efficient numerical computational methods for flutter analysis initiated resurgent research activities.

From transonic to supersonic, from supersonic to hypersonic, the enhancement in flight speed is an ultimate goal of aircraft/spacecraft design. For panel flutter analysis of a vehicle flying at hypersonic speed, most of the experiences and expertise accumulated by generations of aeroelasticians through supersonic panel flutter analyses can be inherited and exploited. The major topics, such as choices of aerodynamic theory, linear/nonlinear structural dynamics model, analytical/numerical approach to apply, considerations of effects from system parameters, and so on, remain the same for hypersonic flutter analysis as for supersonic flutter analysis. The literature survey following serves as a brief summary of pertinent research and also exposes the necessity of the work carried out in the rest of this dissertation research.

1.2 Literature Survey

1.2.1 Flutter Analysis

Theoretical and experimental studies of panel flutter started in the 1950s. Research and findings conducted in the early stage were summarized by Fung [4] and Johns [5, 6]. In a later survey paper by Dowell [7], the author grouped a voluminous theoretical literature on panel flutter into four basic categories based upon the structural and aerodynamic theories employed, as shown in Table 1.1. The table is taken from a recent review paper by Mei et al. [8]. Augmentation of the fifth type of analysis is attributed to Gary and Mei [9] on consideration of hypersonic panel flutter analysis theory proposed

by McIntosh [10]. A review on the specific topic of hypersonic panel flutter analysis was given by Reed et al. [11] in support of the NASP program. There are also review papers about certain types of flutter analysis listed in Table 1.1, such as the review papers concerning application of the finite element method to type 3 and type 5 panel flutter analysis by Bismarc-Nasr [12,13] and a review of various analytical methods including the finite element approach for nonlinear supersonic panel flutter type 3 analysis by Zhou et al. [14].

Table 1.1 Panel Flutter Analysis Categories

Type	Structure Theory	Aerodynamic Theory	Range of Mach No.
1	Linear	Linear Piston	$\sqrt{2} < M_\infty < 5$
2	Linear	Linearized Potential Flow	$1 < M_\infty < 5$
3	Nonlinear	Linear Piston	$\sqrt{2} < M_\infty < 5$
4	Nonlinear	Linearized Potential Flow	$1 < M_\infty < 5$
5	Nonlinear	Nonlinear Piston	$M_\infty > 5$
6	Nonlinear	Euler or Navier-Stokes Equations	Transonic, Supersonic, and Hypersonic

Because of the mathematical simplicity of linear structural theory, the majority of preliminary flutter analysis belongs to linear panel flutter analysis of type 1 or type 2. Representative works are Hedgepeth [15], Dugundji [16], and Cunningham [17]. Clearly, as indicated in the review paper by Dowell [7], panel flutter analysis using linear structural theory is incapable of accounting for structural nonlinearities. Linear structural

theory indicates that there is a critical dynamic pressure above which the panel motion becomes unstable and grows exponentially with time. In reality, when the vibration amplitude of the panel gets large, the panel extends also. This in-plane stretching introduces significant membrane tensile forces (Woinowsky-Krieger [18]) so that the bending of the panel is restrained within a limited range, which is termed as limit cycle oscillation. This stabilizing effect due to nonlinear membrane stresses must be addressed when the amplitude of LCOs is of interest. Linear panel flutter analysis usually is only used to predict flutter boundary and frequency. Some researchers, such as Eisley [19], Houboult [20], Fung [21], and Bolotin [22], employed nonlinear structural theory in the determination of flutter boundaries. Since LCO is not involved, such analysis is actually partial nonlinear. Full nonlinear panel flutter analysis can be found in a vast amount of literature. The von Karman large deflection theory [23] is widely used to account for geometric nonlinearity, and has been successfully applied to the nonlinear panel flutter problem. Despite the comparative consistency on which nonlinear structural theory to use, various linear aerodynamic theories have been employed. The most popularly adopted is the quasi-steady first order piston theory [24], which is applicable for flow speed of Mach number greater than $\sqrt{2}$. Dowell [25-27] applied the full linearized potential flow aerodynamics for LCO behavior of plates in airflow with Mach number close to one. The quasi-static Ackeret aerodynamic theory, also known as the static strip theory (Cunningham [17]), was applied to nonlinear supersonic flutter analysis by Fralich [28].

Linear flutter analysis generally solves for the stability boundary through eigenanalysis, whereas nonlinear flutter analysis needs special treatment. The prevailing

analysis approaches include direct numerical integration, the harmonic balance method and the pertubation method. The very first application of direct numerical integration was due to Dowell [26, 27] in study of nonlinear oscillations of simply supported, in-plane elastically restrained, fluttering plates. Ventres [29] investigated the nonlinear flutter behavior of clamped plates also by direct numerical integration. The procedures of this approach include first applying the Galerkin's method in the spatial domain to the nonlinear partial differential equations of motion to yield a set of coupled nonlinear ordinary differential equations in time. Then the time numerical integration is conducted to simulate the flutter response. The Rayleigh-Ritz method, which requires that the assumed modes satisfy only the geometric boundary conditions, is another approach for approximate spatial expansion of the plate deflection. The harmonic balance method has also been successfully applied to nonlinear flutter analysis by some investigators [30-33]. This method, compared to direct numerical integration, requires less computation time but it is extremely tedious to implement. The perturbation method was introduced to nonlinear flutter analysis by Morino et al. [34-36]. Good agreement between the results obtained by perturbation methods and those by the harmonic balance method was found by Kuo et al. [37]. In general, for both harmonic balance and perturbation methods, the panel deflection is represented in terms of two to six normal modes.

Some intrinsic limitations obstruct the application of the abovementioned analytical approaches to more extensive analysis practices. For instance, Galerkin's method or the Ralyeigh-Ritz method requires reasonable assumptions about normal mode shape functions, which must satisfy the boundary conditions of the panel. Generally, panels with simple support conditions, such as simply supported or clamped boundaries, are

mathematically easy to deal with. For complex support conditions, even for a combination of simple support conditions, suitable displacement functions may not exist or are too complicated to manipulate. The anisotropic material properties of composite materials that have extensive engineering applications also make it difficult to analyze nonlinear flutter using analytical methods. In view of these problems, researchers have resorted to numerical methods such as the finite element method (FEM). Extension of FEM to linear panel flutter analysis was initiated by Olson [38] and followed by many researchers [39-42]. The application of FEM to nonlinear panel flutter started in 1977 by Mei [43] in study of 2-D panel flutter with membrane inertia neglected. The FEM for nonlinear flutter analysis can be further categorized as the finite element frequency domain formulation and the time domain formulation. The frequency domain formulation is well developed and widely applied in solving the flutter boundary (eigenanalysis) and studying harmonic LCO. Mei and Rogers [44] incorporated the supersonic flutter analysis module for a 2-D panel into the NASTRAN code. Rao and Rao [45] investigated the supersonic flutter of 2-D panels with ends restrained elastically against rotation. Mei and Weidman [46] were the first to extend the study to the 3-D panel LCO. Effects of damping, aspect ratios, initial in-plane forces, and boundary conditions were examined. Flutter of a 3-D panel was further investigated by Mei and Wang [47], and Han and Yang [48] using triangular plate finite elements. For study of harmonic LCO, a linearized updated mode with a nonlinear time function (LUM/NTF) approximation solution procedure proposed by Gray and Mei [9] is usually employed [49-51]. In comparison, the time domain formulation that involves numerical integration is less documented in nonlinear panel flutter analysis. The major obstacles to implementation of the time

domain formulation are (Green and Killey [52] and Robinson [53]): (i) the large number of degrees of freedom (DOF) of the system, (ii) the nonlinear stiffness matrices have to be assembled and updated from the element nonlinear stiffness matrices at each time step, and (iii) the time step of integration has to be extremely small. Zhou et al. [54] presented a finite element time domain modal formulation making use of the modal truncation technique in nonlinear panel flutter analysis. Flutter responses of isotropic and composite panels under combined supersonic aerodynamic pressure and thermal loading were investigated. Five types of panel behavior – flat, buckled, LCO, periodic but nonharmonic, and chaotic motions – were determined through numerical integration of governing equations of motion in modal coordinates.

As mentioned earlier, nonlinearities involved with panel flutter arise from two aspects: the structural and aerodynamic points of view. For flight vehicles operating in the hypersonic regime, unsteady nonlinear aerodynamic theories are more applicable to the problem. Aerodynamic nonlinearity was first considered in conjunction with structural nonlinearity by Mcintosh [10, 55] and Eastep and McIntosh [56] in panel flutter analysis of simply supported 2-D and 3-D panels in hypersonic airflow. The von Karman large deflection theory was used to address structural nonlineraity. Two nonlinear aerodynamic terms, $(\partial w / \partial x)^2$ and $((\partial w / \partial x)(\partial w / \partial t))$, taken from the 3rd order piston theory, were added to the linear piston theory to address the aerodynamic nonlinearity. The Rayleigh-Ritz approximation is employed in a modal representation of the panel transverse deflection. The nonlinear modal equations of motion are then integrated in the time domain until observation of LCO. Major findings include: (1) the two nonlinear terms proved to be the most important sources of aerodynamic nonlinearity, (2) the

nonlinear aerodynamic loading introduced a bias of panel motion toward the cavity that could be attributed to the overpressurization effects of the additional nonlinear pressure terms, (3) aerodynamic loading has no effects on limit cycle frequency and little effect on panel stress, (4) contrary to the stabilizing effect from the structural nonlinear membrane stress on panel motion, nonlinear aerodynamic loading plays a destabilizing role. The interplay between these two mechanisms distinguishes panel flutter at hypersonic speeds from that at supersonic speeds. For some system parameters, aerodynamic nonlinearities decrease the critical dynamic pressure for panel flutter hence produce a "soft spring" effect on the prediction of the stability boundary. A rather later study on 2-D panel flutter in hypersonic flow by Gray and Mei [57] using FEM confirmed conclusions 1, 2, and 4. The third order piston theory was used for aerodynamic pressure and the significance of the nonlinear terms was investigated in detail. Gray and Mei developed the LUM/NTF method, which is a generic finite element frequency domain LCO solver. The same solution procedure was then extended to panel flutter analysis of a 3-D composite panel at hypersonic speeds in their later work [9]. Effects of panel support conditions, panel thickness to length ratio, panel aspect ratio, and number of laminate layers on LCO amplitude were studied. Good agreement between the flutter analysis by the proposed finite element frequency domain approach and the existing analytical methods was found.

A few more contributions on hypersonic flow panel flutter analysis have been made by other groups of investigators. Bein et al. [58] studied the hypersonic flutter of simply support curved shallow orthotropic panels with uniform temperature distribution due to aerodynamic heating. Coupled nonlinear panel flutter modal equations were obtained using Galerkin's mehod, and direct time numerical integration was conducted to compute

the LCO amplitudes. The unsteady aerodynamic pressure from third order piston theory was compared to that from the solutions of Euler equations and good agreement was found. Nydick et al. [59] continued the study on hypersonic flutter of curved panels by considerations of more comprehensive temperature distributions (temperature is a function of all three coordinates, x, y, and z), presence of shocks in the flow, and an alternative representation of aerodynamic loading. The aerodynamic load is given by third order piston theory and it is compared with pressure distributions solved from the Euler equations and from the Navier-Stokes equations in light of the viscosity presented in practical hypersonic flow fields. The comparisons show that the second and third order piston theory compared very well with the aerodynamic load from the unsteady Euler equations, however, the Navier-Stokes solutions predict a much lower (up to 60% lower) surface pressure than the Euler equations and piston theory. However, the LCO amplitudes obtained by Nydick et al compared well with the results by Gray and Mei [9] for the case of hypersonic flutter of orthotropic panels. The most recent work by this group, Thuruthimattam et al. [60], further extended hypersonic flutter analysis to a double wedge airfoil and a 3-D generic hypersonic vehicle. The flutter analysis is conducted on basis of an integrated procedure that couples the computational fluid dynamics (CFD) solution with structural finite element analysis. Euler and Navier-Stokes aerodynamics were primarily used for the aerodynamic loading. However, the aeroelastic responses were validated by comparison with results from an independently developed aeroelastic code based on third order piston theory. The paper concluded that in a large portion of the flight envelope, good agreement is found between the double wedge airfoil flutter responses from calculations based on piston theory and those from Euler solutions.

Only in certain portions of the flight envelope, significant differences are observed between Euler based results and Navier-Stokes based solution. As to the 3-D generic hypersonic vehicle model, the difference between viscous (Navier-Stokes) and inviscid (Euler, piston) solutions on the vehicle is substantially smaller than on the double wedge foil.

Another group of studies on nonlinear panel flutter considering aerodynamic nonlinearity were given by Chandiramani et al. [61] and Chandiramani and Librescu [62]. Panel flutter in high supersonic flow of shear-deformable composite panels was investigated. High-order shear deformation theory and aerodynamic loads based on third order piston theory were used, and the panel flutter equations were derived using Galerkin's method. The arc length continuation method was used to determine the static equilibrium state and its dynamic stability was subsequently examined. Effects of small geometrical panel imperfection, airflow direction, uniform in-plane compression on flutter boundary were investigated. It was concluded that for moderately thick composite panel, shear deformation theory and nonlinear aerodynamic theory are required for determination of the flutter boundary. The post-flutter motion of such composite panels was also investigated by applying a predictor and Newton-Raphson type corrector technique for periodic solution and numerical integration for quasi-periodic or chaotic flutter solutions. Results showed that edge constraints normal to the flow appear to stabilize the panel, whereas those parallel to the flow do not noticeably affect the flutter speed and the immediate post-critical response. Chaotic motions were obtained for imperfect panels via the period-doubling scenario and for perfect panels where a sudden transition from the buckled state to one of chaos (followed by complicated periodic

motion) occurred. The near critical points bifurcation behavior of a simply supported isotropic panel was recently studied by Sri Namachchivaya and Lee [63]. Third-order piston theory and Galerkin's method were employed. It is found that inclusion of nonlinear aerodynamic terms could completely change the bifurcation behavior of the panel.

The applicability of various hypersonic aerodynamic theories is still a subject of active research. A few examples of such work are listed here for review purposes. One effort made by Chen and Liu [64], Chavez and Liu [65], and Liu et al. [66] was to develop a unified method for computation of the flow field of hypersonic/supersonic airflow that could be applied to aeroelastic problems. Two methods, the perturbed Euler characteristics (PEC) method and the unified hypersonic-supersonic lifting surface method, were developed. The PEC method is virtually an Euler approximation to the hypersonic flow. The method is developed to account for the effect of unsteady Mach wave/shock wave interaction and, hence, the rotationality and thickness effects. The lifting surface method is intended to generalize the exact three-dimensional linear theory for treatments of lifting surfaces in unsteady supersonic flow (Chen and Liu [64]) and to include the effects of nonlinear thickness and upstream influence in a unified supersonic-hypersonic flow regime. Both methods are proposed for panel flutter applications to extend the applicable range of piston theory. However, neither of the two methods could ultimately supersede the piston theory. As indicated by Liu et al. [66], because of the limitation in available measured data, further validation and applicability assessment of the proposed method are warranted. Another concern from the fluid mechanics point of view is the influence of boundary layers on panel flutter. Analysis and experimental

that determination of critical dynamic pressure with numerical accuracy of less than one unit could be considerably costly in computation time.

In a summary, the Euler aerodynamics (or its variations) and piston theory are applicable for unsteady, inviscid flow and Navier-Stokes equations for viscous fluids. Good agreement exists between panel flutter analyses using Euler equations and by piston theory. For panel flutter at hypersonic flow, viscosity effects can be neglected and nonlinear aerodynamic theory must be employed. This gives the reason for applying the third order piston theory in the present study of panel flutter of composite panels in hypersonic flow.

There are several system parameters that affect the panel flutter characteristics as reviewed by Mei et al. [8]. Among these influential parameters, the thermal effect is highlighted in the present work since the temperature of surface panels of any vehicle operating at hypersonic flow is raised by aerodynamic heating. Few investigations of panel flutter have dealt directly with thermal effects. Houboult [20] was the first to study the thermal buckling stability and flutter boundary for two-dimensional (2-D) plates subjected to uniform temperature distribution. Yang and Han [74] studied the linear flutter of thermally buckled 2-D panels using FEM. More recent research has extended to nonlinear flutter of panels under various temperature distributions. Xue and Mei [50,75] investigated the flutter boundaries of thermally buckled plates under non-uniform temperature distributions using FEM and von Karman large deflection plate theory for structural nonlinearity. Liaw [76] included geometrical nonlinearities in a finite element formulation and studied supersonic flutter of laminated composite plates. High temperature brings another structural instability phenomenon into concern — thermal

buckling. Therefore, for a typical surface panel of a hypersonic vehicle, two types of instability mechanisms, panel flutter and thermal buckling, may cause structural failure and damage. The coexistence of these two nonlinear phenomena could give rise to a complicated panel motion, chaos, which has been observed and investigated by researchers in many cases. The chaotic motion is also a focus of the present study and a brief review of pertinent research work is given in the next section.

1.2.2 Chaos Study

The first observation of chaotic motion was due to Lorenz [77] while developing a three-dimensional atmospheric dynamics model. The chaotic motion is typically irregular, unpredictable, never repeating and sensitive to initial conditions. Chaos is also termed as strange attractor in the sense that in phase space, chaos takes on the appearance of a fractal set, whereas the classical attractors, such as equilibrium, periodic motion, and LCO, have a shape of a point or closed curve. Chaotic motion is random-like but it is not random motion since the motion is controlled by deterministic governing equations of motion and it remains in a bounded region in phase space. The fundamental theories and physical understanding of chaos can be found in a series of published books [78-82].

Observation and investigation of chaos have been documented in a substantial body of literature and in a broad region of disciplines. It was found that chaotic vibration occurs when some strong nonlinearity exists in the system. A brief review of a few such studies in the nonlinear dynamics domain is given below.

One dynamic system that has been under concentrated study as a demonstration of chaos is a cantilevered beam buckled by magnetic forces undergoing nonlinear forced

vibration. Such a dynamic system possesses multiple equilibrium positions. This fact plus the high nonlinearity give rise to non-periodic and chaotic motion. The first experimental investigation of chaotic motion of a magnetically buckled beam system was given by Moon and Holmes [83]. Both experimental and theoretical evidence of the existence of a strange attractor in such a deterministic system is presented. The governing Partial Differential Equations (PDE) of motion were reduced to one Duffing-type Ordinary Differential Equation (ODE) by applying Galerkin's method. Fine agreement between the chaotic solutions from the ODE and the experiment observations was achieved. Moon [84] then extended the study on magnetically buckled beams to establish both experimental and theoretical threshold criteria for chaotic motions. Experimental Poincaré plots were used to assist in detecting the strange attractor. A heuristic semi-analytical criterion based in part on a perturbation solution for forced vibration and experimental observation was proposed. It is observed that at a fixed excitation frequency, changing excitation amplitude could result in periods one, two, three, four, or more times the driving period motion as well as chaotic motion. But, such motions might not persist since the chaotic motion might decay to the periodic motion. A review of theoretical and experimental studies of strange attractors and chaos in the field of nonlinear mechanics up to 1983 was given by Holmes and Moon [85]. Chaos or strange attractors observed in mechanical systems, electrical circuits, dynamos, feedback control systems, and chemical systems were reviewed and proposed analytical methods and criteria for chaos were summarized. It is pointed out that the demand of criteria for determining when a system may become chaotic and analytical methods to predict the spectral properties of the motion called for future work. Brunsden et al. [86] then

developed a theory that provides first order predictions of power spectra of single degree of freedom non-linear oscillators undergoing chaotic motions near homoclinic orbits based upon the assumption that the displacement of the oscillator can be represented by the random superposition, in time, of deterministic structures. The prediction approach was validated by comparing the predicted power spectra with numerical simulation of Duffing's equation and experimental spectra observed from a cantilever beam buckled by magnetic forces. It is well accepted that Duffing's equation has provided a useful paradigm for studies in non-linear oscillations hence attracted extensive analytical and numerical investigations. In view of this, Gottwald et al. [87] built an experimental set-up, with a ball rolling on a double-well potential energy surface, to mimic the behavior of Duffing's equation. With this elaborately designed experiment apparatus, nonlinear dynamics features, such as competing steady state attractors, hysteresis, sensitivity to initial conditions, subharmonic oscillations, and chaos, can be illustrated.

Nonlinear aeroelasticity is a rich source of static and dynamic instability and associated LCO or even chaotic motions [88]. Panel flutter, induced by the highly nonlinear fluid-structure interaction, has long been recognized as a source of chaotic motion [79, 80]. Study of chaotic motions associated with flutter of a buckled simply supported plate was conducted by Dowell [89]. Two control parameters, dynamic pressure (flow velocity) and in-plane compressive load, were changed systematically to observe chaotic motion in the phase plane. For the isotropic simply supported plate under study, it was found that chaos occured at moderate to large dynamic pressure and sufficiently large in-plane compressive force. A later paper by Dowell [90] illustrated four important chaos indicators, time histories, phase plane portraits, power spectra

densities, and Poincaré maps, with emphasis on the latter two. The method of construction of the Poincaré map was adopted in the present study with slight modifications. A survey on how numerical methods can be used to solve nonlinear aeroelasticity problems and various types of complicated behavior typically encountered in nonlinear aeroelastic systems was due to Virgin and Dowell [91]. In the field of panel flutter analysis using nonlinear aerodynamic theory, few efforts were made to study chaos. Two such papers reviewed earlier, Chandiramani et al. [61] and Nydick et al. [59], touched upon the topic of the possible occurrence of nonperiodic or chaotic motions for panel flutter in high supersonic or hypersonic flow.

One frequently used concept in chaos study is bifurcation. Literarily, bifurcation means splitting into two parts. The term bifurcation is commonly used in the study of nonlinear dynamics to describe any sudden change in the behavior of the system as some control parameter changes. Mathematically, bifurcation is defined as when a physical parameter in the system under study changes by a small amount, the solution curve branches out to family of curves. More extensive mathematical description of bifurcation theory can be found in many books, such as Mittelmann and Weber [92], Bruter et al. [93], and more recently Chen and Leung [94]. Applications of bifurcation theory to panel flutter analysis to yield qualitative bifurcation solutions to governing PDE or ODE were outlined by Holmes [95] and Holmes and Marsden [96]. The application of bifurcation theory to explain the results shown in the bifurcation diagram is one of the emphases of the current study. An excellent investigation of chaos in supersonic panel flutter by observation of bifurcation was performed by Bolotin et al. [97]. Two control parameters, the compressive in-plane force and the dynamic pressure, are varied independently and

continuously along both backward and forward paths to observe chaos and demonstrate the hysteretic behavior. A number of bifurcations were found and various pertinent patterns of transition among divergence, symmetric flutter, asymmetric flutter, and chaotic motion were observed, as well as several hysteretic phenomenon. One previously referenced paper, Sri Namachchivaya and Lee [63], analyzed the bifurcation behavior of fluttering panels using nonlinear aerodynamic theory.

The panel flutter problem under study is intrinsically deterministic in the sense that the time response of the panel is numerically simulated on the basis of a given set of governing equations of motion. The chaotic motion of such a system is also termed as deterministic chaos, which denotes the irregular or chaotic motion that is generated by nonlinear systems whose dynamical laws uniquely determine the time evolution of a state of the system from a knowledge of its previous history (Schuster [98]). Naturally, there must exist "deterministic" quantities to characterize a chaotic motion other than the qualitative tools like the phase plane plot and Poincaré map. It is expected that these quantities should be able to define critical boundaries of chaos in terms of control parameters and to tell what extent the chaos has reached. Two well accepted quantitative measures have been developed and applied widely in study of chaos: the Lyapunov exponent and the fractal dimension. Approaches for calculation of the Lyapunov exponent of dynamical systems were presented by a few pioneer researchers. Shimada and Nagashima [99] and Benettin et al. [100, 101] presented numerical methods for computing the Lyapunov exponent of systems whose equations of motion are explicitly known. As an extension of these methods, Wolf et al. [102] proposed an algorithm to estimate non-negative Lyapunov exponents from an experimental time series. Review of

the concept of Lyapunov exponents and discussion on their calculation from observed data were given by Abarbanel et al. [103]. Pezeshi and Dowell [104] used the computer program from Wolf et al. [102] to calculate the Lyapunov exponent spectrum of a magnetically buckled beam on basis of the one, two, three, and four-mode projections of the governing PDE, which was derived by Tang and Dowell [105] in study of the threshold force for chaotic motion in such a buckled beam system. Pezeshi and Dowell [104] also successfully compared the largest Lyapunov exponent calculated from the governing PDEs to that computed from the experimental time history using another algorithm from Wolf [102]. More recently, Fermen-Coker and Johnson [106] also adopted the algorithms from Wolf [102] to investigate the thermal effects on the onset of chaotic vibrations of simply supported isotropic plates by computing the largest Lyapunov exponent. A single mode Duffing's equation was derived as the governing equation of motion. Three types of thermal loading, uniform temperature increase at the panel midplane, a parabolic temperature variation over the panel, and a temperature gradient across the thickness of the panel are considered. Although the paper aimed to provide a design tool for external panels of hypersonic vehicles, the effects of aerodynamic forces were not included in the analysis. Chandiramani et al. [61] considered the aerodynamic force effects while computing Lyapunov exponents to study the nonperiodic/chaotic motion of composite panels under in-plane compression. However, their method possessed some limitations of analytical approach and in effect, some special cases of thermal loading on surface panels of hypersonic vehicles cannot be approximated by uniformly distributed in-plane compression. As mentioned at the beginning of this section, the fractal dimension is another qualitative measure of chaos.

The Lyapunov spectrum is closely related to the fractal dimension. The relationship between fractal dimension, information entropy and Lyapunov spectrum was made by Kalplan and Yorke [107]. The fractal dimension is not among the interests of the present study.

1.3 Objectives and Scope

The primary goal of the present study is to develop a finite element time domain modal formulation applied to panel flutter analysis of isotropic or composite thin panels in hypersonic airflow. Such a modal formulation is intended to be a practical design tool for hypersonic vehicle surface panel design. "Practical" herein is understood as cost (computation time) effective without losing much accuracy and simple enough for application without sophisticated mathematical manipulations. "Practical" also means that as much as possible real design considerations, such as application of composites and thermal loading must be incorporated into the algorithm. It is also anticipated that such formulation will assist in fatigue analysis and flutter suppression controller design during the development of hypersonic vehicles.

The time domain formulation is a complement to existing frequency domain panel flutter approaches, which, as reviewed before, are incapable of investigating panel motion types other than harmonic or periodic LCO. However, solving the governing equations of motion in physical coordinates by direct numerical integration [52, 53] could be extremely costly, especially when fine meshes are required due to the high nonlinearity inherent to the analyzed fluttering panel structure. To avoid the waste of computer resources and the necessity of producing huge amounts of time history data, a modal

truncation technique, which has already been applied successfully to supersonic panel flutter analysis, is introduced to simplify the work. Subsequently, issues such as selection of modes to be used, validation of computational accuracy, etc., have to be addressed.

Verification of the proposed time domain modal formulation will be conducted through comparing the flutter results with limited available results in the literature. Then, the method can be applied to flutter analysis of othotropic/composite panels under combined hypersonic aerodynamic pressure and thermal loading due to aerodynamic heating. It is the thermal loading that makes all types of complicated panel motions more likely to occur with low amplitude of control parameters. Of these motions, chaos is the most highlighted. The scenario for commencement of chaotic motion, rather than the severity of chaos, is the major concern. This means that the "boundary" between LCO and chaos is of interest since design of surface panels could be guided so that chaotic motion is avoided. All diagnosis and inspection tools for complicated motions are taken for direct use. Studies of the algorithms behind these tools are beyond the scope of present study.

In Chapter 2, a detailed finite element formulation is given. The governing equation of motion in physical coordinates is derived based on the principle of virtual work. As explained before, von Karman large deflection plate theory is employed to address structural nonliearity and full third order piston theory is used to consider the aerodynamic nonlinearity. The C^1 conforming Bogner-Fox-Schmit (BFS) finite element is utilized to discretize the panel. Modal transformation is performed on the assembled system governing equations of motion in physical coordinates. Evaluation procedures of

all nonlinear stiffness matrices, and nonlinear aerodynamic damping matrices are presented.

In Chapter 3, the governing equations of motion in modal coordinates are further transformed into a state space representation to ease the implementation of direct numerical integration. The fourth order Runge-Kutta integration scheme is then applied to generate the time histories and other useful data sets. Applications of time histories, phase plane plots, Poincaré maps, bifurcation diagrams, and Lyapunov exponents in detection and analysis of various panel motions are also overviewed.

An effective procedure for filtering out influential modes to be used in the time integration is explained in detail. The procedure is on basis of the concept of a modal participation factor. Some programming know-how on how to achieve the goal of reducing computation cost is also highlighted. The entire solution procedure is summarized by a detailed flow chart for better understanding.

Chapter 4 presents the numerical results and corresponding discussion. LCO amplitudes of an isotropic/orthotropic panel are compared to existing results from analytical methods and finite element frequency domain methods for verification purpose. Evolution of chaos for isotropic/orthotropic panels is observed with the assistance of phase plane plots and Poincaré maps. Global bifurcation behavior of an isotropic/orthotropic panel is examined by construction of bifurcation diagrams.

There are two ways to establish the "boundary" between LCO and chaos when the two system control parameters changed continuously. One is using bifurcation diagrams in conjunction with phase plane plots and/or Poincaré maps. Another way is computing the largest Lyapunov exponent. The former approach is applied to the isotropic

/orthotropic panels and the Lyapunov exponent approach is first illustrated with isotropic panels and then applied to the composite panel cases. Effects of aerodynamic damping coefficients and temperature gradient on such boundaries are examined in detail. A few conclusions according to all analyses are presented in Chapter 5.

CHAPTER II

FINITE ELEMENT FORMULATION

In this chapter, the governing equation of motion (EOM) for a three dimensional panel under both aerodynamic and thermal loading will be developed. The EOM is firstly expressed in terms of structural degrees of freedom (DOF), or in physical coordinates. Then the system level EOM is transformed into modal coordinates based upon the expansion theorem [108].

The plate is subjected in a combined aerodynamic and thermal environment. High temperature and hypersonic airflow result in highly nonlinear vibration of the plate. The von Karman large deflection plate theory [23, 109] is herein employed to describe the nonlinear strain and displacement relationships. The third order piston theory [24] is used for aerodynamic pressure distribution. Current work falls into the category 5 analysis defined by Mei et al. [8], that is, flutter analysis using nonlinear structural theory and nonlinear aerodynamic theory.

2.1 Problem Description

Depicted in Fig 2.1 is a sketch of the 3-D panel. The panel could be isotropic, othotropic or laminated. The panel has geometrical dimensions of length a, width b, and thickness h. In present work, only thin panels ($a/h > 50$) is under consideration in light of aerospace applications. Therefore, the effects of transverse shear are neglected.

The airflow is assumed to be parallel to panel length and takes the direction of positive x coordinate. The positive transverse deflection of the panel is toward the cavity

on one side of the panel. The family of piston theory [24] gives the relationship between the local point function pressure generated by the panel's motion and the local normal component of the flow velocity. Basic assumptions include: (1) the local motion of the panel can be simulated by a moving piston, (2) the air is ideal and it has a constant specific heat, the piston generates only simple waves and produces no entropy changes, (3) the local panel motion velocity is much smaller than the air flow velocity, and (4) the air flow is parallel to the panel surface. The first order piston theory gives a linear relationship that is generally applicable to supersonic speed. The second and third order piston theories depict the nonlinear (quadratic, cubic) relationships between local pressure fluctuation and local motion of the panel. Since present flutter analysis mainly concerns panel motion under high supersonic or hypersonic airflow, the nonlinear piston theory is applied. Of the two nonlinear piston theories, the third order piston theory is in a complete form that incorporates contributions from the second and third order terms. The aerodynamic pressure given by the third order piston theory is [9]

$$\Delta p = p_a - p_\infty = \frac{2q}{M} \left[\frac{1}{V} w_{,t} + w_{,x} + \frac{(\gamma+1)}{4} M \left(\frac{1}{V} w_{,t} + w_{,x} \right)^2 \right.$$

$$\left. + \frac{(\gamma+1)}{12} M^2 \left(\frac{1}{V} w_{,t} + w_{,x} \right)^3 \right] \tag{2.1}$$

To investigate the contributions from first, second and third order terms in Eq. (2.1), switch flags or variables are introduced to enable/disable related terms, as expressed in following equation

$$\Delta p = p_a - p_\infty = \frac{2q}{M} \left[\frac{1}{V} C_{1t} w_{,t} + C_{1x} w_{,x} + \frac{(\gamma+1)}{4} M \left(\frac{1}{V} C_{2t} w_{,t} + C_{2x} w_{,x} \right)^2 \right.$$

$$+ \frac{(\gamma+1)}{12} M^2 \left(\frac{1}{V} C_{3t} w_{,t} + C_{3x} w_{,x} \right)^3 \Bigg] \tag{2.2}$$

Clearly, by setting C_{1i}, C_{1x}, C_{2t}, C_{2x}, C_{3t} and C_{3x} to 1/0 could switch on/off contributions from corresponding terms in Eq. (2.2). The symbols involved are defined as:

p_a	Aerodynamic pressure
p_∞	Undisturbed pressure of the perfect gas
$q = \rho_a V^2/2$	Dynamic pressure
M	Mach number
γ	Specific-heat ratio of air ($\cong 1.4$)
V	flow velocity
w	transverse panel deflection.

For thin-walled structures that have extensive applications in aircraft, the close to reality steady-state temperature field is a function of all three coordinates, i.e., $\Delta T(x, y, z)$. As suggested by some earlier researchers [110, 111], the temperature variation can be assumed to be linearly distributed across the plate thickness as $\Delta T = T_0 + zT_1/h$ (Fig. 2.1b), where T_0 is the average temperature of the plate and T_1 is the temperature gradient through the plate thickness. By setting $T_1 = 0.0$, a special case of uniform temperature distribution is reached. Temperature induced in-plane thermal stresses and transverse bending moments may weaken or stiffen the panel. Interactions between thermal and aerodynamic effects result in complicated motions of the panel: limit cycle oscillation, periodic motion, non-periodic motion, and chaos. The main goal of present work is to develop a cost effective methodology for high supersonic/hypersonic flutter analysis and apply it to investigation of the post-transient motions of thin panels.

(a) Aerodynamic loading

(b) Temperature distribution
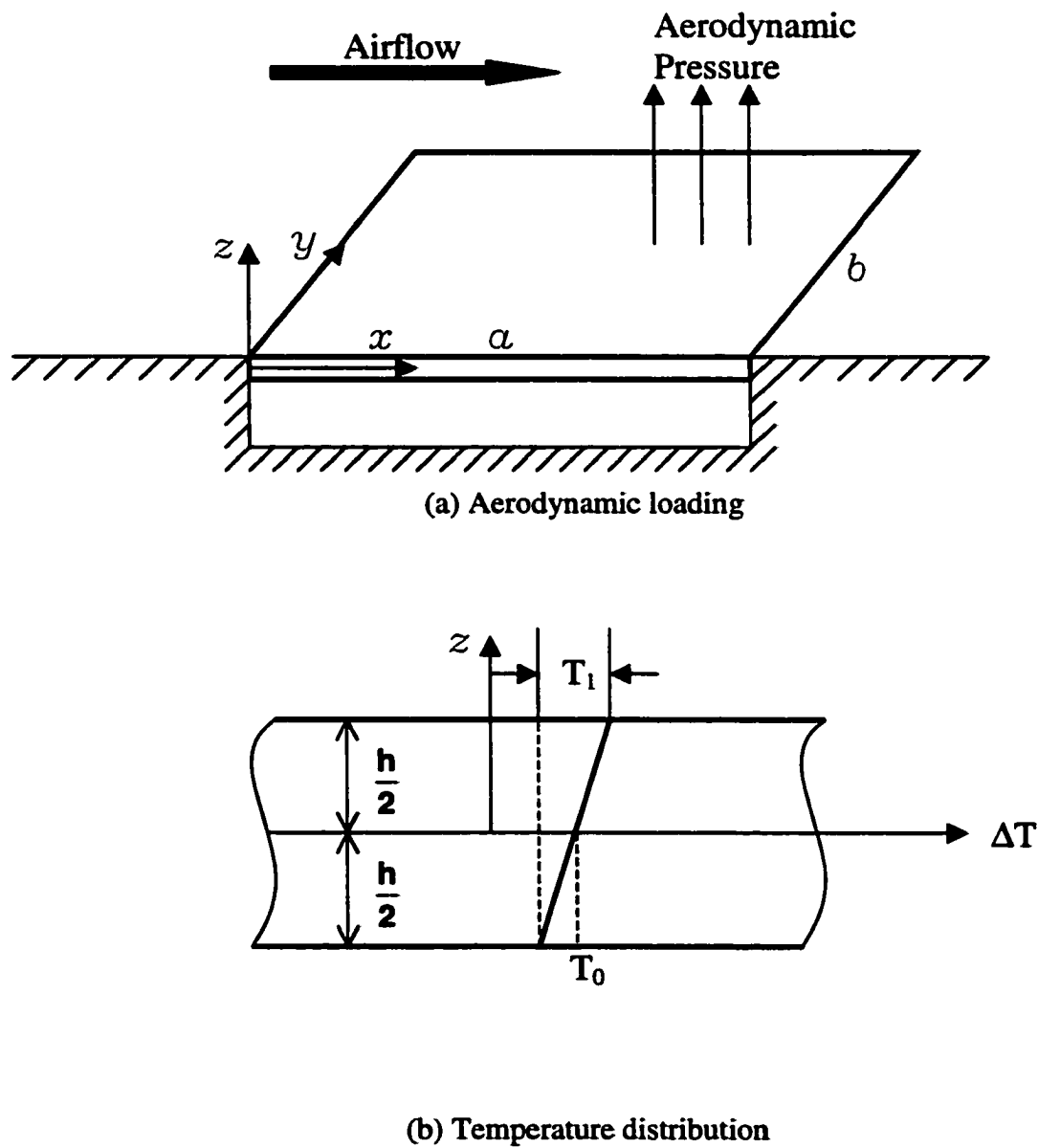
Fig. 2.1 Thermal and aerodynamic environment

for a three-dimensional panel

2.2 Governing EOM in Structure DOF

As stated before, flutter of isotropic, orthortropic, and laminated panels will be studied. Since the isotropic, orthotropic and symmetrical laminates can be treated as special cases of general laminates, only the EOM for general laminates are formulated in detail.

2.2.1 Finite element

The 24-DOF Bogner-Fox-Schmit C^l conforming rectangular plate element is used for the finite element model. Figure 2.2 shows one finite element for laminated panel. The displacement vector at each node includes the in-plane displacement vector $\{u \quad v\}$ and transverse bending displacement vector $\left\{w \quad \dfrac{\partial w}{\partial x} \quad \dfrac{\partial w}{\partial y} \quad \dfrac{\partial w}{\partial x \partial y}\right\}$. Therefore, the nodal displacement vector of the entire element is

$$\{w\} = \begin{Bmatrix} w_b \\ w_m \end{Bmatrix} \tag{2.3}$$

in which $\{w_b\}$ and $\{w_m\}$ are collections of bending displacements and in-plane displacements at the four nodes. The panel is discretized by modeling it as a series of finite elements. The field quantities (i.e., the in-plane/bending displacements) within the element domain are then interpolated from corresponding nodal vectors. A detailed formulation for the interpolation functions and element matrices of the rectangular plate element is given in Appendix A. In a brief form, the displacements at an arbitrary point in the element can be expressed as follows
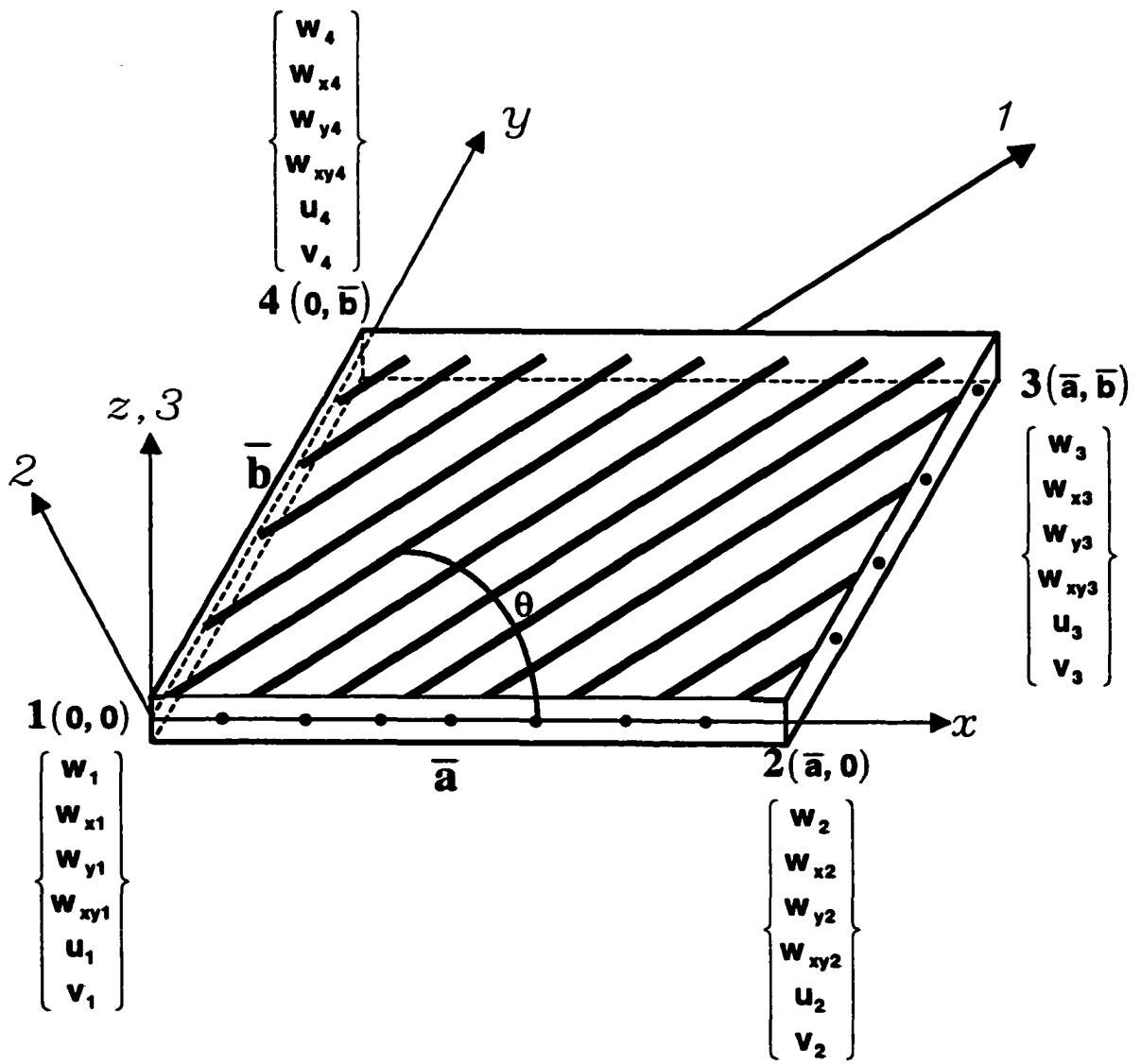
Fig. 2.2 Bogner-Fox-Schmit C^1 conforming rectangular plate element for a laminate

$$w = [H_w][T_b]\{w_b\} \tag{2.4}$$

$$u = [H_u][T_m]\{w_m\} \tag{2.5}$$

$$v = [H_v][T_m]\{w_m\} \tag{2.6}$$

2.2.2 Strain-Displacement Relationships and Constitutive Equations

While undergoing large amplitude deflection, which means the transverse displacement of the panel is of the same order of magnitude as the panel thickness, the in-plane membrane response becomes coupled to the transverse bending. As the plate bends, the middle surface stretches and significant membrane forces develop. The load-transverse deflection response becomes nonlinear. The von Karman plate theory addresses above in-plane extension effects by introducing additional quadratic terms to the strains developed in a vibrating plate. The nonlinear strain-displacement relationship is given as

$$\{\varepsilon\} = \left\{ \begin{array}{c} u_{,x} \\ v_{,y} \\ u_{,y} + v_{,x} \end{array} \right\} + \frac{1}{2} \left\{ \begin{array}{c} w_{,x}^2 \\ w_{,y}^2 \\ 2w_{,x}w_{,y} \end{array} \right\} + z \left\{ \begin{array}{c} -w_{,xx} \\ -w_{,yy} \\ -2w_{,xy} \end{array} \right\}$$

$$= \{\varepsilon_m^0\} + \{\varepsilon_\theta^0\} + z\{\kappa\} \tag{2.7}$$

where $\{\varepsilon_m^0\}$ = the first term, linear membrane strain vector

$\{\varepsilon_\theta^0\}$ = the second term, von Karman nonlinear membrane strain vector

$z\{\kappa\}$ = the last term, bending strain vector

By substitution of Eqs. (2.4), (2.5) and (2.6) into Eq. (2.7), the strain components can be expressed in terms of finite element nodal displacement vectors.

Noted that matrices $[T_b]$ and $[T_m]$ are constant and interpolation functions $[H_w]$, $[H_u]$ and $[H_v]$ are functions of x, y coordinates, the linear membrane strain $\left\{\varepsilon_m^0\right\}$ can be expressed as

$$\left\{\varepsilon_m^0\right\}=\left\{\begin{array}{c} u_{,x} \\ v_{,y} \\ u_{,y}+v_{,x} \end{array}\right\}=\left\{\begin{array}{c} \dfrac{\partial}{\partial x}[H_u] \\ \dfrac{\partial}{\partial y}[H_v] \\ \dfrac{\partial}{\partial y}[H_u]+\dfrac{\partial}{\partial x}[H_v] \end{array}\right\}[T_m]\{w_m\}=[C_m]\{w_m\} \qquad (2.8)$$

The von Karman nonlinear membrane strain $\left\{\varepsilon_\theta^0\right\}$ can be expressed as

$$\left\{\varepsilon_\theta^0\right\}=\frac{1}{2}\begin{bmatrix} w_{,x} & 0 \\ 0 & w_{,y} \\ w_{,y} & w_{,x} \end{bmatrix}\left\{\begin{array}{c} w_{,x} \\ w_{,y} \end{array}\right\}=\frac{1}{2}[\theta]\{G\}$$

$$=\frac{1}{2}[\theta]\left\{\begin{array}{c} \dfrac{\partial}{\partial x}[H_w] \\ \dfrac{\partial}{\partial y}[H_w] \end{array}\right\}[T_b]\{w_b\}=\frac{1}{2}[\theta][C_\theta]\{w_b\} \qquad (2.9)$$

The matrix $[\theta]$ and vector $\{G\}$ are called slope matrix and slope vector, respectively.

Similarly, the bending curvature $\{\kappa\}$ can be expressed as

$$\{\kappa\}=-\left\{\begin{array}{c} w_{,xx} \\ w_{,yy} \\ 2w_{,xy} \end{array}\right\}=-\left\{\begin{array}{c} \dfrac{\partial^2}{\partial x^2}[H_w] \\ \dfrac{\partial^2}{\partial y^2}[H_w] \\ 2\dfrac{\partial^2}{\partial x \partial y}[H_w] \end{array}\right\}[T_b]\{w_b\}=[C_b]\{w_b\} \qquad (2.10)$$

2.2.3 Stress-Strain Relationships and Constitutive Equations

For an isotropic thin panel in plane stress, the stress-strain relationship is defined by Hooke's law as

$$\begin{Bmatrix} \sigma_x \\ \sigma_y \\ \tau_{xy} \end{Bmatrix} = \begin{bmatrix} E & 0 & 0 \\ 0 & \nu E & 0 \\ 0 & 0 & G \end{bmatrix} \begin{Bmatrix} \varepsilon_x \\ \varepsilon_y \\ \gamma_{xy} \end{Bmatrix} \qquad (2.11)$$

where E is the Young's modulus of the material and $G = E/2(1+\nu)$; ν is the Possion's ratio of the isotropic material.

For a general orthotropic lamina, because of the anisotropic material properties, the stress-strain relationships are derived with a coordinate transformation from the material coordinates (Fig. 2.2) to the x, y coordinates [112]

$$\{\sigma\} = \begin{Bmatrix} \sigma_x \\ \sigma_y \\ \sigma_{xy} \end{Bmatrix} = \begin{bmatrix} \overline{Q}_{11} & \overline{Q}_{12} & \overline{Q}_{16} \\ \overline{Q}_{12} & \overline{Q}_{22} & \overline{Q}_{26} \\ \overline{Q}_{16} & \overline{Q}_{26} & \overline{Q}_{66} \end{bmatrix} \begin{Bmatrix} \varepsilon_x \\ \varepsilon_y \\ \gamma_{xy} \end{Bmatrix} = [\overline{Q}]\{\varepsilon\} \qquad (2.12)$$

in which the entries for the transformed reduced lamina stiffness matrix $[\overline{Q}]$ are

$$\overline{Q}_{11} = Q_{11}\cos^4\theta + 2(Q_{12} + 2Q_{66})\sin^2\theta\cos^2\theta + Q_{22}\sin^4\theta$$

$$\overline{Q}_{12} = (Q_{11} + Q_{22} - 4Q_{66})\sin^2\theta\cos^2\theta + Q_{12}(\cos^4\theta + \sin^4\theta)$$

$$\overline{Q}_{22} = Q_{11}\sin^4\theta + 2(Q_{12} + 2Q_{66})\sin^2\theta\cos^2\theta + Q_{22}\cos^4\theta$$

$$\overline{Q}_{16} = (Q_{11} - Q_{12} - 2Q_{66})\cos^3\theta\sin\theta - (Q_{22} - Q_{12} - 2Q_{66})\cos\theta\sin^3\theta \qquad (2.13)$$

$$\overline{Q}_{26} = (Q_{11} - Q_{12} - 2Q_{66})\sin^3\theta\cos\theta - (Q_{22} - Q_{12} - 2Q_{66})\cos^3\theta\sin\theta$$

$$\overline{Q}_{66} = (Q_{11} + Q_{22} - 2Q_{12} - 2Q_{66})\cos^2\theta\sin^2\theta + Q_{66}(\sin^4\theta + \cos^4\theta)$$

The Q_{ij}'s are the reduced stiffness in the material coordinate systems. For the orthotropic lamina, Q_{ij}'s are evaluated as

$$Q_{11} = \frac{E_{11}}{(1-v_{12}v_{21})}, \qquad Q_{12} = \frac{v_{12}E_{22}}{(1-v_{12}v_{21})}$$

$$Q_{22} = \frac{E_{22}}{(1-v_{12}v_{21})}, \qquad Q_{66} = G_{12}$$

(2.14)

The subscripts i, j = 1, 2, 6 denote the material principal coordinates shown in Fig. 2.2. By setting $E_{11} = E_{22} = E$, $G_{12} = G$, and $v_{12} = v_{21} = v$, the isotropic case is reached.

In consideration of thermal effects, the stress resultants can be evaluated as [113, 114]

$$\begin{Bmatrix} N \\ M \end{Bmatrix} = \begin{bmatrix} A & B \\ B & D \end{bmatrix} \begin{Bmatrix} \varepsilon^0 \\ \kappa \end{Bmatrix} - \begin{Bmatrix} N_{\Delta T} \\ M_{\Delta T} \end{Bmatrix}$$

(2.15)

where,   extensional matrix $A_{ij} = \sum_{k=1}^{n} (\overline{Q}_{ij})_k (z_{k+1} - z_k)$ (2.16a)

extensional-bending $B_{ij} = \frac{1}{2} \sum_{k=1}^{n} (\overline{Q}_{ij})_k (z_{k+1}^2 - z_k^2)$ (2.16b)

flexural matrix $D_{ij} = \frac{1}{3} \sum_{k=1}^{n} (\overline{Q}_{ij})_k (z_{k+1}^3 - z_k^3)$ (2.16c)

in-plane thermal loads $\{N_{\Delta T}\} = \int_{-h/2}^{h/2} [\overline{Q}]_k \{\alpha\}_k \Delta T(x,y,z) dz$ (2.16d)

thermal bending moment $\{M_{\Delta T}\} = \int_{-h/2}^{h/2} [\overline{Q}]_k \{\alpha\}_k \Delta T(x,y,z) z dz$ (2.16e)

i, j   = 1, 2, 6

k   the k-th layer

n   total number of layers

h   thickness of the plate

$\{\alpha\}_k$ thermal expansion vector of the k-th layer

ΔT temperature change

For isotropic and symmetrically laminated panels, the extensional-bending coupling matrix vanishes. The extensional matrix [A] and flexural matrix [D] for isotropic panel are simply

$$[A] = \frac{E}{1-v^2}\begin{bmatrix} 1 & v & 0 \\ v & 1 & 0 \\ 0 & 0 & \frac{1-v}{2} \end{bmatrix}, \qquad [D] = \frac{Eh^3}{12(1-v^2)}\begin{bmatrix} 1 & v & 0 \\ v & 1 & 0 \\ 0 & 0 & \frac{1-v}{2} \end{bmatrix} \qquad (2.17)$$

According to the strain-displacement relationships given in section 2.2.2, the stress resultants can be expressed in terms of finite element nodal displacement vectors as

$$\{N\} = [A]\{\varepsilon_m^0 + \varepsilon_\theta^0\} + [B]\{\kappa\} - \{N_{\Delta T}\}$$

$$= [A][C_m]\{w_m\} + \frac{1}{2}[A][\theta][C_\theta]\{w_b\} + [B][C_b]\{w_b\} - \{N_{\Delta T}\} \qquad (2.18)$$

$$= \{N_m\} + \{N_\theta\} + \{N_b\} - \{N_{\Delta T}\}$$

$$\{M\} = [B]\{\varepsilon_m^0 + \varepsilon_\theta^0\} + [D]\{\kappa\} - \{M_{\Delta T}\}$$

$$= [B][C_m]\{w_m\} + \frac{1}{2}[B][\theta][C_\theta]\{w_b\} + [D][C_b]\{w_b\} - \{M_{\Delta T}\} \qquad (2.19)$$

$$= \{M_m\} + \{M_\theta\} + \{M_b\} - \{M_{\Delta T}\}$$

Here $\{N_m\}, \{M_m\}, \{N_\theta\}, \{M_\theta\}$, $\{N_b\}$, and $\{M_b\}$ are stress resultants induced by inpalne or membrane (subscript m) stresses, stresses due to large deflection effects (subscript θ) and bending stresses (subscript b). $\{N_{\Delta T}\}$ and $\{M_{\Delta T}\}$ are thermal stress resultants as evaluated with Eq. (2.16).

2.2.4 Governing EOM

The governing EOM is derived using the principle of virtual work (or virtual displacements) with incorporation of D'Alambert's principle. The principle of virtual

work states that for a body in equilibrium, the total virtual work done due to virtual displacement is zero. The virtual work is classified as internal virtual work δW_{int}, which is attributed to internal forces (herein stress resultants), and the external virtual work δW_{ext}, which is done by applied external forces (herein the aerodynamic pressure) and body forces (herein the inertia forces). Therefore, the principle of virtual work enforces that

$$\delta W = \delta(W_{int} - W_{ext}) = 0 \tag{2.20}$$

Virtual Work Done by Internal Stresses

The virtual work done by internal stresses is

$$\delta W_{int} = \int_V \sigma_{ij} \delta\varepsilon_{ij} dV = \int_A \left(\{\delta\varepsilon^0\}^T \{N\} + \{\delta\kappa\}^T \{M\} \right) dA \tag{2.21}$$

The variations of in-plane membrane strain $\{\delta\varepsilon^0\}$ and curvature $\{\delta\kappa\}$ can be expanded in view of Eqs. (2.7) ~ (2.10) as

$$\{\delta\varepsilon^0\}^T = \{\delta\varepsilon_m^0\}^T + \{\delta\varepsilon_\theta^0\}^T = \{\delta w_m\}^T [C_m]^T + \{\delta w_b\}^T [C_\theta]^T [\theta]^T \tag{2.22}$$

$$\{\delta\kappa\}^T = \{\delta w_b\}^T [C_b]^T \tag{2.23}$$

Note that it is easy to prove $\delta\left(\dfrac{1}{2}[\theta]\{G\}\right) = [\theta]\{\delta G\}$.

Substituting the stress resultants given in Eqs. (2.18) and (2.19), as well as strain, curvature variations given in Eqs. (2.22), (2.23) into Eq. (2.21), the internal virtual work can be expressed in terms of nodal displacement vectors as

$$\delta W_{int} = \int_A \left[\left(\{\delta w_m\}^T [C_m]^T + \{\delta w_b\}^T [C_\theta]^T [\theta]^T \right) \left([A][C_m]\{w_m\} + \frac{1}{2}[A][\theta][C_\theta]\{w_b\} \right. \right.$$
$$+ [B][C_b]\{w_b\} - \{N_{\Delta T}\} \right) + \left(\{\delta w_b\}^T [C_b]^T \right) \left([B][C_m]\{w_m\} \right.$$

$$+\frac{1}{2}[B][\theta][C_\theta]\{w_b\}+[D][C_b]\{w_b\}-\{M_{\Delta T}\}\Bigg)\Bigg]dA \qquad (2.24)$$

Further expansion of Eq. (2.24) produces 12 terms as listed following

| 1st | $\{\delta w_m\}^T[C_m]^T[A][C_m]\{w_m\}$ | (2.25a) |

$$1^{st} \qquad \{\delta w_m\}^T[C_m]^T[A][C_m]\{w_m\} \qquad (2.25a)$$

$$2^{nd} \qquad \frac{1}{2}\{\delta w_m\}^T[C_m]^T[A][\theta][C_\theta]\{w_b\} \qquad (2.25b)$$

$$3^{rd} \qquad \{\delta w_m\}^T[C_m]^T[B][C_b]\{w_b\} \qquad (2.25c)$$

$$4^{th} \qquad -\{\delta w_m\}^T[C_m]^T\{N_{\Delta T}\} \qquad (2.25d)$$

$$5^{th} \qquad \{\delta w_b\}^T[C_\theta]^T[\theta]^T[A][C_m]\{w_m\} \qquad (2.25e)$$

$$6^{th} \qquad \frac{1}{2}\{\delta w_b\}^T[C_\theta]^T[\theta]^T[A][\theta][C_\theta]\{w_b\} \qquad (2.25f)$$

$$7^{th} \qquad \{\delta w_b\}^T[C_\theta]^T[\theta]^T[B][C_b]\{w_b\} \qquad (2.25g)$$

$$8^{th} \qquad -\{\delta w_b\}^T[C_\theta]^T[\theta]^T\{N_{\Delta T}\} \qquad (2.25h)$$

$$9^{th} \qquad \{\delta w_b\}^T[C_b]^T[B][C_m]\{w_m\} \qquad (2.25i)$$

$$10^{th} \qquad \frac{1}{2}\{\delta w_b\}^T[C_b]^T[B][\theta][C_\theta]\{w_b\} \qquad (2.25j)$$

$$11^{th} \qquad \{\delta w_b\}^T[C_b]^T[D][C_b]\{w_b\} \qquad (2.25k)$$

$$12^{th} \qquad -\{\delta w_b\}^T[C_b]^T\{M_{\Delta T}\} \qquad (2.25l)$$

Terms 1, 3, 9, and 11 can be written in the matrix form as

$$\begin{Bmatrix}\delta w_b\\ \delta w_m\end{Bmatrix}^T\begin{bmatrix}k_b & k_{bm}\\ k_{mb} & k_m\end{bmatrix}\begin{Bmatrix}w_b\\ w_m\end{Bmatrix} \qquad (2.26)$$

which gives the definition of linear stiffness matrices as

$$[k_b]=\int_A[C_b]^T[D][C_b]dA \qquad (2.27)$$

$$[k_m] = \int_A [C_m]^T [A][C_m] dA \tag{2.28}$$

$$[k_{mb}] = [k_{bm}]^T = \int_A [C_m]^T [B][C_b] dA \tag{2.29}$$

Terms 2 and 5 can be written as

Term 2 + Term 5

$$= \frac{1}{2}\{\delta w_m\}^T [C_m]^T [A][\theta][C_\theta]\{w_b\} + \{\delta w_b\}^T [C_\theta]^T [\theta]^T [A][C_m]\{w_m\}$$

$$= \frac{1}{2}\{\delta w_m\}^T [C_m]^T [A][\theta][C_\theta]\{w_b\} + \frac{1}{2}\{\delta w_b\}^T [C_\theta]^T [\theta]^T [A][C_m]\{w_m\}$$

$$+ \frac{1}{2}\{\delta w_b\}^T [C_\theta]^T [\theta]^T [A][C_m]\{w_m\}$$

$$= \frac{1}{2}\{\delta w_m\}^T [C_m]^T [A][\theta][C_\theta]\{w_b\} + \frac{1}{2}\{\delta w_b\}^T [C_\theta]^T [\theta]^T [A][C_m]\{w_m\}$$

$$+ \frac{1}{2}\{\delta w_b\}^T [C_\theta]^T [N_m][C_\theta]\{w_b\}$$

$$= \frac{1}{2}\{\delta w_m\}[n1_{mb}]\{w_b\} + \frac{1}{2}\{\delta w_b\}[n1_{bm}]\{w_m\} + \frac{1}{2}\{\delta w_b\}[n1_{nm}]\{w_b\}$$

$$= \frac{1}{2}\begin{Bmatrix} \delta w_b \\ \delta w_m \end{Bmatrix}^T \begin{bmatrix} n1_{nm} & n1_{bm} \\ n1_{mb} & 0 \end{bmatrix} \begin{Bmatrix} w_b \\ w_m \end{Bmatrix} \tag{2.30}$$

Note that following transformation based on Eqs. (2.9) and (2.18) is utilized to achieve the symmetry $([n1_{mb}] = [n1_{bm}]^T)$ of the nonlinear stiffness matrix

$$[\theta]^T [A][C_m]\{w_m\} = [\theta]^T \{N_m\} = \begin{bmatrix} \dfrac{\partial w}{\partial x} & 0 & \dfrac{\partial w}{\partial y} \\ 0 & \dfrac{\partial w}{\partial y} & \dfrac{\partial w}{\partial x} \end{bmatrix} \begin{Bmatrix} N_{xm} \\ N_{ym} \\ N_{xym} \end{Bmatrix} = \begin{Bmatrix} \dfrac{\partial w}{\partial x}N_{xm} + \dfrac{\partial w}{\partial y}N_{xym} \\ \dfrac{\partial w}{\partial y}N_{ym} + \dfrac{\partial w}{\partial x}N_{xym} \end{Bmatrix}$$

$$= \begin{bmatrix} N_{xm} & N_{xym} \\ N_{xym} & N_{ym} \end{bmatrix} \begin{Bmatrix} \dfrac{\partial w}{\partial x} \\ \dfrac{\partial w}{\partial y} \end{Bmatrix} = [N_m]\{G\} = [N_m][C_\theta]\{w_b\} \tag{2.31}$$

where matrix $[N_m]$ is constructed from vector $\{N_m\}$ per following definitions

$$\{ N_m \} = \begin{Bmatrix} N_{xm} \\ N_{ym} \\ N_{xym} \end{Bmatrix} = [A][C_m]\{w_m\}, \quad [N_m] = \begin{bmatrix} N_{xm} & N_{xym} \\ N_{xym} & N_{ym} \end{bmatrix} \tag{2.32}$$

Therefore, the components of the first order nonlinear stiffness matrices are defined as

$$[n1_{mb}] = [n1_{bm}]^T = \int_A [C_m]^T [A][\theta][C_\theta] \, dA \tag{2.34}$$

$$[n1_{nm}] = \int_A [C_\theta]^T [N_m][C_\theta] \, dA \tag{2.35}$$

From the definitions of $[\theta]$ and $[N_m]$, it is seen that $[n1_{nm}]$ is linearly dependent on $\{w_m\}$ and $[n1_{mb}]$ is linearly dependent on $\{w_b\}$.

Terms 7 and 10 can be combined and written as

Term 7 + Term 10

$$= \{\delta w_b\}^T [C_\theta]^T [\theta]^T [B][C_b]\{w_b\} + \frac{1}{2}\{\delta w_b\}^T [C_b]^T [B][\theta][C_\theta]\{w_b\}$$

$$= \frac{1}{2}\{\delta w_b\}^T [C_\theta]^T [\theta]^T [B][C_b]\{w_b\} + \frac{1}{2}\{\delta w_b\}^T [C_\theta]^T [\theta]^T [B][C_b]\{w_b\}$$

$$+ \frac{1}{2}\{\delta w_b\}^T [C_b]^T [B][\theta][C_\theta]\{w_b\}$$

$$= \frac{1}{2}\{\delta w_b\}^T [C_\theta]^T [N_b][C_\theta]\{w_b\} + \frac{1}{2}\{\delta w_b\}^T [C_\theta]^T [\theta]^T [B][C_b]\{w_b\}$$

$$+ \frac{1}{2}\{\delta w_b\}^T [C_b]^T [B][\theta][C_\theta]\{w_b\}$$

$$= \frac{1}{2}\{\delta w_b\}[n1_{nb}]\{w_b\}$$

$$= \frac{1}{2}\begin{Bmatrix} \delta w_b \\ \delta w_m \end{Bmatrix}^T \begin{bmatrix} n1_{nb} & 0 \\ 0 & 0 \end{bmatrix} \begin{Bmatrix} w_b \\ w_m \end{Bmatrix} \tag{2.36}$$

Another transformation also derived from Eqs. (2.9) and (2.18) is performed to simplify the expression of the complement matrix to the first order nonlinear stiffness matrix.

$$[\theta]^T[B][C_b]\{w_b\} = [\theta]^T\{N_b\} = \begin{bmatrix} \dfrac{\partial w}{\partial x} & 0 & \dfrac{\partial w}{\partial y} \\ 0 & \dfrac{\partial w}{\partial y} & \dfrac{\partial w}{\partial x} \end{bmatrix}\begin{Bmatrix} N_{xb} \\ N_{yb} \\ N_{xyb} \end{Bmatrix} = \begin{Bmatrix} \dfrac{\partial w}{\partial x}N_{xb}+\dfrac{\partial w}{\partial y}N_{xyb} \\ \dfrac{\partial w}{\partial y}N_{yb}+\dfrac{\partial w}{\partial x}N_{xyb} \end{Bmatrix}$$

$$= \begin{bmatrix} N_{xb} & N_{xyb} \\ N_{xyb} & N_{yb} \end{bmatrix}\begin{Bmatrix} \dfrac{\partial w}{\partial x} \\ \dfrac{\partial w}{\partial y} \end{Bmatrix} = [N_b]\{G\} = [N_b][C_\theta]\{w_b\} \qquad (2.37)$$

Similar to the evaluation of $[N_m]$ given in Eq. (2.32), the matrix $[N_b]$ is constructed from vector $\{N_b\}$ per following definitions

$$\{N_b\} = \begin{Bmatrix} N_{xb} \\ N_{yb} \\ N_{xyb} \end{Bmatrix} = [B][C_b]\{W_b\}, \quad [N_b] = \begin{bmatrix} N_{xb} & N_{xyb} \\ N_{xyb} & N_{yb} \end{bmatrix} \qquad (2.38)$$

From Eq. (2.36), the complement stiffness matrix to the first order nonlinear stiffness matrix is defined as

$$[n1_{nb}] = \int_A \left([C_\theta]^T[N_b][C_\theta] + [C_\theta]^T[\theta]^T[B][C_b] + [C_b]^T[B][\theta][C_\theta]\right)dA \qquad (2.39)$$

The second order nonlinear stiffness can be derived from the 6th term:

$$\frac{1}{2}\{\delta w_b\}^T[C_\theta]^T[\theta]^T[A][\theta][C_\theta]\{w_b\} = \frac{1}{3}\{\delta w_b\}^T[n2]\{w_b\} \qquad (2.40)$$

where
$$[n2] = \frac{3}{2}\int_A[B_\theta]^T[\theta]^T[A][\theta][B_\theta]\,dA \qquad (2.41)$$

It is seen that $[n2]$ is a quadratic function of $\{w_b\}$.

The rest three terms, terms 4, 8 and 12, are thermal effects terms. Term 8 gives the thermal effect stiffness matrix.

$$-\{\delta w_b\}^T[C_\theta]^T[\theta]^T\{N_{\Delta T}\} = -\{\delta w_b\}^T[C_\theta]^T\begin{bmatrix} \dfrac{\partial w}{\partial x} & 0 & \dfrac{\partial w}{\partial y} \\ 0 & \dfrac{\partial w}{\partial y} & \dfrac{\partial w}{\partial x} \end{bmatrix}\begin{Bmatrix} N_{x\Delta T} \\ N_{y\Delta T} \\ N_{xy\Delta T} \end{Bmatrix}$$

$$= -\{\delta w_b\}^T [C_\theta]^T \left\{ \begin{matrix} \dfrac{\partial w}{\partial x} N_{x\Delta T} + \dfrac{\partial w}{\partial y} N_{xy\Delta T} \\ \dfrac{\partial w}{\partial y} N_{y\Delta T} + \dfrac{\partial w}{\partial x} N_{xy\Delta T} \end{matrix} \right\} = -\{\delta w_b\}^T [C_\theta]^T \begin{bmatrix} N_{x\Delta T} & N_{xy\Delta T} \\ N_{xy\Delta T} & N_{y\Delta T} \end{bmatrix} \left\{ \begin{matrix} \dfrac{\partial w}{\partial x} \\ \dfrac{\partial w}{\partial y} \end{matrix} \right\}$$

$$= -\{\delta w_b\}^T [C_\theta]^T [N_{\Delta T}]\{G\} = -\{\delta w_b\}^T [C_\theta]^T [N_{\Delta T}][C_\theta]\{w_b\} \qquad (2.42)$$

Thus, the thermal effect stiffness matrix can be defined as

$$[k_{N\Delta T}] = \int_A [C_\theta]^T [N_{\Delta T}][C_\theta] \, dA \qquad (2.43)$$

where

$$[N_{\Delta T}] = \begin{bmatrix} N_{x\Delta T} & N_{xy\Delta T} \\ N_{xy\Delta T} & N_{y\Delta T} \end{bmatrix} \qquad (2.44)$$

Terms 4 and 12 give the thermal load vectors as

$$\{p_{m\Delta T}\} = -\int_A [C_m]^T \{N_{\Delta T}\} \, dA \qquad (2.45)$$

$$\{p_{b\Delta T}\} = -\int_A [C_b]^T \{M_{\Delta T}\} \, dA \qquad (2.46)$$

Now, the expression of internal virtual work can be rewritten in terms of above defined stiffness matrices as

$$\delta W_{int} = \left\{ \begin{matrix} \delta w_b \\ \delta w_m \end{matrix} \right\}^T \begin{bmatrix} k_b & k_{bm} \\ k_{mb} & k_m \end{bmatrix} \left\{ \begin{matrix} w_b \\ w_m \end{matrix} \right\} - \left\{ \begin{matrix} \delta w_b \\ \delta w_m \end{matrix} \right\}^T \begin{bmatrix} k_{N\Delta T} & 0 \\ 0 & 0 \end{bmatrix} \left\{ \begin{matrix} w_b \\ w_m \end{matrix} \right\} +$$

$$\frac{1}{2} \left\{ \begin{matrix} \delta w_b \\ \delta w_m \end{matrix} \right\}^T \begin{bmatrix} n1_{nm} & n1_{bm} \\ n1_{mb} & 0 \end{bmatrix} \left\{ \begin{matrix} w_b \\ w_m \end{matrix} \right\} + \frac{1}{2} \left\{ \begin{matrix} \delta w_b \\ \delta w_m \end{matrix} \right\}^T \begin{bmatrix} n1_{nb} & 0 \\ 0 & 0 \end{bmatrix} \left\{ \begin{matrix} w_b \\ w_m \end{matrix} \right\} \qquad (2.47)$$

$$+ \frac{1}{3} \left\{ \begin{matrix} \delta w_b \\ \delta w_m \end{matrix} \right\}^T \begin{bmatrix} n2 & 0 \\ 0 & 0 \end{bmatrix} \left\{ \begin{matrix} w_b \\ w_m \end{matrix} \right\} - \left\{ \begin{matrix} \delta w_b \\ \delta w_m \end{matrix} \right\}^T \left\{ \begin{matrix} p_{b\Delta T} \\ p_{m\Delta T} \end{matrix} \right\}$$

Virtual Work Done by External Forces

$$\delta W_{ext} = \int_V B_i \delta u_i dV + \int_{Surface} T_i \delta u_i dS$$

$$= \int_A \left[\delta w \left(-\rho h \frac{\partial^2 w}{\partial t^2} + \Delta p(x,y,t) \right) + \delta u \left(-\rho h \frac{\partial^2 u}{\partial t^2} \right) + \delta v \left(-\rho h \frac{\partial^2 v}{\partial t^2} \right) \right] dA \qquad (2.48)$$

where B_i is the body or inertial forces per volume and T_i is the surface traction per area.

In present work, the inertia forces and aerodynamic pressure $\Delta p(x,y,t)$ take effects. ρ is the mass density per unit area of the panel and h is the panel thickness.

Note that

$$\delta w = [H_w][T_b]\{\delta w_b\} \qquad \delta w = \delta w^T = \{\delta w\}^T [T_b]^T [H_w]^T$$

The first term of Eq. (2.48) can be expressed as

$$\int_A \delta w \left(-\rho h \frac{\partial^2 w}{\partial t^2} \right) dA = -\{\delta w_b\}^T \rho h [T_b]^T \int_A [H_w]^T [H_w] dA \, [T_b]\{\ddot{w}_b\}$$

$$= -\{\delta w_b\}^T \frac{1}{\omega_0^2} [m_b]\{\ddot{w}_b\} \qquad (2.49)$$

So that the mass matrix in bending can be defined as

$$[m_b] = \omega_0^2 \rho h [T_b]^T \int_A [H_w]^T [H_w] \, dA \, [T_b] = \frac{D_{110}}{a^4} [T_b]^T \int_A [H_w]^T [H_w] dA \, [T_b] \qquad (2.50)$$

where the reference frequency ω_0 is defined as

$$\omega_0 = \sqrt{\frac{D_{110}}{\rho h a^4}} \qquad (2.51)$$

D_{110} is the first entry of the laminate flexural stiffness [D] calculated when all of the fibers of the composite layers are aligned in the x-direction.

Simlilarly, the in-plane mass matrix can be acquired from the third and fourth terms in Eq. (2.48):

$$\int_A \left[\delta u \left(-\rho h \frac{\partial^2 u}{\partial t^2} \right) + \delta v \left(-\rho h \frac{\partial^2 v}{\partial t^2} \right) \right] dA$$

$$= -\{\delta w_m\}^T \rho h [T_m]^T \int_A \left([H_u]^T [H_u] + [H_v]^T [H_v] \right) dA [T_m]\{\ddot{w}_m\} \qquad (2.52)$$

$$= -\{\delta w_m\}^T \frac{1}{\omega_o^2} [m_m]\{\ddot{w}_m\}$$

thus

$$[m_m] = \frac{D_{110}}{a^4} [T_m]^T \int_A \left([H_u]^T [H_u] + [H_v]^T [H_v] \right) dA [T_m] \qquad (2.53)$$

The most important term in Eq. (2.48), obviously, is the second term that embodies the effects of airflow on the panel motion. The airflow applies significant damping effects by introducing a series of aerodynamic damping matrices into the governing EOM. By substituting the aerodynamic pressure given in Eq. (2.2), the second term of Eq. (2.48) becomes

$$\int_A \delta w \, \Delta p(x, y, t) \, dA$$

$$= \int_A \delta w \left\{ \frac{2q}{M} \left[\frac{1}{V} C_{1t} w_{,t} + C_{1x} w_{,x} + \frac{\gamma+1}{4} M \left(\frac{1}{V^2} C_{2t}^2 w_{,t}^2 + C_{2x}^2 w_{,x}^2 + \frac{2}{V} C_{2t} C_{2x} w_{,t} w_{,x} \right) \right. \right.$$

$$\left. \left. + \frac{\gamma+1}{12} M^2 \left(\frac{1}{V^3} C_{3t}^3 w_{,t}^3 + \frac{3}{V^2} C_{3t}^2 C_{3x} w_{,t}^2 w_{,x} + \frac{3}{V} C_{3t} C_{3x}^2 w_{,t} w_{,x}^2 + C_{3x}^3 w_{,x}^3 \right) \right] \right\} dA$$

$$(2.54)$$

Note that

$$w_{,x} = [H_w]_{,x} [T_b]\{w_b\} \qquad w_{,t} = [H_w][T_b]\{\dot{w}_b\}$$

Equation (2.54) can be further expanded into 9 terms so that

$$\int_A \delta w \, \Delta p(x,y,t) \, dA$$

$$= \{\delta w_b\}^T C_{1t} \frac{2q}{MV}[T_b]^T \int_A [H_w]^T[H_w] \, dA \, [T_b]\{\dot{w}_b\} \tag{2.55a}$$

$$+ \{\delta w_b\}^T C_{1x} \frac{2q}{M}[T_b]^T \int_A [H_w]^T[H_w]_{,x} \, dA \, [T_b]\{w_b\} \tag{2.55b}$$

$$+ \{\delta w_b\}^T C_{2t}^2 \frac{q(\gamma+1)}{2V^2}[T_b]^T \int_A (w_{,t})[H_w]^T[H_w] \, dA \, [T_b]\{\dot{w}_b\} \tag{2.55c}$$

$$+ \{\delta w_b\}^T C_{2t}C_{2x} \frac{q(\gamma+1)}{V}[T_b]^T \int_A (w_{,t})[H_w]^T[H_w]_{,x} \, dA \, [T_b]\{w_b\} \tag{2.55d}$$

$$+ \{\delta w_b\}^T C_{2x}^2 \frac{q(\gamma+1)}{2}[T_b]^T \int_A (w_{,x})[H_w]^T[H_w]_{,x} \, dA \, [T_b]\{w_b\} \tag{2.55e}$$

$$+ \{\delta w_b\}^T C_{3t}^3 \frac{q(\gamma+1)}{6V^3}M[T_b]^T \int_A (w_{,t}^2)[H_w]^T[H_w] \, dA \, [T_b]\{\dot{w}_b\} \tag{2.55f}$$

$$+ \{\delta w_b\}^T C_{3t}^2 C_{3x} \frac{q(\gamma+1)}{2V^2}M[T_b]^T \int_A (w_{,x}w_{,t})[H_w]^T[H_w] \, dA \, [T_b]\{\dot{w}_b\} \tag{2.55g}$$

$$+ \{\delta w_b\}^T C_{3x}^2 C_{3t} \frac{q(\gamma+1)}{2V}M[T_b]^T \int_A (w_{,x}w_{,t})[H_w]^T[H_w]_{,x} \, dA \, [T_b]\{w_b\} \tag{2.55h}$$

$$+ \{\delta w_b\}^T C_{3x}^3 \frac{q(\gamma+1)}{6}M[T_b]^T \int_A (w_{,x}^2)[H_w]^T[H_w]_{,x} \, dA \, [T_b]\{w_b\} \tag{2.55i}$$

Equation (2.55) is nondimensionalized with reference to the following parameters

Nondimensional dynamic pressure $\lambda = \dfrac{2qa^3}{MD_{110}}$ (2.56a)

Air-plate mass ratio $\mu = \dfrac{\rho_a a}{\rho h}$ (2.56b)

Aerodynamic damping coefficient $C_a \approx \dfrac{\mu}{M}$, for $M \gg 1$ (2.56c)

Aerodynamic damping
$$g_a = \frac{\rho_a V(M^2-2)}{\rho h \omega_0 (M^2-1)^{3/2}} \approx \sqrt{\lambda C_a} \qquad (2.56c)$$

Plate thickness-width ratio
$$r = \frac{h}{a} \qquad (2.56d)$$

Conduct the nondimensionalization and collect similar terms, Eq. (2.55) becomes

$$\int_A \delta w\, \Delta p(x,y,t)\, dA = -\{\delta w_b\}^T \frac{g_a}{\omega_0}([g]+[g1_t]+[g2_{bt}]+[g2_t])\{w_b\}$$

$$-\{\delta w_b\}^T \lambda([a]+[a1_t]+[a1_b]+[a2_{bt}]+[a2_b])\{w_b\} \qquad (2.57)$$

in which the matrices are defined as

$$[g] = C_{1t} \frac{D_{110}}{a^4}[T_b]^T \int_A [H_w]^T[H_w]dA\,[T_b] \qquad (2.58a)$$

$$[g1_t] = C_{2t}^2 \frac{\gamma+1}{4\omega_0 h}\sqrt{\frac{1}{\lambda}\frac{\mu}{M}}Mr\frac{D_{110}}{a^4}[T_b]^T \int_A (w_{,t})[H_w]^T[H_w]dA\,[T_b] \qquad (2.58b)$$

$$[g2_{bt}] = C_{3t}^2 C_{3x} \frac{\gamma+1}{4\omega_0 h^2}\sqrt{\frac{1}{\lambda}\frac{\mu}{M}}(Mr)^2\frac{D_{110}}{a^3}[T_b]^T \int_A (w_{,x}w_{,t})[H_w]^T[H_w]dA\,[T_b] \qquad (2.58c)$$

$$[g2_t] = C_{3t}^3 \frac{\gamma+1}{12\omega_0^2 h^2}\frac{1}{\lambda}\frac{\mu}{M}(Mr)^2\frac{D_{110}}{a^4}[T_b]^T \int_A (w_{,t})^2[H_w]^T[H_w]dA\,[T_b] \qquad (2.58d)$$

$$[a] = C_{1x} \frac{D_{110}}{a^3}[T_b]^T \int_A [H_w]^T[H_w]_{,x}dA\,[T_b] \qquad (2.58e)$$

$$[a1_t] = C_{2x}C_{2t} \frac{\gamma+1}{2\omega_0 h}Mr\sqrt{\frac{1}{\lambda}\frac{\mu}{M}}\frac{D_{110}}{a^3}[T_b]^T \int_A (w_{,t})[H_w]^T[H_w]_{,x}dA\,[T_b] \qquad (2.58f)$$

$$[a1_b] = C_{2t}^2 \frac{\gamma+1}{4h}Mr\frac{D_{110}}{a^2}[T_b]^T \int_A (w_{,x})[H_w]^T[H_w]_{,x}dA\,[T_b] \qquad (2.58g)$$

$$[a2_{bt}] = C_{3x}^2 C_{3t} \frac{\gamma+1}{4\omega_0 h^2}\sqrt{\frac{1}{\lambda}\frac{\mu}{M}}(Mr)^2\frac{D_{110}}{a^2}[T_b]^T \int_A (w_{,x}w_{,t})[H_w]^T[H_w]_{,x}dA\,[T_b] \qquad (2.58h)$$

$$[a2_b] = C_{3x}^3 \frac{\gamma+1}{12 \, h^2} (Mr)^2 \frac{D_{110}}{a} [T_b]^T \int_A (w_{,x})^2 [H_w]^T [H_w]_{,x} \, dA \, [T_b]$$ (2.58i)

Collecting the terms given in Eqs. (2.49), (2.52) and (2.57), the external virtual work can be expressed in matrix form as

$$\delta W_{ext} = -\frac{1}{\omega_o^2} \begin{Bmatrix} \delta w_b \\ \delta w_m \end{Bmatrix}^T \begin{bmatrix} m_b & 0 \\ 0 & m_m \end{bmatrix} \begin{Bmatrix} \ddot{w}_b \\ \ddot{w}_m \end{Bmatrix} - \frac{g_a}{\omega_o} \begin{Bmatrix} \delta w_b \\ \delta w_m \end{Bmatrix}^T \begin{bmatrix} [g]+[g1_t]+[g2_{bt}]+[g2_t] & 0 \\ 0 & 0 \end{bmatrix} \begin{Bmatrix} \dot{w}_b \\ \dot{w}_m \end{Bmatrix}$$

$$-\lambda \begin{Bmatrix} \delta w_b \\ \delta w_m \end{Bmatrix}^T \begin{bmatrix} [a]+[a1_t]+[a1_b]+[a2_{bt}]+[a2_b] & 0 \\ 0 & 0 \end{bmatrix} \begin{Bmatrix} w_b \\ w_m \end{Bmatrix}$$ (2.59)

Governing Equation of Motion

Applying the principle of virtual work with the matrix form expressions of virtual works, the equation that reflects the equilibrium of the finite element can be established as

$$\frac{1}{\omega_o^2} \begin{bmatrix} m_b & 0 \\ 0 & m_m \end{bmatrix} \begin{Bmatrix} \ddot{w}_b \\ \ddot{w}_m \end{Bmatrix} + \frac{g_a}{\omega_o} \left(\begin{bmatrix} [g]+[g1_t]+[g2_{bt}]+[g2_t] & 0 \\ 0 & 0 \end{bmatrix} \right) \begin{Bmatrix} \dot{w}_b \\ \dot{w}_m \end{Bmatrix} +$$

$$\left(\lambda \begin{bmatrix} [a]+[a1_t]+[a1_b]+[a2_{bt}]+[a2_b] & 0 \\ 0 & 0 \end{bmatrix} \right) + \begin{bmatrix} k_b & k_{bm} \\ k_{mb} & k_m \end{bmatrix} - \begin{bmatrix} k_{N\Delta T} & 0 \\ 0 & 0 \end{bmatrix} +$$

$$\frac{1}{2} \left(\begin{bmatrix} [n1_{nm}]+[n1_{nb}] & [n1_{bm}] \\ [n1_{mb}] & 0 \end{bmatrix} \right) + \frac{1}{3} \begin{bmatrix} n2 & 0 \\ 0 & 0 \end{bmatrix} \right) \begin{Bmatrix} w_b \\ w_m \end{Bmatrix} = \begin{Bmatrix} p_{b\Delta T} \\ p_{m\Delta T} \end{Bmatrix}$$ (2.60)

Assembling all the elements and applying the boundary conditions, the system level equation of motion can be written as

$$\frac{1}{\omega_o^2} \begin{bmatrix} M_b & 0. \\ 0 & M_m \end{bmatrix} \begin{Bmatrix} \ddot{W}_b \\ \ddot{W}_m \end{Bmatrix} + \frac{g_a}{\omega_o} \left(\begin{bmatrix} [G]+[G1_t]+[G2_{bt}]+[G2_t] & 0 \\ 0 & 0 \end{bmatrix} \right) \begin{Bmatrix} \dot{W}_b \\ \dot{W}_m \end{Bmatrix} +$$

$$\left(\lambda \begin{bmatrix} [A_a]+[A1_t]+[A1_b]+[A2_{bt}]+[A2_b] & 0 \\ 0 & 0 \end{bmatrix} \right) + \begin{bmatrix} K_b & K_{bm} \\ K_{mb} & K_m \end{bmatrix} - \begin{bmatrix} K_{N\Delta T} & 0 \\ 0 & 0 \end{bmatrix} +$$

$$\frac{1}{2}\left(\begin{bmatrix} [N1_{Nm}]+[N1_{Nb}] & [N1_{bm}] \\ [N1_{mb}] & 0 \end{bmatrix}+\frac{1}{3}\begin{bmatrix} N2 & 0 \\ 0 & 0 \end{bmatrix}\right)\begin{Bmatrix} W_b \\ W_m \end{Bmatrix}=\begin{Bmatrix} P_{b\Delta T} \\ P_{m\Delta T} \end{Bmatrix}$$

or simply

$$\frac{1}{\omega_o^2}[M]\{\ddot{W}\}+\frac{g_*}{\omega_o}[G_{NL}]\{\dot{W}\}+\left(\lambda[A_{NL}]+[K_o]-[K_{N\Delta T}]+\frac{1}{2}[N1]+\frac{1}{3}[N2]\right)\{W\}=\{P_{\Delta T}\}$$

$$(2.61)$$

2.3 EOM in Modal Coordinates

2.3.1 Transform into Modal Coordinates

The expansion theorem states that any possible motion of the system can be described as a linear combination of the modal vectors. Therefore, the real deflection of the panel can be assumed as

$$\{W\}=\begin{Bmatrix} W_b \\ W_m \end{Bmatrix}=\sum_{i=1}^{n} q_r(t)\begin{Bmatrix} q_{br} \\ q_{mr} \end{Bmatrix}=\sum_{r=1}^{n} q_r(t)\{\phi_r\}=[\Phi]\{q\} \qquad (2.62)$$

In Eq. (2.62), $q_r(t)$ is the modal coordinates of the r-th mode, which reflects the contribution to the ensemble deflection from the r-th mode. And $[\Phi] = [\{\phi_1\}, \{\phi_2\}, ...,$ $\{\phi_r\}, ..., \{\phi_n\}]$ is the modal matrix, where $\{\phi_r\}$ is the mode shape of the r-th mode. The linear mode shapes are constructed from following linear eigenanalysis

$$\frac{\omega^2}{\omega_0^2}[M]\{\phi\}=[K_o]\{\phi\} \qquad (2.63)$$

The transformation of system governing EOM, Eq. (2.61), into modal coordinates is achieved by substituting Eq. (2.62) into Eq. (2.61) and pre-multiplying the whole equation by $[\Phi]^T$. The transformed EOM in modal coordinates can be written in a brief form as follows

$$\frac{1}{\omega_0^2}[\overline{M}]\{\ddot{q}\}+\frac{g_\star}{\omega_0}[\overline{G}_{NL}]\{\dot{q}\}+\left(\lambda[\overline{A}_{NL}]+[\overline{K}]+\frac{1}{2}[\overline{N1}]+\frac{1}{3}[\overline{N2}]\right)\{q\}=[\Phi]^T\{P_{\Delta T}\} \qquad (2.64a)$$

where

$$[\overline{M}]=[\Phi]^T[M][\Phi] \qquad [\overline{G}_{NL}]=[\Phi]^T[G_{NL}][\Phi] \qquad (2.64b)$$

$$([\overline{A}_{NL}],[\overline{K}],[\overline{N1}],[\overline{N2}])=[\Phi]^T([A_{NL}],[K_o]-[K_{N\Delta T}],[N1],[N2])[\Phi] \qquad (2.64c)$$

2.3.2 Evaluation of Nonlinear Matrices

As noted from the definitions, the first/second order nonlinear stiffness matrices, the aerodynamic stiffness matrices, and aerodynamic damping matrices are dependent on the nodal displacement vectors $\{W_b\}$ or $\{W_m\}$. While transferred into modal coordinates, all these nonlinear matrices can be evaluated with modal coordinates.

The first and second order nonlinear stiffness matrices, [N1] and [N2], can be evaluated as

$$[N1]=\sum_{r=1}^{n}q_r[N1]^{(r)} \qquad [N2]=\sum_{r=1}^{n}\sum_{s=1}^{n}q_r q_s[N2]^{(rs)} \qquad (2.65)$$

where

$$[N1]^{(r)}=\sum_{\substack{\text{all elements}\\+\text{bdy. conds.}}}\begin{bmatrix}[n1_{nm}]^{(r)}+[n1_{nb}]^{(r)} & [n1_{bm}]^{(r)}\\ [n1_{mb}]^{(r)} & 0\end{bmatrix}$$

$$[N2]^{(rs)}=\sum_{\substack{\text{all elements}\\+\text{bdy. conds.}}}\begin{bmatrix}[n2]^{(rs)} & 0\\ 0 & 0\end{bmatrix}$$

The superscript r denotes that $\{\phi_r\}$ is used in evaluation of the first-order nonlinear modal stiffness matrix. Similarly, the superscript rs denotes that $\{\phi_r\}$ and $\{\phi_s\}$ are used in evaluation of the second-order nonlinear modal stiffness matrix. The nonlinear modal

stiffness matrices, $[N1]^{(r)}$ and $[N2]^{(rs)}$, are constant. The corresponding transformed matrices, $\lfloor \overline{N1} \rfloor$ and $\lfloor \overline{N2} \rfloor$, are computed from definitions given in Eqs. (2.64b) and (2.64c).

The nonlinear matrices appeared in aerodynamic stiffness matrix $[A_{NL}]$ and aerodynamic damping matrix $[G_{NL}]$ are functions of $w, \dfrac{\partial w}{\partial x}$, or $\dfrac{\partial w}{\partial t}$. From an early definition given in Eq. (2.4), it is inferred that

$$w_{,x} = [H_w]_{,x}[T_b]\{w_b\} = \sum_{r=1}^{n} q_r [H_w]_{,x}[T_b]\{\phi_{br}\}$$ (2.66a)

$$w_{,t} = [H_w][T_b]\{\dot{w}_b\} = \sum_{r=1}^{n} \dot{q}_r [H_w][T_b]\{\phi_{br}\}$$ (2.66b)

$$w_{,x}w_{,t} = w_{,x}^T w_{,t} = \left(\sum_{r=1}^{n} q_r [H_w]_{,x}[T_b]\{\phi_{br}\} \right)^T \left(\sum_{s=1}^{n} \dot{q}_s [H_w][T_b]\{\phi_{bs}\} \right)$$

$$= \left(\sum_{r=1}^{n} q_r \{\phi_{br}\}^T [T_b]^T [H_w]_{,x}^T \right) \left(\sum_{s=1}^{n} \dot{q}_s [H_w][T_b]\{\phi_{bs}\} \right)$$ (2.67c)

$$= \sum_{r=1}^{n} \sum_{s=1}^{n} \left(q_r \dot{q}_s \{\phi_{br}\}^T [T_b]^T [H_w]_{,x}^T [H_w][T_b]\{\phi_{bs}\} \right)$$

$$w_{,x}^2 = \sum_{r=1}^{n} \sum_{s=1}^{n} \left(q_r q_s \{\phi_{br}\}^T [T_b]^T [H_w]_{,x}^T [H_w]_{,x}[T_b]\{\phi_{bs}\} \right)$$ (2.67d)

$$w_{,t}^2 = w_{,t}^T w_{,t} = \sum_{r=1}^{n} \sum_{s=1}^{n} \left(\dot{q}_r \dot{q}_s \{\phi_{br}\}^T [T_b]^T [H_w]^T [H_w][T_b]\{\phi_{bs}\} \right)$$ (2.67e)

The above quantities are all that is needed for evaluation of element level aerodynamic pressure induced matrices, $[a1_t]$, $[a1_b]$, $[a2_{bt}]$, $[a2_b]$, $[g1_t]$, $[g2_{bt}]$, and $[g2_t]$. Attention must be paid that the mode shapes, $\{\phi_{br}\}$ or $\{\phi_{bs}\}$, are bending

related entries in the entire mode shape eigenvectors in Eq. (2.62). This is on basis of following relationship

$$\{W_b\}=(\{\phi_{b1}\} \ \ \{\phi_{b2}\} \ \ \cdots \ \ \{\phi_{bn}\})\begin{Bmatrix} q_1 \\ q_2 \\ \cdots \\ q_n \end{Bmatrix}=[\Phi_b]\{q\}=\sum_{r=1}^{n} q_r\{\phi_{br}\}=\sum_{r=1}^{n}\{W_{br}\} \qquad (2.68)$$

Generally, during the time integration, the modal coordinate q_r and corresponding velocity $\dot{q}_r$ are generated simultaneously. Hence, they are available at each time step for updating the nonlinear matrices. Resembling the evaluation procedure for [N1] and [N2], the nonlinear aerodynamic effects matrices can be evaluated as

$$[G1_t]=\sum_{r=1}^{n}\dot{q}_r[G1_t]^{(r)} \qquad (2.69a)$$

$$[G2_{bt}]=\sum_{r=1}^{n}\sum_{s=1}^{n}q_r\dot{q}_s[G2_{bt}]^{(rs)} \qquad (2.69b)$$

$$[G2_t]=\sum_{r=1}^{n}\sum_{s=1}^{n}\dot{q}_r\dot{q}_s[G2_t]^{(rs)} \qquad (2.69c)$$

$$[A1_t]=\sum_{r=1}^{n}\dot{q}_r[A1_t]^{(r)} \qquad (2.69d)$$

$$[A1_b]=\sum_{r=1}^{n}q_r[A1_b]^{(r)} \qquad (2.69e)$$

$$[A2_{bt}]=\sum_{r=1}^{n}\sum_{s=1}^{n}q_r\dot{q}_s[A2_{bt}]^{(rs)} \qquad (2.69f)$$

$$[A2_b]=\sum_{r=1}^{n}\sum_{s=1}^{n}q_r q_s[A2_b]^{(rs)} \qquad (2.69g)$$

Again, constant matrices $[G1_t]^{(r)}$, $[G2_{bt}]^{(rs)}$, $[G2_t]^{(rs)}$, $[A1_t]^{(r)}$, $[A1_b]^{(r)}$, $[A2_{bt}]^{(rs)}$, and

$[A2_b]^{(rs)}$ are constructed by assembling contributions from all elements and the kinematic

boundary conditions.

2.4 EOM for Isotropic, Symmetrically Laminated Panels

For symmetrically laminated composite and isotropic panels, the extensional-bending

coupling matrix [B] vanishes. Examining definitions given in Eqs. (2.29) and (2.39) tells

that matrices $[K_{mb}]$, $[K_{bm}]$, and $[N1_{Nb}]$ become null. This fact helps to simplify the

governing EOM of Eq. (2.61). Since the in-plane vibration is typically of high frequency,

which needs more energy to activate than lower frequency bending modes, and the modes

in concern are principally low order bending modes, in-plane inertia terms can be

neglected. With this approximation, the in-plane displacement vector $\{W_m\}$ could be

expressed as a function of bending displacement vector $\{W_b\}$ as follows

$$\{W_m\} = [K_m]^{-1}\{P_{m\Delta T}\} - \frac{1}{2}[K_m]^{-1}[N1_{mb}]\{W_b\} = \{W_m\}_0 + \{W_m\}_2$$

$$\{W_m\}_0 = [K_m]^{-1}\{P_{m\Delta T}\}, \qquad \{W_m\}_2 = -\frac{1}{2}[K_m]^{-1}[N1_{mb}]\{W_b\}$$

(2.70)

note that $\{W_m\}_0$ is constant and $\{W_m\}_2$ is actually a quadratic function of $\{W_b\}$ because

$[N1_{mb}]$ is linearly dependent on $\{W_b\}$.

Now, by substituting $\{W_m\}$ given in Eq. (2.70) into the Eq. (2.61), the system EOM

for isotropic and symmetrically laminated composite can be written in terms of bending

displacement vector $\{W_b\}$ only

$$\frac{1}{\omega_o^2}[M_b]\{\ddot{W}_b\} + \frac{g_a}{\omega_o}[G_{NL}]\{\dot{W}_b\} + \left(\lambda[A_{NL}] + [K_b] - [K_{N\Delta T}] + \frac{1}{2}[N1_{Nm}] \right)$$

$$+\frac{1}{3}[N2]-\frac{1}{4}[N1_{bm}][K_m]^{-1}[N1_{mb}]\Big)\{W_b\}+\frac{1}{2}[N1_{bm}][K_m]^{-1}\{P_{m\Delta T}\}=\{P_{b\Delta T}\} \quad (2.71)$$

The in-plane motion affects the panel stiffness through an additional quadratic nonlinear stiffness term and through the load vector term that is linearly dependent on $\{W_b\}$.

To transform into modal coordinates, a previous assumption stated in Eq. (2.68) is employed to conduct the transformation. Executing the same procedure applied to achieve Eq. (2.64), Eq. (2.71) becomes

$$\frac{1}{\omega_o^2}[\overline{M}_b]\{\ddot{q}\}+\frac{g_a}{\omega_o}[\overline{G}_{NL}]\{\dot{q}\}+(\lambda[\overline{A}_{NL}]+[\overline{K}]+[K_{qq}])\{q\}=\{F\} \quad (2.72a)$$

where

$$[\overline{M}_b]=[\Phi_b]^T[M_b][\Phi_b], \qquad \{F\}=[\Phi_b]^T\{P_{b\Delta T}\} \quad (2.72b)$$

$$[\overline{G}_{NL}]=[\Phi_b]^T\Big([G]+\sum_{r=1}^{n}q_r[G1_t]^{(r)}+\sum_{r=1}^{n}\sum_{s=1}^{n}(q_r\dot{q}_s[G2_{bt}]^{(rs)}+\dot{q}_r\dot{q}_s[G2_t]^{(rs)})\Big)[\Phi_b] \quad (2.72c)$$

$$[\overline{A}_{NL}]=[\Phi_b]^T\Big([A_a]+\sum_{r=1}^{n}(\dot{q}_r[A1_t]^{(r)}+q_r[A1_b]^{(r)})$$

$$+\sum_{r=1}^{n}\sum_{s=1}^{n}(q_r\dot{q}_s[A2_{bt}]^{(rs)}+q_rq_s[A2_b]^{(rs)})\Big)[\Phi_b] \quad (2.72d)$$

$$[\overline{K}]=[\Phi_b]^T\Big([K_b]-[K_{N\Delta T}]+\frac{1}{2}[N1_{Nm}]_o\Big)[\Phi_b] \quad (2.72e)$$

$$[K_{qq}]=[\Phi_b]^T\Big(\sum_{r=1}^{n}\sum_{s=1}^{n}q_rq_s(\frac{1}{2}[N1_{Nm}]_2^{(rs)}+\frac{1}{3}[N2]^{(rs)}-\frac{1}{4}[N1_{bm}]^{(r)}[K_m]^{-1}[N1_{mb}]^{(s)})\Big)[\Phi_b]$$

$$=[\Phi_b]^T\Big(\sum_{r=1}^{n}\sum_{s=1}^{n}(q_rq_s[K_{qq}]^{(rs)})\Big)[\Phi_b] \quad (2.72f)$$

The superscript r denotes that $\{\phi_{br}\}$ is used and the superscript rs denotes that $\{\phi_{br}\}$ and $\{\phi_{bs}\}$ are used in evaluation of the matrices.

In Eq. (2.72), the nonlinear stiffness matrix $[N1_{Nm}]$ is split into two parts: $[N1_{Nm}]_o$ and $[N1_{Nm}]_2$. The reason for doing so is that in Eq. (2.70), $\{W_m\}$ consists of a constant part, $\{W_m\}_o$, and a second order part, $\{W_m\}_2$. Subsequently, $[N1_{Nm}]_o$ is evaluated with $\{W_m\}_o$, and the $[N1_{Nm}]_2^{(rs)}$ is computed from $\{W_m\}_2^{(rs)}$, which is expressed in modal coordinates as

$$\{W_m\}_2^{(rs)} = -\frac{1}{2}[K_m]^{-1}[N1_{mb}]^{(r)}\{\phi_{bs}\} \tag{2.73}$$

Clearly, $[N1_{Nm}]_o$ is constant and $[N1_{Nm}]_o$ is a quadratic function of nodal displacement vector $\{W_b\}$.

CHAPTER III

SOLUTION PROCEDURES

In this chapter, the system governing EOM, Eq. (2.64) or (2.72), is solved in time domain through numerical integration. Based upon the time history computed, flutter response as well as possible chaotic motions of the panel are investigated with the assistance of numerical diagnosis tools. Some practical issues pertinent to implementation of the computation work are discussed in detail.

3.1 Flutter Response

Evaluation of the response of nonlinear systems almost inevitably involves some type of numerical integration. Therefore, the most straightforward approach to study flutter response of panels is to examine the time history response generated from numerical integration of the governing EOM. The proposed application of the modal reduction technique into hypersonic flutter analysis makes it feasible and affordable to explore the panel motion through a large amount of numerical integration experiments.

3.1.1 Time Integration

On performing the direct integration of the equilibrium equation, many time integration methods are available [115], such as the central difference method, the Houbolt method, the Newmark method, etc. Herein, the fourth order Runge-Kutta method is adopted.

Numerical integration is carried out most conveniently in terms of first-order equations, so that the dynamic equations of motion must be recast in state-space form. Another benefit is that the modal coordinate velocity $\dot{q}_r$ that is required for evaluation of nonlinear aerodynamic effect matrices is included in the state vector directly.

Pre-multiply Eq. (2.64a) with $[\overline{M}]^{-1}\omega_o^2$,

$$\{\ddot{q}\}+g_a\omega_o[\overline{M}]^{-1}[\overline{G}_{NL}]\{\dot{q}\}+\omega_o^2[\overline{M}]^{-1}\left(\lambda[\overline{A}_{NL}]+[\overline{K}]+\frac{1}{2}[\overline{N1}]+\frac{1}{3}[\overline{N2}]\right)\{q\}=\omega_o^2[\overline{M}]^{-1}[\Phi]^T\{P_{\Delta T}\}$$

$$(3.1)$$

the state vector can be defined as

$$\{X\}=\begin{Bmatrix}\{X_1\}\\\{X_2\}\end{Bmatrix}=\begin{Bmatrix}\{q\}\\\{\dot{q}\}\end{Bmatrix}\quad\Rightarrow\quad\{\dot{X}\}=\begin{Bmatrix}\{\dot{X}_1\}\\\{\dot{X}_2\}\end{Bmatrix}=\begin{Bmatrix}\{\dot{q}\}\\\{\ddot{q}\}\end{Bmatrix}\qquad(3.2)$$

Thus, the state space representation of governing EOM is

$$\begin{Bmatrix}\{\dot{X}_1\}\\\{\dot{X}_2\}\end{Bmatrix}=f(\{x\},t)=\begin{bmatrix}0 & [I]\\-[K_{sys}] & -[C_{sys}]\end{bmatrix}\begin{Bmatrix}\{X_1\}\\\{X_2\}\end{Bmatrix}+\begin{bmatrix}0\\[I]\end{bmatrix}\{F_{sys}\}\qquad(3.3)$$

in which, the system stiffness and damping matrices are defined as

$$[K_{sys}]=\omega_o^2[\overline{M}]^{-1}\left(\lambda[\overline{A}_{NL}]+[\overline{K}]+\frac{1}{2}[\overline{N1}]+\frac{1}{3}[\overline{N2}]\right)\qquad(3.4)$$

$$[C_{sys}]=g_a\omega_o[\overline{M}]^{-1}[\overline{G}_{NL}]\qquad(3.5)$$

$$\{F_{sys}\}=\omega_o^2[\overline{M}]^{-1}[\Phi]^T\{P_{\Delta T}\}\qquad(3.6)$$

Matrix [I] is the identity matrix.

The basic steps for performing fourth order Runge-Kutta (RK4) integration scheme can be found in many books [116]. Observing the fundamental theory of RK4, following computation steps should be executed to produce the time response history of the panel

Step 1. Given initial condition $\{X_o\}$ and nondimensional dynamic pressure λ.

Step 2. Prepare the system stiffness matrix $[K_{sys}]$, damping matrix $[C_{sys}]$ and load vector $\{F_{sys}\}$. Start from iteration $i = 0$.

Step 3. Construct the nonlinear aerodynamic effect matrices and nonlinear structure stiffness matrices using state vector $\{X_i\}$,

Step 4. Compute the coefficients needed for evaluation of the state vector $\{X_{i+1}\}$.

$$k_1 = \Delta t f(\{X_i\}, t_i) \tag{3.7a}$$

$$k_2 = \Delta t f\left(\{X_i\} + a_{21} k_1, t_i + \frac{1}{2}\Delta t\right) \tag{3.7b}$$

$$k_3 = \Delta t f\left(\{X_i\} + a_{31} k_1 + a_{32} k_2, t_i + \frac{1}{2}\Delta t\right) \tag{3.7c}$$

$$k_4 = \Delta t f(\{X_i\} + a_{41} k_1 + a_{42} k_2 + a_{43} k_3, t_i + \Delta t) \tag{3.7d}$$

for classical RK4, $a_{21} = 0.5$, $a_{31} = 0.0$, $a_{32} = 0.5$, $a_{41} = 0.0$, $a_{42} = 0.0$ and $a_{43} = 1.0$.

Step 5. Compute the state vector at time instant t_{i+1}.

$$\{X_{i+1}\} = \{X_i\} + \alpha_1 k_1 + \alpha_2 k_2 + \alpha_3 k_3 + \alpha_4 k_4 \tag{3.8}$$

For classical RK4, $\alpha_1 = 1/6$, $\alpha_2 = 1/3$, $\alpha_3 = 1/3$ and $\alpha_4 = 1/6$.

Step 6. Recover the real response of the structure through the relationship given by Eq. (2.62), $\{W\} = [\Phi]\{q\}$ and output the time history as well as other quantities if needed.

Step 7. Check if $i \geq NPT$, if not, let $i = i+1$ and go to step 3, otherwise stop.

3.1.2 Critical Buckling Temperature

The high temperature that the surface panel experiences gives highly possible rise to the structure instability due to thermal buckling. Thermal buckling only happens when isotropic or symmetrically laminated plates are heated uniformly. But for any plate acted by thermal moments, the plate will deform. For the latter case, there is neither buckling phenomenon nor an associated critical buckling temperature. For the current study, the critical buckling temperature is used as a reference for the case of a plate with thermal moments. The procedure to determine the critical buckling temperature can be found in related literature, such as Yang and Han [74] and Shi and Mei [117]. For an isotropic or symmetrically laminated plate heated uniformly, the critical buckling temperature is (see Appendix B for detailed formulation)

$$\Delta T_{cr} = \mu_1 \Delta T_{ini} \tag{3.9}$$

where ΔT_{ini} is an arbitrary initial temperature change and μ_1 is the lowest eigenvalue of thermal buckling found from the eigenproblem

$$[K_b]\{\phi\} = \mu([K_{N\Delta T}] - [N1_{Nm}])\{\phi\} \tag{3.10}$$

where $\{\phi\}$ is the corresponding buckling mode shape.

3.2 Motion Types - Observation and Diagnosis

The aerodynamic pressure and the temperature are two control parameters that determine the final category of the panel motion. The present hypersonic flutter analysis is not focused on the flutter boundary, which conventionally can be determined with supersonic flutter analysis using linear aerodynamics theory [127]. Beyond the commencement of flutter, when the flow speed increases to the hypersonic region, the

motion of the panel could be either large amplitude LCO (simple harmonic, periodic) or chaos. Hence, issues like the amplitude of LCO, the boundary marks the start of chaos and various evolution routes of chaos will be highlighted.

3.2.1 Diagnosis Tools

As suggested by Dowell [90] and Moon [79], the following diagnosis tools are necessary for detecting chaotic motion.

1. Time histories

2. Phase plane plot

3. Power spectral densities (PSD) or Fourier spectrum of the signal

4. Poincaré maps

Of the four descriptors, time history is the most straightforward means to attain an impression of the motion style. However, it is tricky to detect long-period or quasi-periodic vibration where two or more incommensurate periodic signals are present through the time history only. Phase plane plot is more informative upon this point, but, the trajectory of the orbits will tend to fill up the phase plane so that information about the attractors is submerged inside. The use of Poincaré map, which is a snapshot of the phase plane plot triggered by a certain event, will "develop" portraits of the attractors easily. The PSD or Fourier spectrum provides information about frequency spectrum of the time history. For system of low dimension (one to three DOF), broaden of frequency spectrum is easy to recognize so that beginning of chaos is tracked. But, for system of high dimension, the frequency spectrum is broad (many spikes for various frequency components) even though periodic vibration is ongoing.

The motion of a specific point on the panel, the node located at the cross of ¾ length (x direction) line and mid-width (y direction) line, is monitored as a representative of the entire plate motion. The time history of the transverse deflection, w, at this node is recorded. The phase plane plot is constructed with w as one axis and its corresponding velocity, $\dot{w}$, as the other axis.

The motive of using Poincaré map is to acquire certain qualitative and quantitative information about the system by studying the evolution of state variables at discrete times, which is different from the phase plane plot that records the changes of state variables at continuous time instants. In an n-state variable problem, one can obtain a Poincaré section by measuring the n-1 variables when the nth variable reaches some particular value or when the phase space trajectory crosses some arbitrary plane in phase space. The specific node under study possesses six DOF. It is possible to recover the velocities for each DOF from those of each modal coordinates using a relationship derived from Eq. (2.62)

$$\{\dot{W}\}=[\Phi]\{\dot{q}\}$$
(3.11)

In fact, Eq. (3.11) is used for constructing phase plane plot. Therefore, there are 13 state variables, including time t, available for plotting a 12-dimension Poincaré map. However, it is not necessary to build such a complicate and abstract map since the pair of transverse displacement w and transverse velocity $\dot{w}$ can be treated as a good representative of the rest. That means actually a 3-dimensional state space, (w, $\dot{w}$, t) , is taken as example to build a 2-dimensional Poincaré map, which is mathematically referred to as a reduced map [118].

The crucial question for constructing Poincaré map is the choice of the discrete instants of time, or the occasion for penetrating a plane into the phase space. For a nonautonomous system, the system is generally driven by a force with a prescribed period T. Obviously and reasonably, the stroboscope is switched on at an interval of mT (m = 0, 1, 2, 3, ...) to intercept desired Poincaré map. Whereas for an autonomous system that the flutter problem belongs to, the period of the driving force is unascertainable. It is suggested [79, 90] that an event, instead of a fixed time interval, should be defined so that the occurrence of this event will trigger the stroboscope to capture a portrait of the state space. In general, these events will not occur at equal time intervals. Indeed they may occur at chaotic time intervals. Actually, a successful choice for a nonautonomous system can be understood as an event defined as whenever the periodic driving force achieves its maximum magnitude. The specific event for present instance is defined as being the passage of the velocity of the plate at the ¾ length node through zero from the positive direction. At the occurrence of the defined event, the transverse deflection at the ¾ length node and the deflection at plate center node are recorded for sketching the Poincaré map. This is not the unique acceptable event definition. Choice of an suitable event is highly pertinent to the problem under study and purpose of such study.

The pattern of Poincaré maps reflect the motion type of the system. As classified by Moon [90], following mapping relationships can be taken as criteria for further judgement:

Finite number of points   periodic or subharmonic oscillations

Closed curve   quasiperiodic, two incommensurate frequencies present

Open curve   suggest modeling as a one-dimensional map; try plotting $x(t)$ versus $x(t+T)$

Fractal collection of points   Strange attractor in three phase-space dimensions

Fuzzy collection of points   (i) dynamical systems with too much random or noisy input; (ii) strange attractor but system has very small dissipation- use Lyapunov exponent; (iii) strange attractor in phase space with more than three dimensions — try multiple Poincaré; (iv) quasiperiodic motion with three or more dimension incommensurate frequencies

3.2.2 Bifurcation Diagram

A widely used technique for examining the prechaotic and postchaotic changes in a dynamic system under parameter variations is the bifurcation diagram. Phase plane plot, Poincaré map, time series and power spectra provide information about the dynamics of the system for specific values of the system control parameters, herein the nondimensional dynamic pressure λ and the temperature ΔT. The dynamics may also be viewed more globally over a range of parameter values, thereby allowing simultaneous comparison of periodic and chaotic behavior. The bifurcation diagram provides a summary of the essential dynamics and is therefore a useful method of acquiring this overview.

Despite that the theories about bifurcation are somewhat profound, the construction of the bifurcation diagram is rather simple. There is an internal relationship between Poincaré map and bifurcation diagram. The event defined for Poincaré map is also utilized to activate recording the maximum plate deflection at the ¾ length node. Another axis of the bifurcation diagram, the control parameter axis, is taken as either the nondimensional pressure λ or the temperature ΔT. Therefore, the bifurcation behavior of the fluttering plate is studied along two paths: one is bifurcation at certain flow speed value versus variations of plate temperature, the other case is bifurcation of a plate heated up to a specific temperature level versus changes of flow speed.

The typical types of bifurcation that can be observed from bifurcation diagram are: the saddle-node (or fold, tangent) bifurcation, the Hopf bifurcation, the pitchfork bifurcation and the period-doubling (or flip) bifurcation. Nice illustrations of above bifurcations in phase plane portraits, Poincaré map and bifurcation diagram can be found in plenty of books [80, 81, 119-121]. An illustrated guide to above bifurcations without any mathematical support is given by Abraham and Shaw [119] and Abraham, Abraham and Shaw [120]. Illustrations and typical examples of each type of bifurcation can be found in the book by Thompson and Stewart [80]. Some related research findings are collected by Thompson and Bishop [81]. Extensive mathematical treatments of some or all of abovementioned bifurcations are given in Guckeheimer and Holems [118], Chen and Leung [94] and Hale and Koçak [121]. The four types of bifurcation belong to the local bifurcations that concerns primarily about the bifurcations of fixed points of vector fields and maps. There exist global bifurcations [82, 122] that describe qualitative changes in the orbit structure of an extended region of the phase plane. The associate

theories and tools are not as sophisticated as those for the local bifurcations yet. The local bifurcations are mainly investigated herein to explore various routes to chaos.

The most important information about the evolution of chaos that can be probed by using of bifurcation diagram is the various routes to chaos. Since the discovery of the strange attractor by Lorenz in 1963 [77], four typical routes leading to chaos have been discovered [79, 94].

(1) Period doubling route to chaos. The most celebrated scenario for chaotic vibration. The typical bifurcation phenomenon belongs to this category is the period-doubling (flip) bifurcation, which shows the transition from period one motion to period two motion.

(2) Quasiperiodic route (also named as secondary Hopf bifurcation route) to chaos. Occurrence of the Hopf bifurcation symbolizes such this route. Two or more closed curves, indicating two or more incommensurate periods, are the typical image shown in the corresponding Poincaré map.

(3) Intermittent transition route to chaos. Long periods of periodic motion with bursts of chaos observed. The behavior of the system seems to switch back and forth between two qualitatively different behaviors even though all the control parameters remain constant. Two major types of intermittence are that system behavior switches between periodic and chaotic motion for the first type, whereas, between periodic and quasiperiodic for the second.

(4) Breaking of the KAM (Kolmogorov-Arnold-Mosor) torus route to chaos. The typical observation is that according to the KAM theorem [94], the phase space portraits of the quasi-Hamiltonian system are distributed on two KAM tori

(one embedded in the other), but between the two tori there exists a chaotic region. Unlike the first three routes, the mechanisms for this route remains to be solved. This fourth route will not be in consideration herein because chaos due to broken KAM torus exists for two-dimensional system only.

As stated above, mechanisms for the first three routes to chaos have all been clear in theory. Thus, identifying a particular prechaotic pattern matching these well-developed models with assistance of Poincaré map and bifurcation diagram will help with a better mathematical and physical understanding of the chaotic phenomena.

3.2.3 Lyapunov Exponent

The defining feature of chaos is its sensitive dependence upon initial conditions (SDIC). The Lyapunov exponent is a measure of the sensitivity of the system to changes in initial conditions. A straightforward understanding of this exponent can be illustrated through the definition of Lyapunov exponent for one-dimensional map. Given the time series $x(t_o)$, $x(t_1)$, $x(t_2)$, ..., which can be labeled as x_0, x_1, x_2, ... If the system is behaving chaotically, the divergence of nearby trajectories in phase space will manifest itself in an exponentially increasing way. Assume x_i is an arbitrarily selected value from the sequences of x's, and x_j is another value in the sequence that is close (theoretically, should be infinitesimally close) to x_i. The distances are defined as

$$d_o = |x_j - x_i|$$

$$d_1 = |x_{j+1} - x_{i+1}|$$

$$d_2 = |x_{j+2} - x_{i+2}|$$

(3.12)

$$\vdots$$

$$d_n = |x_{j+n} - x_{i+n}|$$

Then, the exponential increase is described as

$$d_n = d_o e^{\lambda_1 n}$$

(3.13)

The divergence rate, λ_1, is defined as Lyapunov exponent

$$\lambda_1 = \frac{1}{n} \log_2 \left(\frac{d_n}{d_o} \right)$$

(3.14)

where subscript 2 means base 2 logarithm.

For a n-dimensional system, there exists a spectrum of n Lyapunov exponents. The long-term evolution of an infinitesimal n-sphere of initial conditions is monitored to evaluate the Lyapunov exponents for deformed principal axes. The initial sphere will become ellipsoid due to the expanding and extracting along the principal axes. The i-th one-dimensional Lyapunov exponent is defined in terms of the length of the ellipsoidal principal axis $p_i(t)$ (Wolf et al. [102])

$$\lambda_i = \lim_{t \to \infty} \frac{1}{t} \log_2 \frac{p_i(t)}{p_i(0)}$$

(3.15)

Usually, the λ_i's are ordered so that $\lambda_1 > \lambda_2 > \dots$.

The signs of the Lyapunov exponents indicate what kind of motion the system is undergoing. For the motion described by one-dimensional map, there is only one Lyapunov exponent. A negative exponent corresponds to a periodic limit cycle motion or

fixed point, null exponent means a marginal stable motion or two-torus, and positive exponent indicates chaotic motion. For an n-dimensional system, the largest Lyapunov exponent, λ_1, is used as an indicator of chaos. Again, positive λ_1 indicates chaos. Some sign patterns of multi-dimensional dissipative system Lyapunov exponent spectrum could provide more detailed information about the type of attractor, such as for a three-dimensional spectrum, sign pattern (+, 0, -) corresponds to a strange attractor (chaos); (0, 0, -) is for a two-torus; (0, -, -) means a LCO and (-, -, -) stands for a fixed point.

In present study, only the largest Lyapunov exponent λ_1 is of interest to find the boundary values of control parameters that cause chaos. As mentioned before, the time series used for calculation is actually a one-dimensional map. A program for computing the largest Lyapunov exponent from a time series given in a paper by Wolf et al. [102] is employed. The detailed algorithm, which is not among the scope of current study, is also given in the paper. All components of a Lyapunov exponent spectrum could be computed from governing equations of motion like Eq. (2.64). However, herein it is not necessary to compute all Lyapunov exponents in the spectrum (if n modes are used, there will be n Lyapunov exponents in the spectrum) since the sign of the largest exponent is sufficient for chaos diagnosis purpose.

3.3 Computation Considerations

3.3.1 Convergence Study and Mode Selection Strategy

There are two essential issues prior to the commencement of all computation efforts. The first issue is the convergence study. Convergence studies must be conducted to reveal the effects of mesh sizes and the number of modes on accuracy of time integration.

The final selection of mesh size and mode number will be made on a converged time response of the panel in representative working environment.

Another important issue that accompanies the mode number convergence study is the selection of modes. When airflow is parallel to the length of the panel as shown in Fig. 2.1(a), theoretically, infinite number of modes are activated. For analytical approaches, such as the popularly used Galerkin's method for flutter analysis, and finite element modal formulation, in essence certain mode shape functions/vectors are assumed. Especially if the assumed mode shapes are sine wave or sine-wave like, mode (m, n) means that the mode shape is a compound of m half sine waves along the panel length and n half sine wave along the width. Choice of modes is generally in language of such integer pairs. The guideline of choice is to keep those dominant modes so that the number of modes to be kept to a minimum with reasonable accurate response.

There are some discussions about this issue in the literature. Dowell [7, 123] indicated that six linear modes, (1,1), (2,1) to (6,1), give quite accurate results for LCO in supersonic panel flutter analysis. More recent research has unveiled the complexity of mode selection. Weiliang and Dowell [124] found that more than one spanwise mode is required for sufficient analysis of LCO response for the cantilever isotropic plate. Lee et al. [125] encountered difficulty of tracking frequency coalescing modes when temperature effects are involved. They adopted a mode tracking scheme to follow modes that will coalesce. Chandirmani and Librescu [62], in their study of laminated nonlinear panel flutter using third order piston theory, used 4×1 modes (4 chordwise modes and 1 spanwise mode) for the case of airflow parallel to the panel chord, and 2×2 modes for the case of in-plane angularity. Their work is primarily to search for the flutter boundary that

the phenomenon of frequency coalescence is utilized. Therefore, only the modes that are possible to be involved with frequency coalescence are concerned. Whereas, Nydick et al. [59] stated that for hypersonic flutter analysis of an orthotropic panel using numerical integration, which is the approach employed in present study, up to 8×1 modes are necessary to achieve modal convergence at high flow speed. Their conclusion was made on basis of a careful modal convergence study and is highly advisable to present study.

Another difficulty in mode selection that is specific to flutter analysis of orthotropic or laminated panels is the identification of modes. For analytical approaches, the modes are pre-assumed so that employment of modes (m, n) means simply including the corresponding mode shape function into the expansion series. In finite element analysis, referring to the formulation in chapter two, the modes are solved from eigenanalysis. So, if the conclusions about mode selection from analytical approach are used as guidance, the first step is to identify the high order modes (m, n). Usually this is accomplished through plots of mode shapes, i.e., eigenvectors. The anisotropic properties of the panel make this procedure very difficult to perform since it is hard to count the number of modes along panel length and/or width.

The mode selection strategy adopted here is based upon the concept of modal participation factor (see also Abdel-Motaglay et al. [126]). The modal participation factor of r-th mode, η_r, is defined as

$$\eta_r = \frac{\max|q_r|}{\sum_{s=1}^{n}|q_s|} \qquad (3.16)$$

The basic idea is to filter out the trivial modes according to the value of modal participation factor. To avoid examining a large amount of modes at the same time, the

filtering procedure is conducted in a step by step way as described below (the modes are ordered by ascending of frequency as a result of eigenanalysis):

1. Choose several representative flow speed and temperatures. The simulated LCO amplitudes will be examined.

2. Use the first 20 modes for numerical integration.

3. Record the LCO amplitudes for each case (specific flow speed and temperature).

4. Check the modal participation factors for each mode and discard modes with contribution less than certain level, such as one percent. Introduce more modes (to make up the total number to be 20), which are of higher order than the tested 20 modes, and repeat the numerical integration.

5. Record the LCO amplitudes and compare with previous results for convergence check.

6. If the LCO amplitudes for all cases have converged, the modes used for most recent step should be the final choice. If not converged, go to step 4.

The above procedure assures that the selected modes include all influential modes and give converged LCO amplitude. Since at each round 20~25 modes are involved, it is fairly convenient to reach a final mode selection pattern in a few rounds. It is unnecessary to plot the mode shapes and identify the (m, n) pairs. Apparently, the above 20-mode-base procedure can be modified to be a 10-mode-base or 25-mode-base procedure if necessary.

3.3.2 Computation Cost Reduction

Modal reduction technique reduces the computation cost in the following aspects:

3.4 Flowchart

A schematic flowchart summarizing abovementioned solution procedure is given in Fig. 3.1. There are some points need further explanation:

(1) The flowchart illustrates the integration route of changing average temperature T_o continuously with a fixed nondimensional dynamic pressure λ. It is very easy to be modified to the route of continuous changing λ and fixed temperature level. The second route is also employed in numerical study.

(2) The temperature distribution could be uniform ($T_1 = 0$) or with nonzero temperature gradient ($T_1 \neq 0$). The temperature gradient is not changing continuously like the average temperature does.

(3) The transient response is filtered by a control parameter NPT1. All result data files record the truncated data sets that are after the NPT1 integration points (NPT1* Δt seconds).

(4) The programs used for Lyapunov exponent calculation is not from reference [102]. Instead, updated programs provided by Dr. Alan Wolf, BASGEN and FET, are used. BASGEN is for database generation and FET is for evaluation of the largest Lyapunov exponent with fixed evolution time.

START

INITIALIZATION

Mesh size; Number of modes, nt, and modes to use;

Panel support boundary conditions; material properties;

Nondimensional dynamic pressure λ; Temperature gradient;

Aerodynamic damping coefficient;

Average temperature range: $T_o = 0 \sim nT_r * \Delta T_r$;

For composite, specify lamination angles;

Time integration points NPT, transient response filtering points NPT1;

Integration time step size Δt;

Switch variables for different order of the Piston's theory

Construct [A], [B], [D] matrices.

Composite panel	Isotropic panel
Use Eqs. (2.16a), (2.16b) and (2.16c)	Use Eq. (2.17)

Assemble constant matrices:

$[K_b]$, $[K_m]$, $[K_{bm}]$ — Eqs. (2.27) ~ (2.29)

$[K_{N\Delta T}]$ — Eq. (2.243)

$[G]$, $[A_a]$, — Eqs. (2.58a), (2.58e)

$[M_b]$, $[M_m]$ — Eqs. (2.50), (2.53)

A

(A)

Perform the linear eigenanalysis

$$\omega^2[M]\{\phi\} = [K_o]\{\phi\} \qquad (2.63)$$

Construct the mode shape matrix $[\Phi]$

Normalize the mode shape matrix $[\Phi]$

with maximum component set to one

For isotropic/symmetrically laminated panels:

Solve the thermal buckling eigenproblem

$$[K_b]\{\phi\} = \mu([K_{N\Delta T}] - [N1_{Nm}])\{\phi\} \qquad (3.10)$$

for ΔT_{cr}

DO I = 1, nt

Assemble $[N1]^{(i)}$ using $\{\phi_i\}$, refer to Eqs. (2.34),

(2.35) and (2.39). Save $[\Phi]^T\{N1\}^{(i)}[\Phi]$.

For iso/sym panels, save $[N1_{bm}]^{(i)}$

Assemble $[G1_d]^{(i)}$, $[A1_d]^{(i)}$ and $[A1_b]^{(i)}$ using $\{\phi_i\}$,
$\{\phi_j\}$. Refer to Eq. (2.58b), (2.58f) and (2.58g).
Save $[\Phi]^T([G1_d]^{(i)}, [A1_d]^{(i)}, [A1_b]^{(i)})[\Phi]$.

(C)

(B)

```
        ( C )
          │
          ▼
┌─────────────────────┐
│   DO  JJ = 1, nTr   │◄──────────────┐
└─────────────────────┘               │
          │                           │
          ▼                           │
┌──────────────────────────┐          │
│  ΔT = ΔTo + nTr * ΔTr     │          │
└──────────────────────────┘          │
          │                           │
          ▼                           │
┌──────────────────────────────────┐  │
│ Assemble [KNΔT] and {PΔT}, referring │
│ to Eqs. (2.43), (2.45) and (2.46). │  │
└──────────────────────────────────┘  │
          │                           │
          ▼                           │
┌──────────────────────────────────┐  │
│ Evaluate |K̄| using Eq. (2.64c). For │
│ iso./sym. Panels, use Eq. (2.72c).│  │
└──────────────────────────────────┘  │
          │                           │
          ▼                           │
┌──────────────────────────────────┐  │
│ Given initial condition {Xo}      │  │
└──────────────────────────────────┘  │
          │                           │
          ▼                           │
┌─────────────────────┐               │
│   DO  I = 1, NPT     │◄──────────┐   │
└─────────────────────┘            │   │
          │                        │   │
          ▼                        │   │
┌──────────────────────────────────────────┐
│ Extract modal coordinates {q} and velocity {q̇} from │
│ present state vector {Xi}. Evaluate nonlinear matrices │
│ |ĀNL|, |ḠNL|, |N1| and |N2|, see Eqs. (2.64), (2.65) │
│ and (2.69).                                │
│ For iso./sym. panels, see Eqs. (2.72). Compute [Kqq] │
│ according to Eq. (2.72f).                  │
└──────────────────────────────────────────┘
          │
          ▼
        ( F )
```

(D)   (E)

$\Delta T = \Delta T_o + nTr * \Delta Tr$

Assemble $[K_{N\Delta T}]$ and $\{P_{\Delta T}\}$, referring to Eqs. (2.43), (2.45) and (2.46).

Evaluate $|\bar{K}|$ using Eq. (2.64c). For iso./sym. Panels, use Eq. (2.72c).

Given initial condition $\{X_o\}$

DO I = 1, NPT

Extract modal coordinates $\{q\}$ and velocity $\{\dot{q}\}$ from present state vector $\{X_i\}$. Evaluate nonlinear matrices $|\bar{A}_{NL}|$, $|\bar{G}_{NL}|$, $|N1|$ and $|N2|$, see Eqs. (2.64), (2.65) and (2.69).
For iso./sym. panels, see Eqs. (2.72). Compute $[K_{qq}]$ according to Eq. (2.72f).

D   E   F

$$[K_{sys}] = \omega_o^2 [\overline{M}]^{-1}\left(\lambda[\overline{A}_{NL}] + [\overline{K}] + \frac{1}{2}[\overline{N1}] + \frac{1}{3}[\overline{N2}]\right) \quad (3.4)$$

$$[C_{sys}] = g_a \omega_o [\overline{M}]^{-1}[\overline{G}_{NL}] \quad (3.5)$$

$$\{F_{sys}\} = \omega_o^2 [\overline{M}]^{-1}[\Phi]^T\{P_{\Delta T}\} \quad (3.6)$$

$$\left\{\begin{matrix}\{\dot{X}_1\}\\\{\dot{X}_2\}\end{matrix}\right\} = f(\{x\}, t) = \begin{bmatrix}0 & [I]\\-[K_{sys}] & -[C_{sys}]\end{bmatrix}\left\{\begin{matrix}\{X_1\}\\\{X_2\}\end{matrix}\right\} + \begin{bmatrix}0\\[I]\end{bmatrix}\{F_{sys}\} \quad (3.3)$$

$$k_1 = \Delta t f(\{X_i\}, t_i) \quad (3.7a)$$

$$k_2 = \Delta t f\left(\{X_i\} + \frac{1}{2}k_1, t_i + \frac{1}{2}\Delta t\right) \quad (3.7b)$$

$$k_3 = \Delta t f\left(\{X_i\} + \frac{1}{2}k_2, t_i + \frac{1}{2}\Delta t\right) \quad (3.7c)$$

$$k_4 = \Delta t f(\{X_i\} + k_3, t_i + \Delta t) \quad (3.7d)$$

$$\{X_{i+1}\} = \{X_i\} + \frac{1}{6}k_1 + \frac{1}{3}k_2 + \frac{1}{3}k_3 + \frac{1}{6}k_4 \quad (3.8)$$

The real response of the panel can be recovered as

$$\{W\} = [\Phi]\{q\} \qquad \{\dot{W}\} = [\Phi]\{\dot{q}\}$$

where $\{q\}$ and $\{\dot{q}\}$ are from $\{X_{i+1}\}$

D   E   G

(D) (E) (G)

$I > NPT1$? — No

Yes

Export (*time*, $W_{3/4}/H$) for time history.

Export ($W_{3/4}/H$, $\dot{W}_{3/4}/H$) for phase plane portrait.

Poincaré event activated? — No

Yes

Export ($W_{3/4}/H$, W_c/H) for Poincaré map.

Export (ΔT, $W_{3/4}/H$) for bifurcation diagram.

Store time history data for calculation of Lyapunov Exponent.

$\{X_i\} = \{X_{i+1}\}$

Continue

(D) (H)

Fig. 3.1 Flow chart

CHAPTER IV

RESULTS AND DISCUSSION

The primary objective of this study is to develop a finite element time domain modal method for evaluation of panel flutter at hypersonic airflow. The formulation and corresponding solution procedure has been addressed in detail in prior chapters. This chapter is to present numerical results from implementation of the presented time domain modal method. The first step is taken to validate the finite element formulation through comparisons with available analytical or numerical panel flutter analysis results. The method is subsequently applied to the flutter analysis of six types (Table 4.1) of panels. Special attention is paid to practical implementation issues, which are the essential elements for proper application of the modal method. It is necessary to be noted that due to the advantage of finite element method, the proposed method is not limited to the material properties, supporting conditions, panel geometry (as long as it is a thin panel) and lamination layout that are quoted herein.

4.1 Validation of the Finite Element Formulation

As reviewed in the first chapter, a vast amount of literature has been focused on linear panel flutter analysis and nonlinear panel flutter analysis with linear aerodynamics. Among the major concerns of all studies, the dynamic pressure λ for flutter and LCO amplitudes are two fundamental topics since that the former directly provides design criteria and the latter is very helpful to panel fatigue life analysis. The first numerical study example is to compare λ and LCO amplitudes determined by present finite element

approach with results cited from Dowell [26], Fig.19. The switch variables, C_{1t}, C_{1x}, C_{2t}, C_{2x}, C_{3t}, and C_{3x}, are set as 1, 1, 0, 0, 0, 0 to achieve linear aerodynamic pressure described by the first order piston theory. There exists equivalence between the in-plane loads considered by Dowell [26] and the thermal loading considered here. When the panel is heated up uniformly to a temperature level of $\Delta T_o/\Delta T_{cr}$, the uniform compressive force developed at mechanical supports is $-R_x/\pi^2$, as employed by Dowell [26] for in-plane compressive force. Observing this relationship, the λ versus LCO amplitudes for a simply supported isotropic square panel at thermal loading of $\Delta T_o/\Delta T_{cr} = 0.0$, 1.0, 2.0 are compared to corresponding results from Dowell [26] at in-plane force levels of $R_x/\pi^2 = 0.0$, -2.0, -4.0. Figure 4.1 shows the comparisons. Dowell [26] employed six modes along flow direction, (1, 1), (2,1), ..., (6, 1), for the direct numerical integration. The finite element approach used also six flow direction modes and a 12×8 mesh size based upon a mesh convergence study, not shown here for brevity. For the case of no thermal loading $\Delta T_o/\Delta T_{cr} = 0.0$, $R_x/\pi^2 = 0.0$, the critical dynamic pressure determined by Dowell is 540.5 (as read from figure) and the finite element approach gives 542.0 when $\Delta\lambda$ is taken to be 1.0. For the other two temperature levels, $\Delta T_o/\Delta T_{cr} = 1.0$, 2.0, finite element analyses give λ_{cr} of 365.0 and 205.0, and values of 364.5 and 204.5 are read from Fig. 19 in the paper by Dowell [26]. It is seen that good agreement was reached. Since the accuracy of graph reading cannot be ensured, comparison up to digit accuracy is too foot to proceed. From Fig. 4.1, it is also concluded that using 12×8 meshes, and 6 linear vibration modes, finite element gives almost the same LCO amplitudes as given by Dowell's six-mode analytical solution procedure.

Incorporation of nonlinear aerodynamic terms into the panel flutter analysis results in flutter motions exhibit several unique characteristics that differ the hypersonic panel flutter from supersonic flutter. Instances of such identifying behavior for hypersonic panel flutter response were exposed early by Eastep and McIntosh [56] and their findings were summarized in the literature review section of Chapter I. Here, one visually straightforward example of these special characteristics, the bias of LCO into the cavity, is examined using the simply supported isotropic square panel as an object. Figure 4.2 shows that at a high airflow speed, $\lambda = 2000$ as quoted, using the first order piston theory, the panel moves the same amount away from its center plane ($z = 0$) into the flow as into the cavity, say $W_{max}/H = \pm 2.34$, as illustrated in Fig. 4.2(a). When third order piston theory is used, the bias of motion into the cavity can be observed clearly from Fig. 4.2(b), where in the airflow side, $W_{max}/H = 2.08$, and in the cavity side, $W_{max}/H = -2.50$. This observation of motion bias is a good evidence to say that nonlinear aerodynamic terms do make significant difference and the proposed finite element time domain modal formulation is capable of capturing such difference.

Although limited, there are some LCO amplitudes results from hypersonic panel flutter analysis available in literature. The second comparison was then made for LCO amplitudes of panel flutter in hypersonic flow between present finite element analysis results and selected results by Gray and Mei [9] using finite element frequency domain LUM/NTF method and by Nydick et al. [59] using analytical PDE Galerkin method and direct numerical integration. Figure 4.3 shows the comparisons. The LCO amplitudes for both single layer ([0]) and double layer ([0/90]) B/Al square panels were obtained by Gray and Mei [9] using an 8×8 mesh (8×4 half-plate mesh). Whereas, an 12×8 mesh is

employed in present study based upon the mesh convergence study that will be set forth in a later paragraph. It is also noticed that the two-layer panel belongs to unsymmetrical lamination that has a nonzero bending-extension [B] matrix and the single layer panel is with a null [B] matrix. Evaluations of LCO amplitudes for these two panels of same material, same geometry, same support condition, different lamination scheme are then performed with different formulations put forth in sections 2.3 and 2.4. Figure 4.3 tells that very good agreements are found between the finite element frequency domain method and time domain modal approach for both the symmetrically laminated panel and the unsymmetrically laminated panel case. For the analytical approach adopted by Nydick et al. [59], it is necessary to choose which mode to be used for assuming the panel deflection in space domain using the Galerkin method. This is a common issue that is also encountered while applying the present finite element time domain modal approach. Nydick et al. [59] conducted elaborate comparisons for LCO amplitudes obtained from analyses using various numbers of modes and concluded that an 8×1 (i.e., eight flow direction modes, (1,1), (2,1), ..., (8,1), are used) mode selection pattern would give converged LCO amplitudes. A detailed mode convergence study based upon conclusions from mode filtering procedure is carried out as preparation work for the entire solution procedure suggests that for the single layer B/Al panel, up to 13 modes are needed for accurate LCO amplitude evaluation. Modes other than those along flow direction modes (i.e., mode m×1, m = 1, 2, 3, ...) may have significant contribution to the ensemble panel oscillation according to modal participation computation results. Details about the mode convergence study and implementation of mode filtering will be illustrated through two instances later in this chapter. In a summary, comparisons made in

Fig. 4.3 proved that the finite element frequency domain method developed by Gray and Mei [9], the analytical approach used by Nydick et al. [59] and the finite element time domain modal formulation presented herein agree well with one another on solutions of LCO amplitudes of panel flutter at hypersonic airflow. The good agreement achieved also demonstrated the validity of the proposed strategy of mode selection through mode filtering procedure.

4.2 Flutter of Isotropic Panels

Thin panels made of isotropic materials, such as aluminum and its alloys, titanium and its alloys, have earned extensive applications in aircraft design since the very beginning of aerospace engineering. Besides their potential high strength and/or light weight, the simplicity of material properties greatly ease the corresponding analyses work. The main purpose of studying the flutter response of isotropic panels in hypersonic flow is to get a first impression on what the hypersonic airflow can do to the thin panels of the flight vehicles.

For all case studies followed, the 24-DOF Bogner-Fox-Schmit C^1 conforming finite element is utilized for discretization of the panel since the formulation was based upon (but not limited to) this type of element. For curved panel or panel with initial imperfection, shell elements such as MIN6 finite element are suggested. The panels are assumed to be simply supported that implies boundary conditions of $w(0, y) = w(a, y) = w(x, 0) = w(x, b) = 0$, $w_{,xx}(0, y) = w_{,xx}(a, y) = w_{,yy}(x, 0) = w_{,yy}(x, b) = 0$. The in-plane boundary conditions for all cases are assumed to be the so-called "immovable"

denotes the product of Mach number and panel geometry constant $r = h/a$. It is seen that the thermal loading for the isotropic panel is $\Delta T_0/\Delta T_{cr} = 1.3 > 1.0$ but the panel motion is tranquilized by the airflow so that no buckling occurs. As temperature increases, the aerodynamic pressure becomes insufficient to repel the occurrence of buckling so that the panel is buckled into certain shape, and if aerodynamic pressure is not high, it is possible that the panel keeps its buckling shape without any vibration. This is the "buckled but dynamically stable" status, as termed by Dowell [26]. As the dynamic pressure (flow speed) increases further, flutter will take place and the rest three dynamically unstable motions run onto the stage. The simplest motion of these three is the simple harmonic LCO as shown in Fig. 4.5. Simple harmonic LCO is a type of sine wave like motion that has a single period, in the other word, one dominating nonlinear frequency. In the Poincaré map, this single period is projected as one point (the Poincaré map of "blown flat" behavior is also one point, but the point has null coordinates). In the phase plane, a closed elliptic orbit represents the repeatability of this kind of motion. Figure 4.6 shows a period-2 motion that can be easily identified in its Poincaré map (points A and B stand for the existence of two periods). Motions with more than two periods are also possible and usually increase of periods will finally cause chaos. Periodic motion owns more than one dominating vibration frequencies and they are not harmonics of one another. Both the simple harmonic motion and periodic motion are oscillations within a limited bound so that they are also termed as simple harmonic LCO and periodic LCO, respectively. The most complicated of the five types is obviously the chaos. As shown in Fig. 4.7, the time history of chaotic motion is highly random and its phase plane is crowded with non-repeating orbits. Typical Poincaré map shows a fractal pattern as shown in Fig. 4.7(c).

Projections of all trails occupy an irregular domain of the map and there are no any hints of the existence of periods. It is worthy to clarify that even without in-plane thermal/mechanical loading effects, a fluttering panel could develop chaos when flow speed is high (see Nydick et al. [59]). However, it is true that thermal/mechanical loads could result in chaos at low flow speed since the snap-through phenomenon after buckling is also highly nonlinear and nonlinearity is among the major causes to chaos (Moon [79]).

4.2.2 Bifurcation and Routes to Chaos

Because of the high nonlinearity inherent with hypersonic panel flutter, chaos becomes inevitable as system control parameters, i.e., the temperature and the dynamic pressure, change. It is therefore interesting to observe the route that chaos evolve via bifurcation diagram, as introduced in Chapter III. Figure 4.8 is the first example of bifurcation diagram chosen on purpose to observe the route to chaos for the simply supported aluminum panel. Figure 4.9 is a close view of the pitchfork bifurcation cascade. Apparently, at $\lambda = 1100$, the panel takes a period-doubling route (see previous section 3.2.2) to evolve into chaos. For a better understanding, the phase plane plots and Poincaré maps for representative control parameter values, $\Delta T_0/\Delta T_{cr} = 3.0, 3.5, 4.5, 5.1$, and 5.4, are presented in Fig. 4.10 and Fig. 4.11. Observed from Fig. 4.10 and Fig. 4.11, at $\Delta T_0/\Delta T_{cr} = 3.0$, the panel undergoes a period one LCO motion. As the temperature increases to $\Delta T_0/\Delta T_{cr} = 3.5$, in phase plane the closed single connection orbit in Fig. 4.10(a) bifurcates into two orbits as shown in Fig. 4.10(b), correspondingly, the single point in Poincaré of Fig. 4.11(a) bifurcates into two points as shown in Fig. 4.11(b). The

pitchfork bifurcation continues as temperature amplitude increases. The period-2 motion bifurcates into period-4 motion, as shown in Fig. 4.10(c) and Fig. 4.11(c), and period-4 motion then bifurcates into period-8 motion, as shown in Fig. 4.10(d) and Fig. 4.11(d). In Fig. 4.10(d), the further bifurcated eight orbits are crowded at the right half plane that implies further bifurcation may cause disturbance between different orbits. Fig. 4.10(e) illustrates that bifurcation from the period-8 motion results in diffusion of orbits in a finite area that is typical for chaotic motion. In Poincaré maps shown in Fig. 4.11(d) and (e), the eight points grow into a fractal patch in the map as shown in Fig. 4.15(e). Pitchfork bifurcation is not the only bifurcation behavior observed during the chaos study undertaken here. Typically, the Hopf bifurcation is also encountered when λ changes from a value lower than λ_{cr} to $\lambda > \lambda_{cr}$, i.e., the panel undergoes the transition from flat panel to LCO motion.

Another phenomenon observed in Fig. 4.8 and Fig. 4.9 is the post-chaos characteristics. It is seen that at temperature ratio $\Delta T_o / \Delta T_{cr}$ between 5.65 and 5.75, the matured chaos disappeared and periodic motion revives, as indicated in the phase plane plot of Fig. 4.10(f) and Poincaré map Fig.4.11(f). Same phenomenon of transition from chaos to periodic motion was also observed by Dowell [90] while studying the chaotic motions of a buckled beam at supersonic flow. The rejuvenation of post-chaos periodic motion does not sustain long as temperature ration increases. It is observed that at $\Delta T_o / \Delta T_{cr}$ between 5.75 and 5.80, chaos appears again. The background principle governing this chaos to periodic motion and then return to chaos is not yet known exactly and needs further research.

Period-doubling pitchfork bifurcation is not the only route. Figure 4.12 shows the bifurcation diagram for $\lambda = 2500.0$ and this type of bifurcation diagram is typical for high λ region. The chaos occurs at a $\Delta T_o/\Delta T_{cr}$ value falls between 4.0 and 4.5 with a gradually broaden area in the bifurcation diagram. Visual judgement about at what specific value of temperature ratio chaos starts becomes very difficult, compared with the legible bifurcation points in Fig. 4.9. The evaluation of the largest Lyapunov exponent (refer to previous section 3.2.3) is then introduced for assistance of determining the start point of chaos. Figures 4.13 and 4.14 illustrate the Lyapunov exponent calculation results for selected $\Delta T_o/\Delta T_{cr}$ ratios, i.e. $\lambda = 1100.0$, $\Delta T_o/\Delta T_{cr} = 5.0$, 5.1 and 5.2, $\lambda = 2500.0$, $\Delta T_o/\Delta T_{cr} = 4.1, 4.2, 4.3$. Comparing the bifurcation diagram in Fig. 4.9 and the Lyapunov exponents in Fig. 4.13, it is easy to conclude that the chaos for aluminum panel at $\lambda = 1100.0$ starts when temperature ratio reaches $\Delta T_o/\Delta T_{cr} = 5.2$ because the Lyapunov exponents at $\Delta T_o/\Delta T_{cr} = 5.0$, 5.1 are null, which denotes LCO, and for $\Delta T_o/\Delta T_{cr} = 5.2$ the Lyapunov exponent jumps to 28.0, which indicates chaotic motion. Similarly, review of bifurcation diagram given in Fig. 4.12 and Lyapunov exponents illustrated in Fig. 4.24 tells that at $\lambda = 2500.0$, the chaos occur when the temperature ratio is $\Delta T_o/\Delta T_{cr} = 4.3$. Evidently, use of the largest Lyapunov exponent calculations in conjunction with bifurcation diagrams will provide an efficient and precise means to capture the critical points for chaos commencement and/or post-chaos periodic LCO. The compound use of bifurcation diagram and Lyapunov exponent is applied to all chaos study cases followed.

c

4.3 Flutter of Orthotropic Panels

Over the years, orthotropic panels of various materials, geometries and supporting conditions have been chosen as an example to exploit the mechanisms, characteristics of the dynamic motions of fundamental structural components. The reason is two-fold. Firstly, orthotropic panels have extensive applications in many industries including aerospace structures and this makes related research very informative and meaningful. On the other hand, the simplicities (of course, more complicated than isotropic material) in material properties are preferable for convenient analytical or numerical analysis to be conducted. Strictly speaking, the B/Al Metal Matrix Composite (MMC) panel belongs to orthotropic panel and it had extensive applications in airplane surface panels, airframe struts design. Such an orthotropic panel is then taken as an example to demonstrate all types of complicate flutter behaviors of panels at hypersonic airflow.

The investigations on the effect of nonlinear aerodynamic terms that involved in piston theories are given to show the importance of including influential terms while doing hypersonic panel flutter analysis. Influences of some important system parameters, such as temperature gradient, aerodynamic damping, and Mach number, on the flutter response are also examined.

4.3.1 Mode Selection, Mode Convergence and Mesh Convergence

So far, the importance of mode selection and mode convergence study has been emphasized for several times. The essence of this issue is that any modal reduction technique assumes an approximation to the true solution of the physical problem. A good assumption on modes to use leads to an accurate simulation and a bad one causes loss of

veracity. As a common sense in dynamics, structure vibration is usually dominated by low frequency modes. However, for a fluttering panel at hypersonic flow, the airflow provides the energy source for activating high order modes so that they may play a more significant role. The motive of proposing the mode filtering procedure as the guidance for mode selection is to identify those modes really contributes much to the vibration. The modal participation factor, as defined in Eq. (3.16), is the gauge to assist the judgement of influence of a certain mode on the ensemble motion. As one of the major objectives of current research, effort must be made on developing a practical tool for engineering application. Hence, a systematic scheme for mode selection for the finite element time domain modal formulation is highly demanded.

The mode filtering procedure for a simply supported, single layer [0], $12'' \times 12'' \times 0.04''$, B/Al panel is executed by observing the general guidelines put forth in section 3.3.1. As the first step, an initial run with a broad range of nondimensional dynamic pressures, $\lambda = 1000.0 \sim 5000.0$, has been conducted and the results showed that non-periodic or chaotic motions possibly occur at the range of $\lambda = 3000.0 \sim 5000.0$. There are two ways to perform this initial run: (1) run with a finite element model in physical coordinates (without mode truncation), or (2) run with a large number of modes taken from the low frequency modes, such as mode 1~30, which was used in current study. Since the modal contributions of various linear vibration modes to the LCO amplitudes will be examined, three representative nondimensional dynamic pressure levels, $\lambda = 1000.0, 1500.0, 2000.0$, are chosen for further study. Caution must be taken while choosing such representatives. It is anticipated that high order modes to be more important at high LCO amplitudes. So, the sample nondimensional dynamic pressures

should not be too low so that the influence of high order modes is underestimated. There are no precise criteria about how high is enough, however, by observing phase plane plot and time history, one can easily tells how good the LCO is. Apparently, λ should not be too high either so that the motion is not LCO any more. It is also possible to use Power Spectrum Density (PSD) plots in helping with the identification of those influential modes so that the sample motions are not restricted to LCOs. As will be explained later, the boundary from LCO to chaos is the focus of further study, so that the LCO is highlighted.

Table 4.2 lists details of the five runs performed to screen out the influential modes dominating the LCO flutter responses of the single layer orthotropic panel under study. The first run was executed with modes #1 ~ #20 ordered in sequence of increasing natural frequency. By inspection of the modal participation factors of these 20 modes, it is easy to tell that mode #2, #4, #8, #9, #11, #13, #15, #19, and #20 have no contribution to the motion and naturally they are eliminated. Then, 9 more modes, mode #21 to #29, are incorporated into the second round. From the results of the 2nd run, mode #22, #24, #25, #26, #28, and #29 are found to be null or little contribution modes and are discarded. It is also noted that due to the appearance of new influential modes, mode #21, #23, and #27, some low order modes survived after the first run relinquished their shares to those newcomers. In consequence, mode #14 becomes unqualified for the next run. The participation factor of mode #17 is also decreased from more than one percent in the first run down to less than one percent. However, mode #17 is also retained for further inspection. Seven new modes, mode #30 to #36, are complemented and the third run is conducted. Frustratingly, none of the newly introduced modes stands out so that even

mode #17 seems safe to stay. The fourth run is carried out with a new set of modes augmented with mode #37 to #43. It is then found out that mode #37 is another important mode. Because of this, the role of mode #17 becomes trivial so that it is excluded together with mode #38, #39, #40, #41, #42 and #43. One more step is taken with mode #44 to #50 added to see if there are more important modes unexposed. The results of the fifth round showed that it is not very constructive. Only one mode of the seven newly introduced modes, mode #49, occupies a percentage of 0.3% for $\lambda = 2000.0$. This implies that further augmentation of modes is not worthy any more. Actually, from the LCO amplitudes calculated during each round, one can also decide whether further run is necessary. It is noted that from the first run to the second run, from the second run to the third run, there are noticeable changes to the LCO amplitudes corresponding to $\lambda = 1000.0$, 1500.0 and 2000.0. And the fifth run does not change LCO amplitudes obtained in the fourth run much that implies convergence is achieved. After all five runs, up to 14 influential modes prove to be candidates for further modal convergence study. If ordered in ascending sequence based on the modal participation percentages (see Table 4.2) for the case of $\lambda = 2000.0$, the 14 modes are:

#3(34.14%), #1(29.79%), #6(15.27%), #12(4.36%), #18(3.77%), #7(3.32%), #10(2.36%), #5(1.88%), #27(1.4%), #16(1.1%), #21(0.84%), #23(0.68%), #37(0.63%), #49(0.33%)

What are these modes? Figure 4.15 shows the mode shapes for above fourteen candidate linear modes. With assistance of these plots, it is easy to tell the number of half sine waves along x- and y-coordinate directions for each mode:

#3(2, 1), #1(1, 1), #6(3, 1), #12(4, 1), #18(5, 1), #7(2, 3), #10(3, 3), #5(1, 3),

#27(6, 1), #16(4, 3), #21(3, 5), #23(5, 3), #37(7, 1), #49(8, 1)

It is noted that the eight modes along x-direction, mode #1(1, 1), #3(2, 1), ..., #49(8, 1), are included in the preliminarily selected 14 candidate modes. This also confirmed the mode convergence study conclusion from Nydick [59] that 8×1 modes are necessary to achieve a converged LCO amplitudes at hypersonic flow speed for an orthotropic, simply supported square panel. A careful investigation of these fourteen modes also indicates: (1) mode #1(1, 1) and #3(2, 1) dominate the LCO since they contribute nearly 65% to the ensemble vibration of the panel, (2) as investigated by Gray and Mei [9], for the same panel, frequency coalescence occurs to mode #1 and mode #2 and coalescence is also expected between mode #3 and mode #4. However, mode #2 and mode #4 do not appear among the candidates. A possible explanation is that influences from mode #2 and mode #4 are "absorbed" by mode #1 and mode #3 due to frequency coalescence phenomena, (3) although the x-direction modes, i.e. mode (n, 1), n = 1, 2, 3,..., are very important (actually the top five dominating modes are such modes), influences from modes other than x-direction modes can not be neglected, for an example, at $\lambda = 2000.0$, mode #7(2, 3) takes up 3.32% modal participation so that it can not be ignored, (4) typically, the role of high frequency modes, such as mode #37(7, 1) and mode #49(8, 1), is less important.

Although the conclusion is somewhat obvious for an orthotropic panel, but the mode selection procedure is really developed for anisotropic composite panels [126]. Further mode convergence study is conducted to examine if there are modes among the fourteen modes that can be neglected to save computation cost. Figure 4.16 shows the mode convergence study results of LCO amplitudes for $\lambda = 500.0 \sim 2000.0$. Here, 6-mode

solution means the top six important modes, i.e., #3(2, 1), #1(1, 1), #6(3, 1), #12(4, 1), #18(5, 1), and mode #7(2, 3), are used for time integration. Similarly, an eight-mode solution employs the top eight important modes, and so on. As expected, the 13-mode solution converged with 14-mode solution that indicates mode #49(8, 1) can be neglected. Attention must be paid when compare this conclusion with that by Nydick [59] since different panel material and geometry are used. The conclusion drawn here serves better as an advice than as a general rule. The 13 modes are selected for further numerical integration experiments.

Besides the mode convergence study, the mesh size is also optimized through a thorough mesh convergence study as illustrated in Fig. 4.17. It is concluded that a 12×8 mesh scheme will give converged LCO amplitudes as a 16×8 mesh. This conclusion agrees with Gray and Mei [9] on mesh size selection when studying LCOs of the same panel. Based upon the investigations undertaken in this section, 12×8 mesh and 13 modes are chosen for future studies on the flutter characteristics of the simply supported square B/Al panel.

4.3.2 Effects of Nonlinear Aerodynamic Terms

The first numerical example is dedicated to investigate the effects of each nonlinear aerodynamic term in the full form piston theory on LCO amplitudes. By expanding the aerodynamic pressure expression given in Eq. (2.2), there are totally seven nonlinear aerodynamic terms, $C_{2x}(\partial w/\partial x)^2$, $C_{2t}C_{2x}(\partial w/\partial x)(\partial w/\partial t)$, $C_{2t}(\partial w/\partial t)^2$, $C_{3x}(\partial w/\partial x)^3$, $C_{3t}C_{3x}(\partial w/\partial x)^2(\partial w/\partial t)$, $C_{3t}C_{3x}(\partial w/\partial x)(\partial w/\partial t)^2$, and $C_{3t}(\partial w/\partial t)^3$, that may affect the panel motion (power of switch variables were removed since they are valued as 1 or 0). Four of

these seven terms, $C_{2x}(\partial w/\partial x)^2$, $C_{2t}(\partial w/\partial t)^2$, $C_{3x}(\partial w/\partial x)^3$, and $C_{3t}(\partial w/\partial t)^3$, possess specific physical meaning since $\partial w/\partial t$ is the panel velocity and $\partial w/\partial x$ is the slope. Therefore, the influences of these four terms on panel LCO are highlighted for a clear physical understanding. The roles of the 6 switch variables are very lucid — switch on/off the influence of corresponding terms. Thus, if the switch variables are ordered as C_{1t}, C_{1x}, C_{2t}, C_{2x}, C_{3t}, C_{3x}, seven specific sets of value patterns can be designed to inspect the role of important terms:

110000	$\partial w/\partial t$ and $\partial w/\partial x$ are functioning — 1st order piston theory
111000	$\partial w/\partial t$, $\partial w/\partial x$, $(\partial w/\partial t)^2$ taking effects
110100	$\partial w/\partial t$, $\partial w/\partial x$, $(\partial w/\partial x)^2$ taking effects
111100	$\partial w/\partial t$, $\partial w/\partial x$, $(\partial w/\partial t)^2$, $(\partial w/\partial x)(\partial w/\partial x)$ and $(\partial w/\partial x)^2$ are involved — 2nd order piston theory
111110	2nd order piston theory with effect of term $(\partial w/\partial t)^3$
111101	2nd order piston theory with effect of term $(\partial w/\partial x)^3$
111111	3rd order piston theory, all 7 nonlinear terms included

Tables 4.3, 4.4, and 4.5 exhibit the effects of neglecting some or all of the abovementioned nonlinear aerodynamic terms on LCO amplitudes of low ($\lambda = 500.0$), moderately high ($\lambda =1000.0$, 1500.0) and high ($\lambda = 2000.0$, 2500.0) nondimensional dynamic pressure values. Panels without thermal loading ($\Delta T_o/\Delta T_{cr} = 0.0$, $T_1 = 0.0$, Table 4.3), with uniform temperature distribution ($\Delta T_o/\Delta T_{cr} = 2.0$, $T_1 = 0.0$, Table 4.4) and with moderate temperature gradient across panel thickness ($\Delta T_o/\Delta T_{cr} = 2.0$, $T_1 = 50.0$, Table 4.5) are considered. Several conclusions can be drawn on basis of a careful review of all

results: (1) at low or moderately high λ, LCO amplitudes obtained using second order piston theory notably differ from those using first order piston theory, however, almost agree with those obtained using third order piston theory, (2) at high λ, LCO amplitudes obtained from first, second and third order theories are all different, (3) at all λ value ranges, term $(\partial w/\partial x)^2$ causes more difference than $(\partial w/\partial t)^2$ and $(\partial w/\partial x)^3$ is more influential than $(\partial w/\partial t)^3$. Conclusion one was also observed by Eastep and McIntosh [56] on studying hypersonic panel flutter of a simply supported two-dimensional isotropic panel and by Gray and Mei [9] while studying LCO of same panel as quoted here at moderately high (the highest λ considered was roughly $80 \times 11.4356 \approx 915$). The overwhelming effect of term $(\partial w/\partial x)^2$ against $(\partial w/\partial t)^2$ is also addressed by these researchers. Second conclusion is believed to be revealed for the first time and is specific to high values of nondimensional dynamic pressure, which is highly possible in the circumstance of hypersonic flow. A physical understanding of the third conclusion is that the slope related nonlinear terms, $(\partial w/\partial x)^2$ and $(\partial w/\partial x)^3$, when considered, will affect the geometry boundary of the flow, hence the pressure distribution, whereas, the velocity related terms, $(\partial w/\partial t)^2$ and $(\partial w/\partial t)^3$, do not have such effects. Observing all three conclusions, it is suggested that the full form 3rd order piston theory must be used in studying flutter response of panels at hypersonic airflow.

4.3.3 Illustrative Motion Map for Orthotropic Panel

It is well accepted that the stability boundaries of a fluttering panel can be established by applying linear aerodynamic theory. Many efforts have been made to depict a stability plot that marks regions of possible panel configurations and motions in supersonic flow,

such as Fig. 3 of Dowell [89], Fig. 5.22–5.24 of Xue [49], and Fig. 1 of Zhou et al. [54]. All such plots are helpful for supersonic vehicle designers because that with information provided in such a map, cares can be taken to avoid the vehicle operates in dangerous parameter regions. However, due to the limitation of linear aerodynamic theory, the bounds of the region for LCO are usually either not well-defined or incomplete. The meaning for demarcating the LCO regions stems from the objective of studying LCO. One crucial concern in panel flutter designs is the fatigue life evaluation (Gray and Mei [9], Xue [49]). Fatigue failure of aircraft skin panel could be caused by LCO or chaotic motion. There exists different fatigue life evaluation algorithms for LCO or chaotic motions and their usage domain is object oriented. Therefore, one must be aware that under certain range of control parameter, what kind of motion the panel is participating so that applicable algorithm is employed.

The major types of motion that may encounter in flutter response analysis of a thermally/mechanically buckled panel have been summarized and illustrated in section 4.2.1. It is the mission of this section to determine and mark the boundaries between various types of motion for the orthotropic panels under study. Figure 4.18 shows a motion map for the simply supported, single layer (i.e., [0]), and double layer (i.e., [0/90]), $12''\times12''\times0.04''$, B/Al panels. The critical buckling temperature ΔT_{cr} for the [0] panel is 2.2186 °F (1.2326 °C). In Fig. 4.18, the boundaries distinguish the flat panel region and the LCO region, and the buckled but dynamically stable region, as well as the upper bound of the buckled panel region are determined by using of a finite element supersonic flutter analysis program used in one of the author's previous work, see reference [127]. The rest of the bounds for LCO region is then obtained by direct

numerical integration using the finite element time domain modal formulation for hypersonic panel flutter analysis developed in present work. For detection of the commencement of chaos, several chaos diagnosis tools introduced in Chapter III have been employed. Observed from Fig. 4.18, the LCO region boundaries for both single layer and double layer panels are highly irregular. This fact reflects the complication of the interplay between the two prevailing instability mechanisms: panel flutter and thermal buckling. A few phenomena can be observed from Fig. 4.18: (1) the single layer panel possesses a larger area of LCO motion than the double layered panel, especially the upper bound of LCO region for single layer panel is much higher than the double layered panel, (2) for the single layer panel, at moderately high nondimensional dynamic pressures, i.e., λ = 500~1300, preliminary bifurcations create a "buffering" region preceding the first observation of chaos boundary, such buffering area also exists for the double layer panel at lower λ values, (3) for the single layer panel, the pure LCO region narrows down quickly at high λ values as λ increases. Compared to the aforementioned stability region plots made by other researchers for isotropic/composite panels at supersonic flow, larger area of the map given in Fig. 4.18 is occupied by chaotic, non-periodic motions. Apparently, more cautions must be borne in mind while designing a vehicle that travels at hypersonic flow.

The boundary of LCO region is not a stability boundary since LCO itself is a nonlinear dynamical instability. The purpose of defining such LCO boundary is not to encourage engineers to design a vehicle with surface panels undergoing LCO. However, at certain extreme situations beyond the flutter boundary, one definitely expects regular

motion like LCO, not the irregular motion like chaos, be on the spot. Therefore, it is worthy to know where the nightmare of chaos starts and how.

The motion map supplies an overview of relationships between system control parameters and motion types. During the process of accumulating points necessary for establishing the boundaries in the map, a large number of time integrations has been carried out and as the byproducts, a huge amount of time histories, phase plane plots, Poincaré maps and bifurcation diagrams have been produced. These auxiliary data are helpful to understanding of the evolution of chaos and post-chaos motions. Figure 4.19 gives one representative bifurcation diagram for $\lambda = 1200$, which falls into the "buffering" region in the motion map. Clearly, the route to chaos for moderately high λ is typically through the pitchfork bifurcation, i.e. period-doubling. Figure 4.20 shows the bifurcation diagram of high dynamic pressure value $\lambda = 3200$. It is seen that at high dynamic pressure, the route to chaos is accompanied with intermittency. These two typical routes to chaos were illustrated with Fig. 4.8 and Fig. 4.12 in section 4.2.

4.3.4 Effects of Aerodynamic Parameters

The typical aircraft takes off, cruises, and lands. The basic aerodynamic parameters keep changing as the flight altitude and vehicle speed changes. A complete aeroelasticity analysis must consider the effects of variations in related aerodynamic parameters.

There are two aerodynamic parameters pertinent to current study subject to changes induced by various flight situations: M_r and C_a, which is the aerodynamic damping coefficient. According to Dowell [7], the typical aerodynamic damping ranges from $C_a = 0.01$ to $C_a = 0.1$. The flow parameter M_r was first used in hypersonic panel flutter

analysis by Eastep and McIntosh [56] and the typical values are $M_r = 0.05, 0.1$ for low and high Mach numbers. The influence of M_r and aerodynamic damping on the LCO region boundary of the single layer panel is then investigated with various combinations of abovementioned typical values. Results are grouped according to equivalent M_r and C_a values and shown in Fig. 4.21 and Fig. 4.22. From results shown in Fig. 4.21, at both low aerodynamic damping, $C_a = 0.01$ and high aerodynamic damping $C_a = 0.1$, increasing M_r will result in decrease of the area for LCO. From Fig. 4.22, it is seen that aerodynamic damping has a more significant effects on LCO region bounds at both low and high M_r values. As a summary of all cases, when $M_r = 0.05$ and $C_a = 0.1$, the area of the pure LCO region is the largest and when $M_r = 0.1$ and $C_a = 0.01$, the LCO region is the smallest of all four cases. This can also be interpreted as that at low Mach number and high aerodynamic damping, LCO region takes up a larger area in the motion map than the other cases. The set of aerodynamic parameters, $M_r = 0.05$, $C_a = 0.1$, are used for all case studies that followed.

4.3.5 Effects of Temperature Gradients

A temperature gradient (T_1) introduces thermal moments that cause bending to the plate. Generally speaking, the bending induced by thermal moments exerts a stiffening effect on the panel, whereas, the thermal expansion due to the elevated average temperature (T_0) plays a softening role. Co-existence of these two opposite actions causes noticeable changes to the stability boundary of a fluttering panel, as discussed in Cheng et al. [127]. It is concluded that temperature gradient benefits the panel motion with lifting up the linear flutter stability boundary and delaying its descending as average

temperature increases. It is the interest of the study carrying on in this section to investigate the influence of temperature gradient on the boundary of the pure LCO region.

The range of temperature gradients, which is typical for aerospace vehicles, is selected with reference to Moorthy [110] and Thornton [113]. Representative low temperature gradient, $T_1 = 20.0$ °F, moderate temperature gradient, $T_1 = 50.0$ °F and high temperature gradient, $T_1 = 100.0$ °F, are considered. The motion maps for the single layer orthotropic panel with above three temperature gradient levels are shown in Fig. 4.23. Figure 4.24 is an overview of temperature gradient effects on the boundary of LCO region through comparisons of various LCO boundaries.

From Fig. 4.23, it is noted that increasing temperature gradient lowers the up-limit of λ, at which chaos appears, and slightly defers the commencement of chaos as average temperature increases. In another word, large temperature gradient makes chaos more possible to occur at high λ. From Fig. 4.24, it is seen that low temperature gradient actually causes little effect on the LCO region since the shape of LCO region boundary for $T_1 = 20.0$ °F resembles that for $T_1 = 0.0$ °F. A tendency of lowering and broadening LCO region boundary as temperature gradient increases can be observed from the comparisons among boundary curves.

4.4 Flutter of Composite Panels

High thermal performance and light weight are among the principal goals for design choices of advanced materials for flight vehicle surface panels. Besides the Metal Matrix Composites (MMC), with B/Al as a special example, polymeric-based composite

materials also have been used extensively in aerospace designs. As a representative of this family of composites, the Graphite/Epoxy laminated composite is among the commonly used material in aerospace engineering. To the aircraft designers, the beauty of fiber-reinforced composites is to allow them tailoring the strength of the structure component in the direction most needed by strategic orientation of the fibers. The variety of fiber orientations, also termed as lamination angles, leads to the varieties in material mechanical/thermal properties. Therefore, dynamical/thermal-mechanical behaviors have long been the major topics of mechanics of composite materials.

To achieve generic conclusions on composite panel dynamics via a thorough study of composites with various fiber and matrix materials, stacking sequences, number of layers is a mission impossible. Thus, present study is focused on panels made of one special type of Graphite/Epoxy composite, the 8-layer, [0/45/-45/90]s, symmetrically laminated composite. Topics general to all composite panel designs, such as effect from the boundary support conditions and the aspect ratio effect, will be addressed in view of the coexistence of thermal loading and aerodynamic pressure applied in hypersonic airflow.

4.4.1 Flutter of a Clamped Square Panel

<u>Mode Filtering, Mode Convergence and Mesh Convergence</u>

The first example panel under study is an all four edges clamped, $12''\times12''\times0.048''$, Graphite/Epoxy 8-layer composite panel. The thermal/mechanical material properties are listed in Table 4.1. In panel flutter analyses of clamped panel using analytical methods, such as Ventres [29] and Kobayashi [31], to satisfy the clamped geometrical boundary conditions, the mode shapes have to be assumed as a combination of functions involving

sin, cos, sinh, cosh. This indicates that the mode shapes for a clamped panel is not exactly in half sine wave shapes as for the simply supported and in sense of finite element analysis, a reasonable scheme of mode selection is required. The mode filtering procedure proposed in section 3.3.1 and illustrated in section 4.2.2 was then applied to the clamped composite panel and results are shown in Table 4.6. Three representative nondimensional dynamic pressure values, $\lambda = 600.0, 800.0, 1000.0$, are selected on basis of an initial run for motion types at various λ values with the lowest 30 modes employed. In convenience of discussion, the mode shapes of related modes are shown in Fig. 4.25.

It is easy to see from Fig. 4.25 that the mode shapes for the clamped panel are more complex than those of simply supported panel (Fig. 4.8). Although there are no precise half sine waves in the mode shapes, for convenience, the mode shapes are still termed as mode (m, n), with m and n denoting the number of half sine wave like curves. As Fig. 4.25 shows, not every mode can be clearly defined as having certain number of half sine wave like curves; hence, "x" is assigned to mode shape curves that are difficult to classify. The first run shown in Table 4.6 indicates that each mode of the lowest 20 modes cited shows its participation to the entire motion, i.e., there is no null contribution as happened in the case of simply supported orthotropic panel (see Table 4.2). However, there are some minor modes with modal participation factors far less than one percent. Elimination proceeds with focus on such modes, with careful inspection of their participation at all three λ values. Six modes, mode #9(0.52%), #11(0.37%), #16(0.41%), #18(0.46%), #19(0.36%), and #20(0.18%), are discarded (all percentages cited from $\lambda = 1000.0$). Note that mode #10 (0.58% at $\lambda = 1000.0$) is retained because it has 1.39% contribution at $\lambda = 600.0$ and this implies mode #10 might be important at low λ values.

It is also noted that during the first run, four x-direction modes, mode #1(1, 1), mode #3(2, 1), mode #8(3, 1), and mode #15(4, 1), have played important roles. In fact, according to the participation percentages for λ = 1000.0, these four modes are the top four contributors. The second run is carried out with six modes, mode 21~26, being added. It is found that mode #24(5,1) is a new discovery that takes up 2.61% contribution at λ = 1000.0. Subsequently, mode #17 that was kept after the first run has given up some shares. The remaining five of the six modes just added did not show any noticeable contributions to the motion so that they are deleted together with mode #17. The third run continued with modes 27~32 introduced into the game and then they are subsequently proved to be trivial modes. Then the fourth run exposed another important x-direction mode, mode #35(6, 1). Mode #34 also shows its contribution to the motion, although that is actually neglectable, mode #34 is retained for further inspection. The fifth run finalizes the whole mode filtering procedure since all four newly added mode are not outstanding and the convergence of LCO amplitudes are reached at all three λ values. As a final result of the mode filtering procedure, 16 modes are selected as candidates for further mode convergence study (ordered according to percentages at λ = 1000.0):

#1(32.68%), **#3(28.48%)**, **#8(11.02%)**, #2(4.47%), **#15(4.2%)**, **#4(2.88%)**, #5(2.58%), #14(2.39%), **#24(2.40%)**, #6(1.84%), #7(1.54%), #12(1.29%), **#35(1.10%)**, #10(1.08%), #34(0.79%), #13(0.72%)

The modes in bold face are the x-direction modes that were expected to be important modes. If nonzero flow angularity is of concern (in real design, definitely yes), as discussed in Cheng et al. [127], it is anticipated that more y-direction modes as well as

hybrid x- and y-direction modes will be important modes and a systematic mode selection strategy like the mode filtering procedure proposed herein is highly demanded.

Figure 4.26 shows the results of mode convergence study for the clamped Gr/Ep panel. Fourteen out of the sixteen candidate modes are chosen for further study. It is noticed that with eight modes, at $\lambda = 1000.0$, a LCO is not reached. This phenomenon is apparently caused by insufficient number of modes, similar abnormalities were also reported by Nydick et al. [59] (see Fig. 8 of their paper) when four or six modes were used for calculation of LCO amplitudes for a simply supported orthotropic panel at high nondimensional dynamic pressures of $\lambda = 2400\text{--}3200$. Increasing the number of modes then overcame this deficiency. Figure 4.27 gives the results for mesh convergence study and it shows a mesh of 12×8 is good enough. Fourteen modes and 12×8 mesh are employed for the rest of studies related to the clamped, $12''\times12''\times0.048''$, $[0/45/-45/90]_s$, Graphite/Epoxy panel.

Motion Map

A substantial quantity of direct time integrations are implemented to plot the motion map for the clamped, square, eight-layer, Gr/Ep panel, the resulting motion map is shown in Fig. 4.28. The motion map shows that the clamped composite panel is apt to chaotic motion at high nondimensional dynamic pressures. The possible explanation is that the highly anisotropic material properties of the composite panel provide more branches of trails for the panel to follow. These branches interweave one another in an irregular pattern that leads to chaos.

It is also observed during the data collection procedure that at low nondimensional dynamic pressures, $\lambda < 800.0$, pre-chaos pitchfork bifurcation is a typical passage to chaotic motions. Whereas, at moderately high and high λ values, the route to chaos usually does not contain obvious pitchfork bifurcation behaviors, as shown in Fig. 4.29. This sudden burst of chaos from period-one LCO brings difficulties in detecting the start point of chaos. As being exploited in previous studies on orthotropic panels, the largest Lyapunov exponent is evaluated through programs provided by Wolf et al. [102]. The newest versions of their Lyapunov exponent evaluation programs are used and minor modifications were made to the interface between Wolf's program and the author's panel flutter analysis codes. Figure 4.30 shows the Lyapunov exponents for the clamped Gr/Ep square panel at $\lambda = 1000.0$ and temperature ratios $\Delta T_0/\Delta T_{cr} = 0.0 \sim 5.0$. Comparison of the Lyapunov exponents shown in Fig. 4.30 and the bifurcation diagram given in Fig. 4.29 leads to a complete understanding of the route to chaos that was taken. At low temperature ratios of $\Delta T_0/\Delta T_{cr} = 0.0 \sim 1.50$, period-one LCO is the major type of motion. Then the chaos starts as temperature ratio increases until $\Delta T_0/\Delta T_{cr} = 1.76$, post-chaos period-two motion appears and lasts for a short range of temperature ratios between $\Delta T_0/\Delta T_{cr} = 1.76$ and $\Delta T_0/\Delta T_{cr} = 1.83$. Another burst of chaos starts at temperature ratio $\Delta T_0/\Delta T_{cr} = 1.84$ and lasts until $\Delta T_0/\Delta T_{cr} = 2.52$, when periodic LCO revives and sustains for a wider range of temperature ratios between 2.52 and 3.08. The panel finally goes into fierce chaotic motions with Lyapunov exponent amplitudes greater than 600, which implies the chaos is matured. Based upon above observations of the interchanges between periodic LCOs and chaotic motions, at $\lambda = 1000.0$, the panel actually takes the intermittent transition route to chaos as defined in section 3.2.2. It is found that at higher

λ values, the intermittency that involves switches of chaos and periodic LCO is not obviously observed. However, in essence, the panel is thought to go through the intermittent transition route since the high dynamic pressure could make bursts of periodic motion occur in a wider range of control parameters so that simulation in a long run may be necessary.

Effects of Insufficient Modes

The detriment of insufficient number of modes to be used for modal truncation was revealed during the mode convergence study. In order to gain a profound understanding of the differences arising from the responses obtained using insufficient number of modes, bifurcation diagrams for the clamped composite panel at a selected nondimensional dynamic pressure, λ = 1600.0, are plotted using six, eight, ten, and fourteen modes and presented in Fig. 4.31. It is seen that using six modes, chaos is predicted to occur beyond the temperature ratio of 2.0. The eight-mode solution denied this conclusion with a prediction of chaos exists even if there is no thermal loading. However, the beautiful shadows of pitchfork bifurcation in the bifurcation diagram obtained using a 10-mode simulation implies the situation may not be that bad. Finally, the 14-mode solution tells that chaos actually commences when the temperature ratio increases over $\Delta T_0/\Delta T_{cr}$ = 0.2. Obviously, the six-mode prediction is too optimistic and the eight-mode, 10-mode predictions are too pessimistic. Careful selection of mode numbers is crucial to obtaining correct predictions of the onset of chaos.

4.4.2 Effect of Boundary Condition — Flutter of a Simply Supported Panel

The influence of boundary supporting conditions on the linear panel flutter boundary and LCO amplitudes have been investigated by several researchers, such as Xue and Mei [50] on supersonic panel flutter boundaries, Gray and Mei [9, 57] on LCO amplitudes at hypersonic flow. The simply supported boundary condition and the clamped boundary condition are two basic support conditions that are encountered in engineering design practices. Generally speaking, the clamped boundary stiffens the panel and simply supported panel possesses more flexibility. To investigate to what extent the boundary supporting condition could affect the LCO region of the composite panels, a simply supported, $12''\times12''\times0.048''$, $[0/45/-45/90]_s$, Graphite/Epoxy panel is taken into consideration.

The analysis is initiated by the routine work of mode filtering procedure, mode convergence and mesh convergence studies. For brevity, the conclusions and results are reviewed. Fourteen candidate modes, mode #1(1,1), #2, #3(2,1) #4 ~ #7, #8(3,1), #9, #11, #12, #14(4, 1), #23(5, 1), and #33(6, 1), were chosen for the mode convergence study and mode #9 is eliminated in consequence. The mesh scheme 12×8 again proved to be reasonably good for discretizing the simply supported Gr/Ep square panel under study. Numerical integrations are then conducted and a motion map is plotted and presented in Fig. 4.32. As observed from the motion map, the linear flutter stability boundary of the simply supported composite panel is much lower than that of the clamped panel, especially at the portion that defines the boundary between "flat" panel and "LCO" region. Compared to the clamped panel, the upper limit of the LCO region for the simply supported panel is lower.

Difference is also showed on the routes to chaos. For simply supported panel, at $\lambda < 1100.0$, typically the route to chaos contains pitchfork bifurcations and at high λ values, intermittent transitions symbolized as bursts of chaos followed by periodic LCO are observed. The bifurcation diagram and Lyapunov exponents of simply supported composite panel are shown in Fig. 4.33 and Fig. 4.34 for comparison with those for the clamped panel (Fig. 4.29 and 4.30). The bifurcation diagram and the Lyapunov exponents announce that at temperature ratio of $\Delta T_o/\Delta T_{cr} = 3.20$, the chaos starts. However, the discontinuities of the bifurcation diagram and the tortuous shape in Fig. 4.30 after the first observation of chaos imply that quasi-periodicity may exist (Moon [79]). Compared to the clamped square panel, within the same range of temperature ratios, the Lyapunov exponents after chaos are at a lower level, with the highest value less than 400.0, which indicates that chaos is less severe for the simply supported panel in this range of temperatures.

As an interim summary of the evolution of chaos that have been observed so far, two "classical" routes to chaos are typical to a fluttering panel at supersonic/hypersonic flow: the period-doubling (pitchfork bifurcations) route and the intermittency (sudden bursts of chaos followed by periodic LCOs) route. They are mathematically described well (phase plane portraits, the Poincaré map, bifurcation diagram), however, physically mysterious. There is one general, but not final, explanation to the complicated behaviors arisen along various routes to chaos as quoted by Bolotin et al. [97] and Hilborn [82]: it is the coexistence of several attractors (LCO, chaos, etc.) in a dynamic system within a given range of control parameter values that gives rise to the complex transitions of system behavior since the characters of the attractors are changing as control parameter

varies. It is typically observed in present hypersonic panel flutter study that route involving pitchfork bifurcations takes place when the dynamic pressure is low or moderately high and intermittency is more or less related to high dynamic pressures. Thus, in engineering sense, the pitchfork bifurcation route is mild and the intermittency way is violent. Like Moon [79] said, "The period-doubling model for the route to chaos is an elegant, aesthetic model and has been described in many popular articles." This elegant pitchfork bifurcation route seems to be a potential good wish of the hypersonic flight vehicle designers since sudden burst of chaos without precursor is more difficult to predict and prevent. As illustrated herein, loosening the stiff supports is among feasible design options.

4.4.3 Effect of Aspect Ratio — Flutter of a Rectangular Panel

Besides the square panels, rectangular panels of various length to width ratios also have extensive applications in aircraft surface panel designs. To complete the comparisons of the effects on stability boundaries and LCO region boundary from design parameters, the flutter responses of a clamped, rectangular panel with aspect ratio of 1.25 are analyzed. The x-coordinate, or the flow parallel direction, is selected to be along the longer edge of the panel so that the weaker case between the two options is investigated.

Mode filtering procedure for the rectangular panel shows that 16 modes, including #1(1, 1), #2, #3(2, 1), #4, #5, #6(3, 1), #7, #10, #12(4, 1), #13, #15 ~ #19(5, 1), #27(6,1), are possible important modes. Mode #13 and #16 are neglected on basis of results of the mode convergence study and a 12×8 mesh is shown to be reasonably fine to the rectangular case. The motion map is then obtained through numerical integrations and the

resulting map is shown as Fig. 4.35. From Fig. 4.35, it is seen that compared to the clamped square panel, the linear flutter stability boundary of the rectangular panel experiences slight effect (without thermal loading, the critical dynamic pressure for the rectangular panel is λ_{cr} = 569.0 and λ_{cr} for the clamped panel without thermal effect is 523.0). However, the LCO region for the rectangular panel is quite limited. The chaos shows up at moderately high dynamic pressures and a temperature ratio greater than 3.0 could result in chaotic motion at low or high dynamic pressures. It is very clear that increasing flow direction flexibility will make the panel more possible to step into chaos.

4.4.4 Summary of Different Designs

For non-dimensionalization purposes, the thermal loading is expressed in temperature ratios with the critical thermal buckling temperature, ΔT_{cr}, as references. However, ΔT_{cr} is highly related to the panel material properties, geometry and supporting conditions. Therefore, an accurate comparison of above panel designs must be based upon the absolute temperature. The critical thermal buckling temperatures for the clamped square panel, simply supported square panel and clamped rectangular panel are listed in Table 4.7. The clamped square panel has the highest ΔT_{cr} and the simply supported square panel has the lowest ΔT_{cr}.

With the thermal buckling temperatures given in Table 4.7, the motion maps of the three designs can be compared in a uniform coordinate system after a simple coordinate transformation, as shown in Fig. 4.36. Remarks on the three designs can be made through several aspects:

1) If the thermal performance is the only concern, i.e., aerodynamic loading is neglectable, the clamped square panel is the best choice because of its high ΔT_{cr}.

2) If linear flutter stability boundary with thermal effects is the primary concern, the clamped rectangular panel is the best as it owns the biggest stable region in the motion map.

3) If thermal effects, linear stability boundary and the area of LCO region are considered together, the clamped square panel is relatively better than the other two designs since it has a larger area of LCO region and the linear stability boundary is moderately high.

Of all three designs, none is able to immunize from chaotic motion when the temperature increase is higher than 180 °F, even if the dynamic pressure is low. This implies all three designs are not suitable to advanced supersonic/hypersonic aircraft because that for the supersonic aircraft, the temperature at the surface panel could be as high as 350 °F, and for the hypersonic aircraft, a temperature range of 1800 °F ~ 3000 °F is possible. Obviously, new material and/or innovative structural designs [128, 129] are in demand. Whatever the material is used and no matter what type of elaborate designs are proposed, the finite element time domain modal formulation presented herein can be applied as a general purpose design assistance tool for evaluation and optimization of the design options with low cost, which is the original goal of this study.

Table 4.1 Material properties, geometry, and boundary conditions of panels under study

Items	1	2	3	4	5	6
Material	Aluminum	B/Al*	B/Al	Gr/Ep	Gr/Ep	Gr/Ep
Geometry	12×12×0.05	12×12×0.04	12×12×0.04	12×12×0.048	12×12×0.048	15×12×0.048
Lamination	[0]	[0]	[0/90]	[0/45/-45/90]$_s$	[0/45/-45/90]$_s$	[0/45/-45/90]$_s$
Support	Simply Supported	Simply Supported	Simply Supported	Clamped	Simply Supported	Clamped
E_{11},Msi	10.0	31.0	31.0	22.5	22.5	22.5
E_{22}, Msi	10.0	20.0	20.0	1.17	1.17	1.17
G_{12}, Msi	3.84	8.40	8.40	0.66	0.66	0.66
ν_{12}	0.3	0.27	0.27	0.22	0.22	0.22
Density, lb-sec^2/in.^{4}	2.6×10^{-4}	2.46×10^{-4}	2.46×10^{-4}	1.458×10^{-4}	1.458×10^{-4}	1.458×10^{-4}
α_1[†]	1.25×10^{-5}	3.22×10^{-6}	3.22×10^{-6}	-0.04×10^{-6}	-0.04×10^{-6}	-0.04×10^{-6}
α_2[†]	1.25×10^{-5}	1.06×10^{-5}	1.06×10^{-5}	1.67×10^{-5}	1.67×10^{-5}	1.67×10^{-5}

* Boron /Aluminum

Graphite/Epoxy

[†] Thermal expansion coefficients along material principal directions

113

Table 4.2 Mode filtering procedure for simply supported, [0], B/Al square panel

1st run

λ	1*	2√	3	4	5	6	7	8	9	10	11	12	13	14	15	16	17	18	19	20	W_{max}/h
1000	35.54	0.0	34.23	0.0	2.03	13.06	3.01	0.0	0.0	1.72	0.0	6.69	0.0	0.25	0.0	0.72	0.54	2.18	0.0	0.0	1.3641
1500	32.19	0.0	35.02	0.0	1.75	15.17	2.91	0.0	0.0	2.25	0.0	5.06	0.0	0.56	0.0	1.91	1.03	2.15	0.0	0.0	1.7791
2000	26.45	0.0	32.28	0.0	1.68	15.03	4.09	0.0	0.0	3.41	0.0	6.25	0.0	0.68	0.0	1.93	1.16	7.05	0.0	0.0	2.0704

2nd run

λ	1	3	5	6	7	10	12	14	16	17	18	21	22	23	24	25	26	27	28	29	W_{max}/h
1000	35.34	33.73	2.05	12.66	2.97	1.72	6.57	0.21	0.70	0.43	2.04	0.23	0.0	0.57	0.0	0.14	0.0	0.63	0.0	0.0	1.3855
1500	32.70	34.92	1.79	14.67	2.75	1.95	4.97	0.29	1.40	0.65	1.64	0.42	0.0	0.62	0.0	0.25	0.0	0.97	0.0	0.0	1.8258
2000	30.07	34.23	1.79	15.22	3.26	2.30	4.39	0.32	1.18	0.54	3.75	0.60	0.0	0.64	0.0	0.35	0.0	1.54	0.0	0.0	2.0942

3rd run

λ	1	3	5	6	7	10	12	16	17	18	21	23	27	30	31	32	33	34	35	36	W_{max}/h
1000	35.33	33.73	2.04	12.66	2.97	1.70	6.57	0.70	0.44	2.04	0.28	0.51	0.63	0.01	0.25	0.11	0.0	0.01	0.0	0.02	1.3876
1500	32.74	34.96	1.76	14.68	2.75	1.92	4.97	1.39	0.64	1.65	0.51	0.54	0.95	0.02	0.26	0.19	0.0	0.04	0.0	0.04	1.8283
2000	30.07	34.23	1.70	15.21	3.23	2.23	4.39	1.16	0.54	3.55	0.70	0.52	1.56	0.03	0.40	0.37	0.0	0.05	0.0	0.07	2.0893

4th run

λ	1	3	5	6	7	10	12	16	17	18	21	23	27	37	38	39	40	41	42	43	W_{max}/h
1000	35.25	33.77	2.03	12.73	2.93	1.71	6.53	0.70	0.45	2.03	0.28	0.56	0.60	0.29	0.0	0.0	0.04	0.01	0.10	0.0	1.3779
1500	32.59	34.93	1.80	14.74	2.74	1.93	4.94	1.32	0.66	1.62	0.51	0.60	0.93	0.41	0.0	0.0	0.10	0.04	0.16	0.0	1.8249
2000	29.41	33.82	1.87	15.17	3.33	2.43	4.30	1.09	0.55	3.98	0.70	0.71	1.46	0.73	0.0	0.0	0.17	0.05	0.23	0.0	2.0586

5th run

| λ	1	3	5	6	7	10	12	16	18	21	23	27	37	44	45	46	47	48	49	50	W_{max}/h
1000	35.45	33.92	2.03	12.75	2.94	1.70	6.54	0.72	2.03	0.27	0.56	0.60	0.28	0.0	0.0	0.0	0.01	0.0	0.17	0.02	1.3815
1500	32.86	35.19	1.83	14.81	2.75	1.91	4.96	1.32	1.62	0.56	0.60	0.93	0.38	0.0	0.0	0.0	0.03	0.0	0.19	0.06	1.8158
2000	29.79	34.14	1.88	15.27	3.32	2.36	4.36	1.10	3.77	0.84	0.68	1.40	0.63	0.0	0.0	0.0	0.03	0.0	0.33	0.09	2.0602

*Mode number in bold face indicates influential mode that is kept for next run

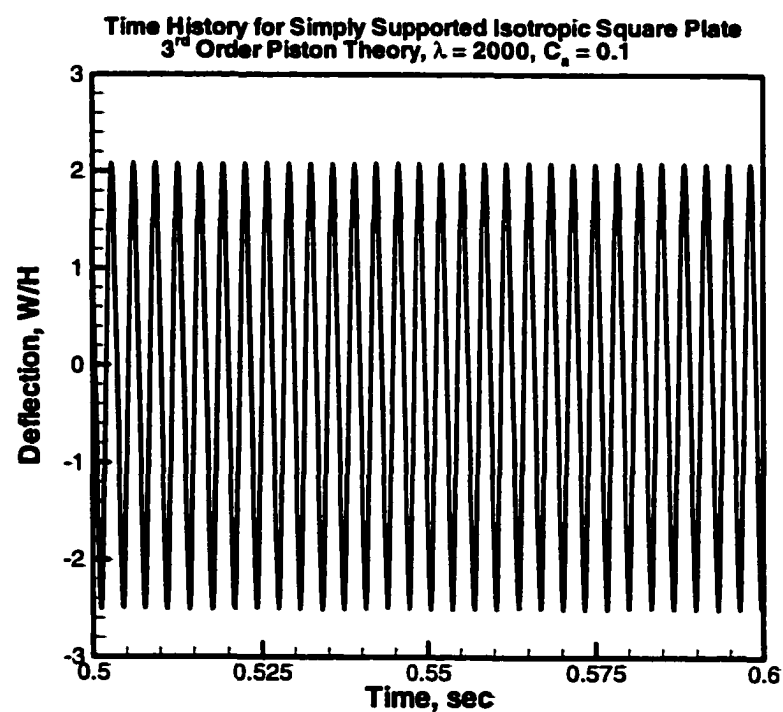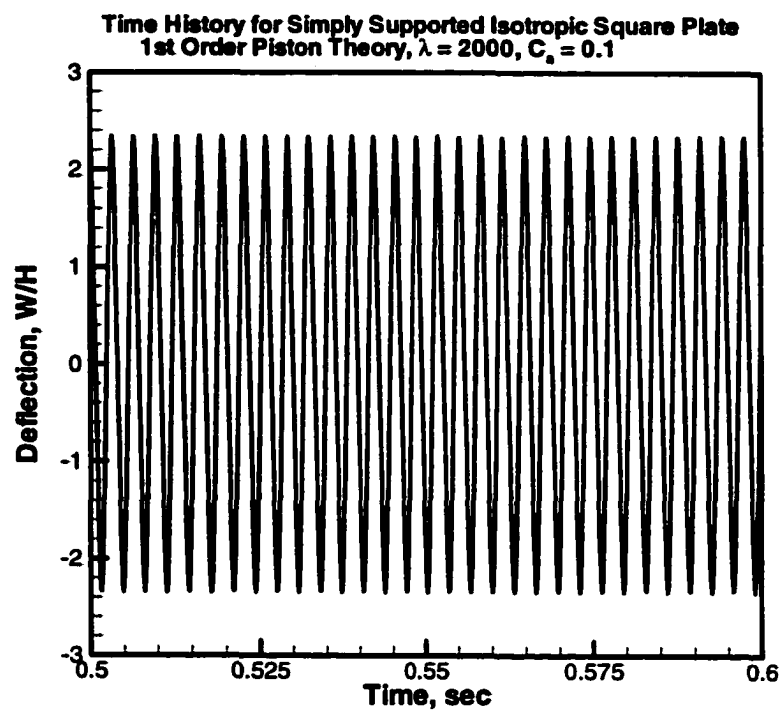√Mode number underlined indicates trivial mode that is filtered out

'All modal participation factors are expressed in percentage %

114

Table 4.3 Effects on limit cycle amplitude by neglecting higher order terms in aerodynamic piston theory for single layer B/Al panel without thermal loading

Case	C_{1t}	C_{1x}	C_{2t}	C_{2x}	C_{3t}	C_{3x}	Dynamic Pressure, λ				
							500	1000	1500	2000	2500
1	1	1	0	0	0	0	0.2837	1.3293	1.7267	2.0025	2.2665
2	1	1	1	0	0	0	0.2837	1.3293	1.7267	2.0025	2.2665
3	1	1	0	1	0	0	0.2863	1.3752	1.8004	2.0312	2.4259
4	1	1	1	1	0	0	0.2862	1.3704	1.8043	2.0279	2.4259
5	1	1	1	1	1	0	0.2862	1.3704	1.8042	2.0279	2.4259
6	1	1	1	1	0	1	0.2863	1.3721	1.8046	2.0162	2.2763
7	1	1	1	1	1	1	0.2863	1.3723	1.8046	2.0162	2.2726

Table 4.4 Effects on limit cycle amplitude by neglecting higher order terms in aerodynamic piston theory for single layer B/Al panel with uniform temperature distribution ($\Delta T_o/\Delta T_{cr} = 2.0$)

Case	C_{1t}	C_{1x}	C_{2t}	C_{2x}	C_{3t}	C_{3x}	Dynamic Pressure, λ				
							500	1000	1500	2000	2500
1	1	1	0	0	0	0	1.0453	1.6218	1.9529	2.2010	2.3865
2	1	1	1	0	0	0	1.0453	1.6218	1.9529	2.2010	2.3865
3	1	1	0	1	0	0	1.0866	1.6787	2.0767	2.2093	2.6430
4	1	1	1	1	0	0	1.0849	1.6591	2.0487	2.2063	2.4645
5	1	1	1	1	1	0	1.0849	1.6591	2.0487	2.2063	2.4645
6	1	1	1	1	0	1	1.0838	1.6585	2.0633	2.2054	2.4733
7	1	1	1	1	1	1	1.0838	1.6587	2.0637	2.2008	2.4730

Table 4.5 Effects on limit cycle amplitude by neglecting higher order terms in aerodynamic piston theory for single layer B/Al panel with moderate temperature gradient across thickness ($\Delta T_o/\Delta T_{cr} = 2.0$, $T_1 = 50.0\ ^\circ F$)

Case	C_{1t}	C_{1x}	C_{2t}	C_{2x}	C_{3t}	C_{3x}	Dynamic Pressure, λ				
							1000	1200	1500	1800	2000
1	1	1	0	0	0	0	1.3100	1.3306	1.5853	1.7710	1.8414
2	1	1	1	0	0	0	1.3100	1.3306	1.5853	1.7710	1.8414
3	1	1	0	1	0	0	1.3191	1.4986	1.7327	1.8721	1.9511
4	1	1	1	1	0	0	1.2960	1.4881	1.7279	1.8707	1.9485
5	1	1	1	1	1	0	1.2960	1.4881	1.7279	1.8707	1.9485
6	1	1	1	1	0	1	1.3032	1.4931	1.7262	1.8713	1.9472
7	1	1	1	1	1	1	1.3031	1.4925	1.7268	1.8714	1.9474

Table 4.6 Mode filtering procedure for clamped, [0/45/-45/90]$_s$, Gr/Ep square panel

1st run

λ	1*	2	3	4	5	6	7	8	9	10	11√	12	13	14	15	16	17	18	19	20	Wmax/h
600	34.18	9.92	29.24	2.65	5.83	0.94	0.64	8.79	0.44	1.39	0.19	0.42	0.55	1.38	2.49	0.53	0.13	0.12	0.11	0.05	0.8460
800	35.04	5.09	30.11	2.81	2.99	1.66	1.42	10.58	0.51	0.80	0.25	0.80	0.75	2.11	3.73	0.57	0.38	0.15	0.20	0.07	1.6899
1000	34.30	3.67	29.19	2.80	2.16	1.92	15.7	10.97	0.52	0.58	0.37	1.20	0.95	2.69	4.73	0.41	0.97	0.46	0.36	0.18	2.2657

2nd run

λ	1	2	3	4	5	6	7	8	10	12	13	14	15	17	21	22	23	24	25	26	Wmax/h
600	33.56	10.79	28.62	2.83	6.24	0.85	0.71	8.64	1.71	0.35	0.58	1.27	2.21	0.13	0.11	0.03	0.03	1.12	0.08	0.15	0.7736
800	33.50	6.39	29.01	2.81	3.71	1.54	1.26	10.45	1.24	0.80	0.69	1.82	3.77	0.40	0.27	0.09	0.05	1.91	0.10	0.20	1.5388
1000	32.24	4.78	28.38	2.90	2.86	1.83	1.54	11.19	1.23	1.25	0.76	2.32	4.23	0.89	0.34	0.20	0.11	2.61	0.10	0.24	1.9971

3rd run

λ	1	2	3	4	5	6	7	8	10	12	13	14	15	24	27	28	29	30	31	32	Wmax/h
600	33.67	10.77	28.75	2.82	6.28	0.85	0.70	8.69	1.71	0.35	0.60	1.29	2.21	1.12	0.03	0.06	0.01	0.03	0.02	0.03	0.7736
800	33.82	6.26	29.34	2.80	3.67	1.56	1.25	10.58	1.22	0.81	0.67	1.98	3.75	1.93	0.03	0.07	0.08	0.07	0.05	0.08	1.5509
1000	32.78	4.71	28.92	2.90	2.76	1.87	1.52	11.41	1.18	1.27	0.75	2.42	4.28	2.65	0.08	0.12	0.09	0.09	0.08	0.11	1.9972

4th run

λ	1	2	3	4	5	6	7	8	10	12	13	14	15	24	33	34	35	36	37	38	Wmax/h
600	33.55	10.59	28.60	2.79	6.15	0.85	0.71	8.67	1.66	0.36	0.61	1.28	2.20	1.07	0.03	0.30	0.44	0.03	0.09	0.04	0.7850
800	33.67	6.00	29.15	2.78	3.46	1.55	1.27	10.49	1.16	0.79	0.68	1.95	3.63	1.75	0.05	0.59	0.83	0.03	0.13	0.04	1.5807
1000	32.76	4.45	28.59	2.85	2.56	1.84	1.52	11.07	1.06	1.28	0.76	2.40	4.21	2.41	0.07	0.81	1.09	0.05	0.15	0.06	2.0644

5th run

λ	1	2	3	4	5	6	7	8	10	12	13	14	15	24	34	35	39	40	41	42	Wmax/h
600	33.58	10.62	28.61	2.79	6.16	0.85	0.71	8.67	1.68	0.35	0.61	1.28	2.20	1.07	0.30	0.44	0.03	0.01	0.01	0.02	0.7850
800	33.63	6.05	29.09	2.79	3.49	1.56	1.28	10.46	1.17	0.79	0.69	1.94	3.64	1.75	0.58	0.83	0.08	0.05	0.04	0.09	1.5790
1000	32.68	4.47	28.48	2.88	2.58	1.84	1.54	11.02	1.08	1.29	0.78	2.39	4.20	2.40	0.79	1.10	0.12	0.10	0.06	0.20	2.0635

*Mode number in bold face indicates influential mode that is kept for next run

√Mode number underlined indicates trivial mode that is filtered out

'All modal participation factors are expressed in percentage %

Table 4.7 Critical thermal buckling temperatures for

[0/45/-45/90]ₛ, Graphite/Epoxy panels

Panel Description	Critical Thermal Buckling Temperature ΔTcr (°F)
Clamped, 12" ×12" ×0.048"	54.55
Simply Supported, 12" ×12" ×0.048"	19.71
Clamped, 15" ×12" ×0.048"	36.48
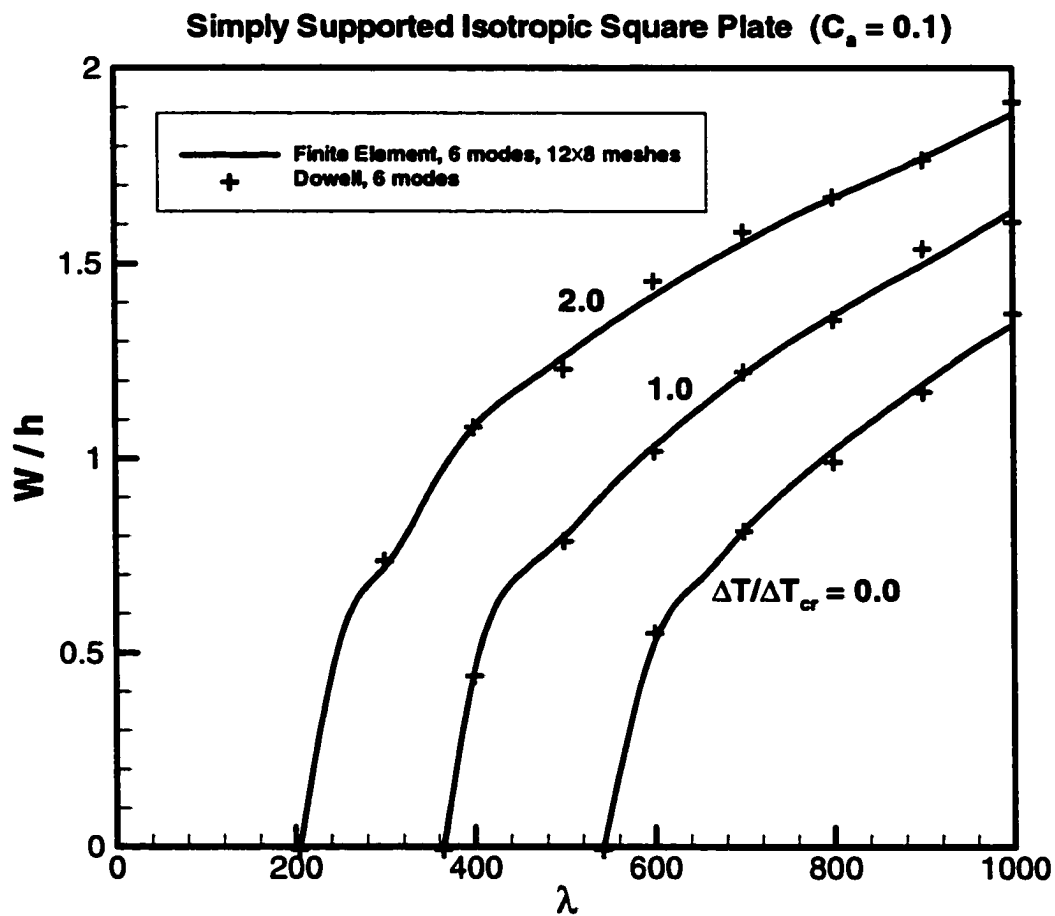
Fig. 4.1 Comparison of dynamic pressure and LCO amplitudes for a simply supported isotropic square panel.

Time History for Simply Supported Isotropic Square Plate
1st Order Piston Theory, $\lambda = 2000$, $C_a = 0.1$

(a)

Time History for Simply Supported Isotropic Square Plate
3rd Order Piston Theory, $\lambda = 2000$, $C_a = 0.1$

(b)

Fig. 4.2 Observation bias of motion into the cavity when nonlinear aerodynamic theory is employed
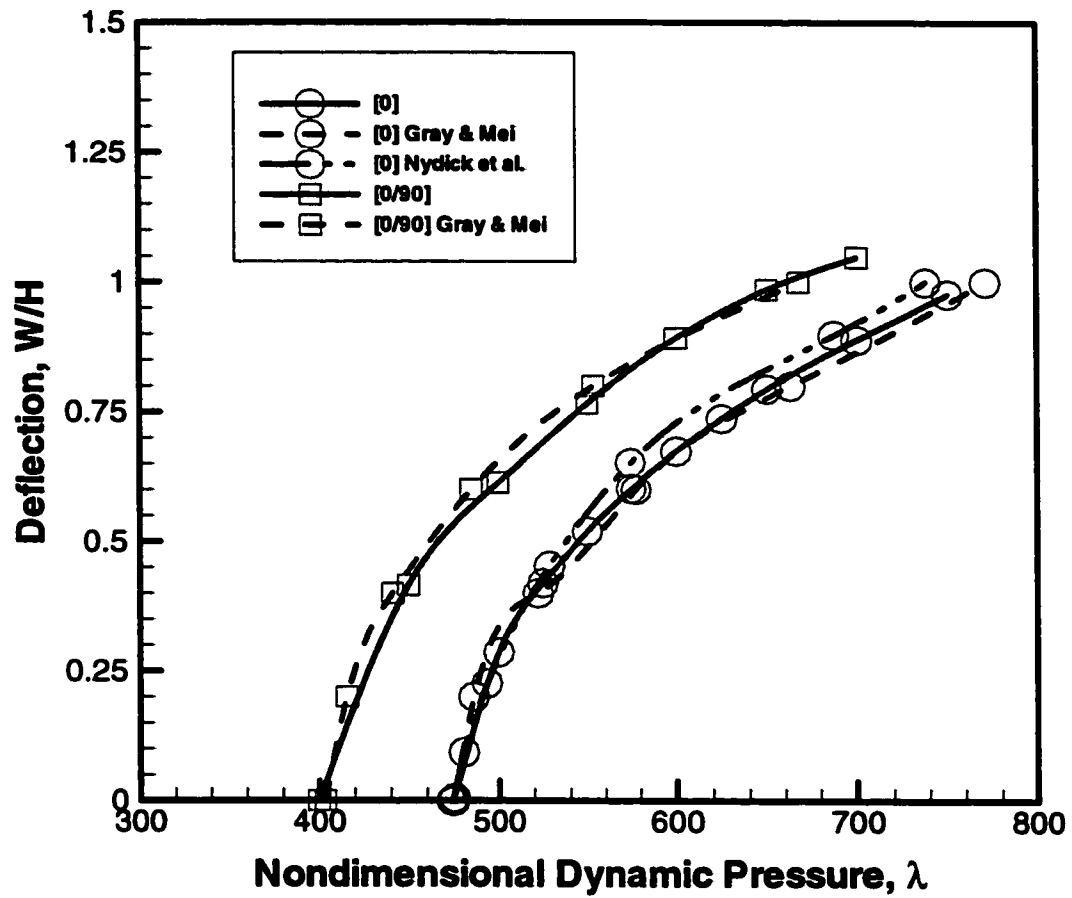
Fig. 4.3 Comparison of LCO amplitudes of simply supported B/Al square panels at hypersonic airflow
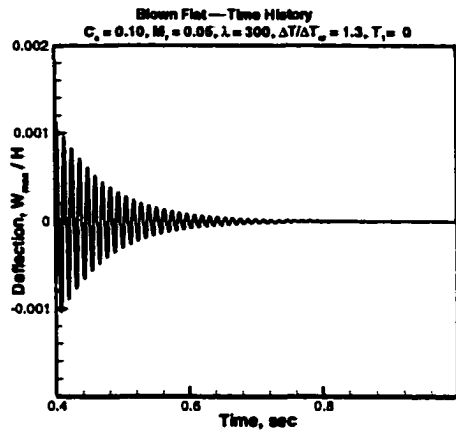
(a) Time history
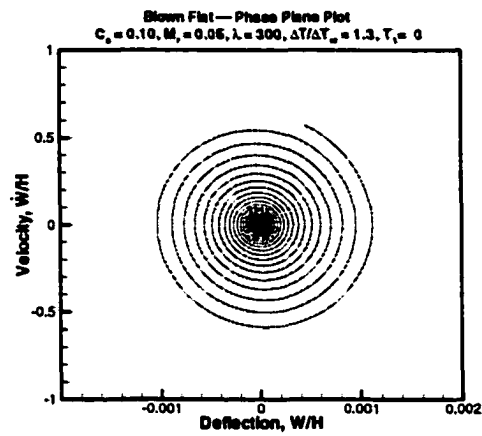
(b) Phase plane plot
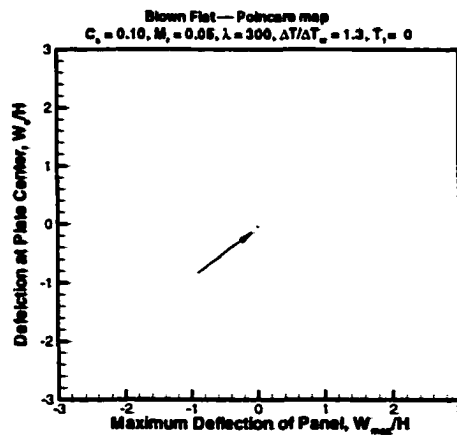
(c) Poincaré map

Fig. 4.4 The blown flat isotropic panel as a demonstration of flat and stable panel condition
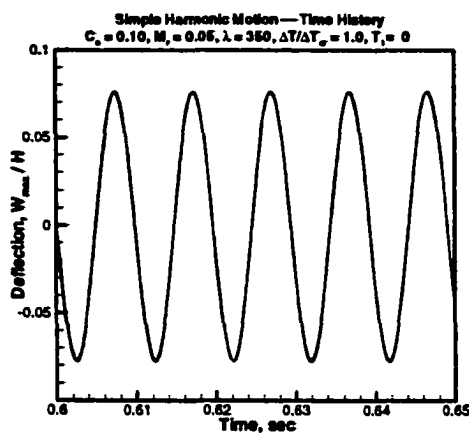
(a) Time history
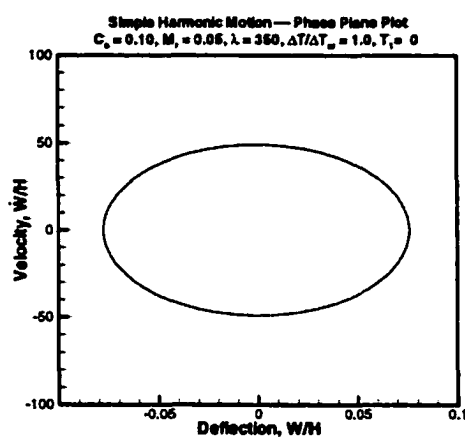
(b) Phase plane plot
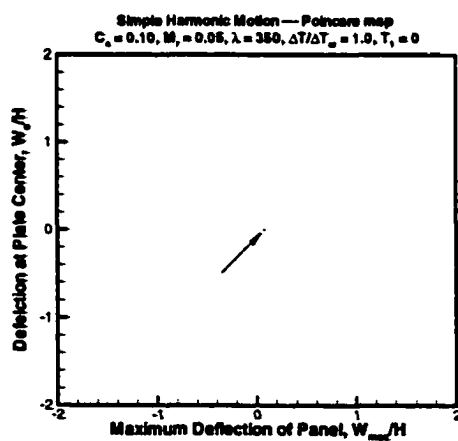
(c) Poincaré map

Fig. 4.5 Demonstration of simple harmonic LCO of isotropic panel

Period-2 Motion — Time History
$C_a = 0.10$, $M_* = 0.05$, $\lambda = 1200$, $\Delta T/\Delta T_* = 3.5$, $T_* = 0$

(a) Time history

Period-2 Motion — Phase Plane Plot
$C_a = 0.10$, $M_* = 0.05$, $\lambda = 1200$, $\Delta T/\Delta T_* = 3.5$, $T_* = 0$

(b) Phase plane plot
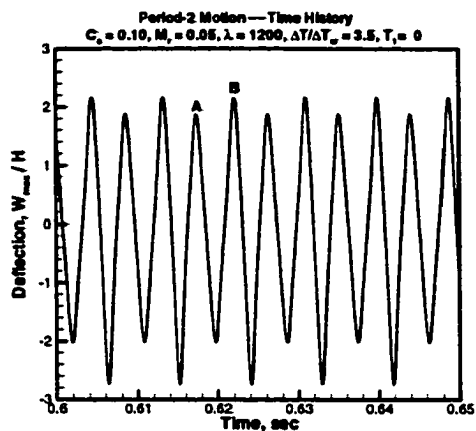
Period-2 Motion — Poincare map
$C_a = 0.10$, $M_* = 0.05$, $\lambda = 1200$, $\Delta T/\Delta T_* = 3.5$, $T_* = 0$
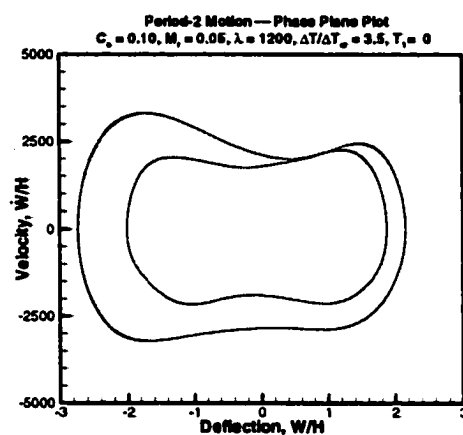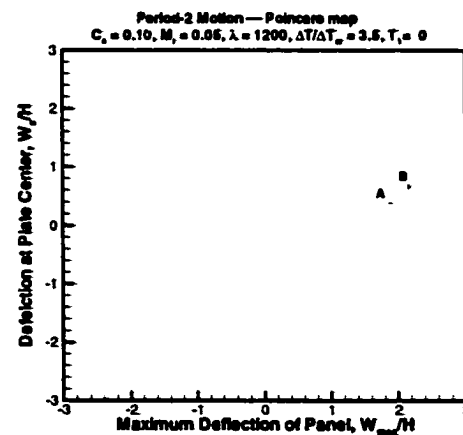
(c) Poincaré map

Fig. 4.6 Demonstration of periodic motion of isotropic panel

Chaotic Motion — Time History
$C_a = 0.10$, $M_a = 0.05$, $\lambda = 2500$, $\Delta T/\Delta T_a = 7.2$, $T_i = 0$

(a) Time history

Chaotic Motion — Phase Plane Plot
$C_a = 0.10$, $M_a = 0.05$, $\lambda = 2500$, $\Delta T/\Delta T_a = 7.2$, $T_i = 0$

(b) Phase plane plot

Chaotic Motion — Poincaré map
$C_a = 0.10$, $M_a = 0.05$, $\lambda = 2500$, $\Delta T/\Delta T_a = 7.2$, $T_i = 0$
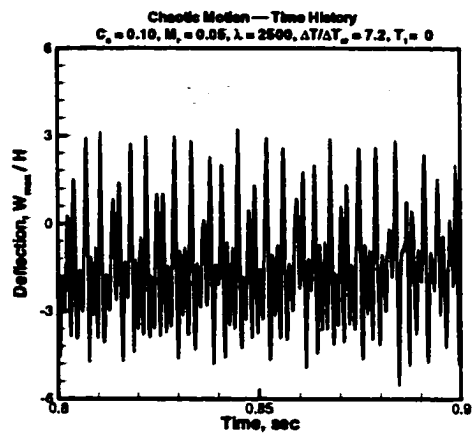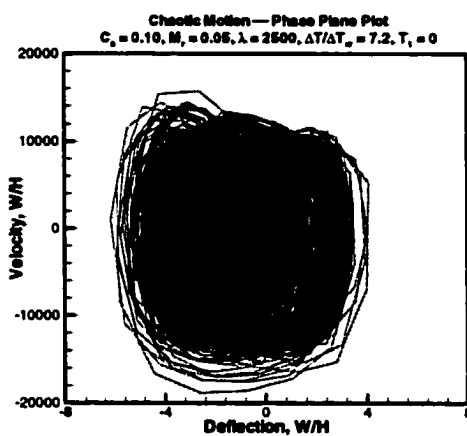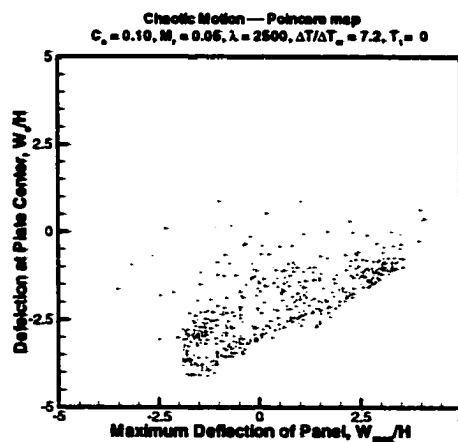
(c) Poincaré map

Fig. 4.7 Demonstration of chaotic motion of isotropic panel

Bifurcation Diagram
$C_a = 0.10$, $M_r = 0.05$, $\lambda = 1100$, $T_1 = 0$
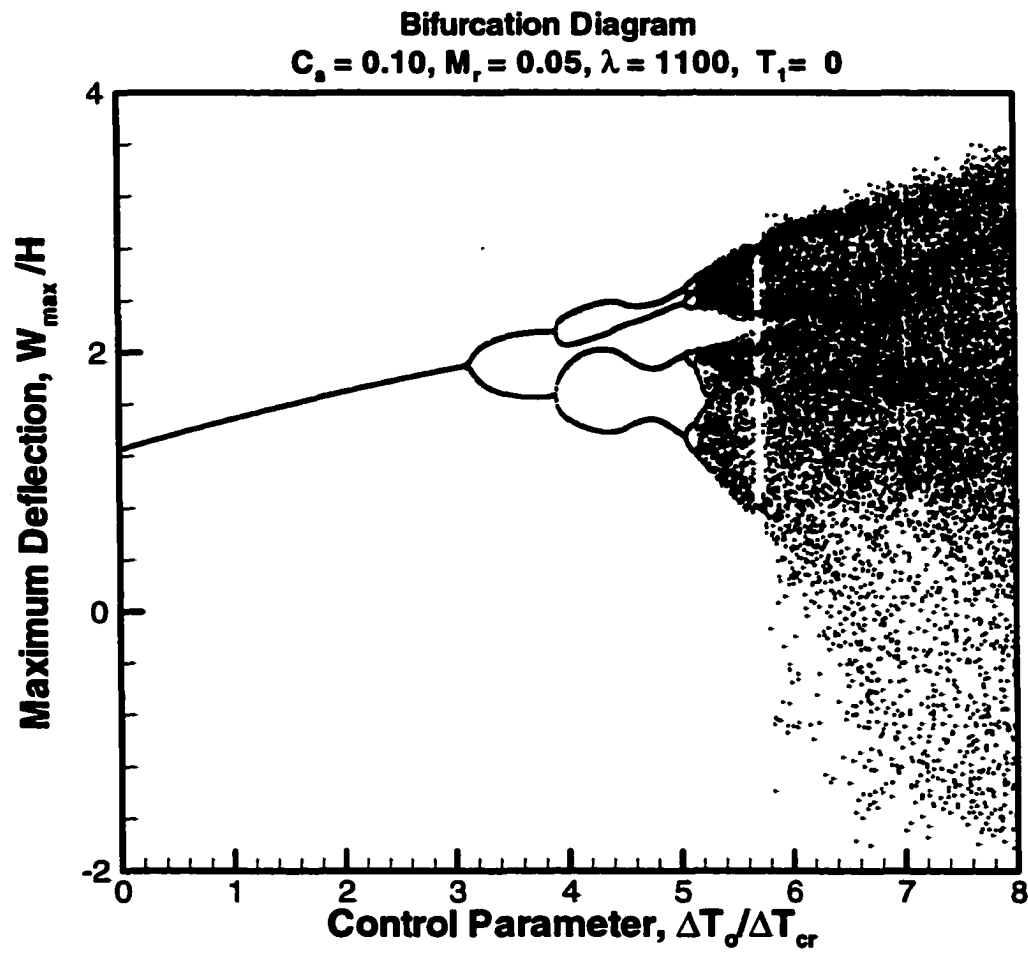
Fig. 4.8 Bifurcation diagram for a simply supported, $12'' \times 12'' \times 0.05''$ aluminum panel at $\lambda = 1100.0$
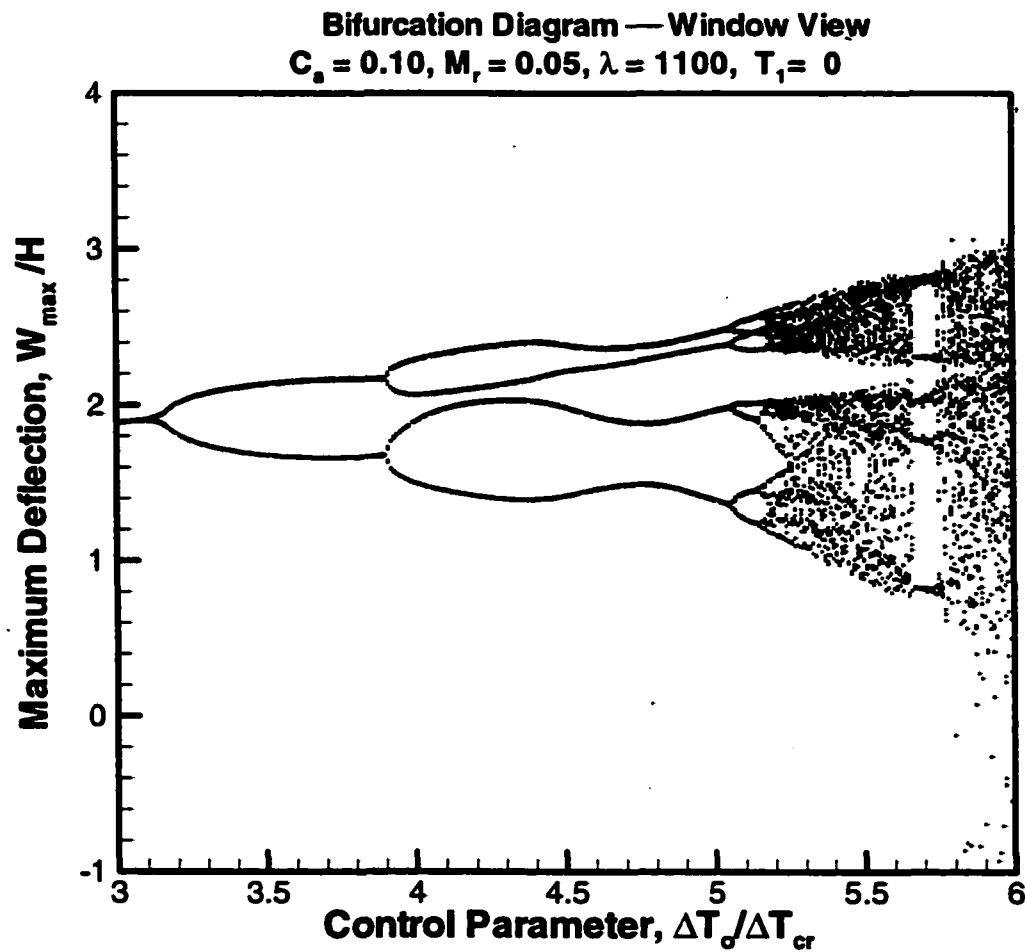
Fig. 4.9 Observation of pitchfork bifurcation and period doubling route to chaos for a simply supported, 12"× 12"× 0.05"aluminum panel at λ = 1100.0

(a) $\Delta T_o / \Delta T_{cr} = 3.0$

(b) $\Delta T_o / \Delta T_{cr} = 3.5$

(c) $\Delta T_o / \Delta T_{cr} = 4.5$

(d) $\Delta T_o / \Delta T_{cr} = 5.1$

(e) $\Delta T_o / \Delta T_{cr} = 5.4$

(f) $\Delta T_o / \Delta T_{cr} = 5.7$
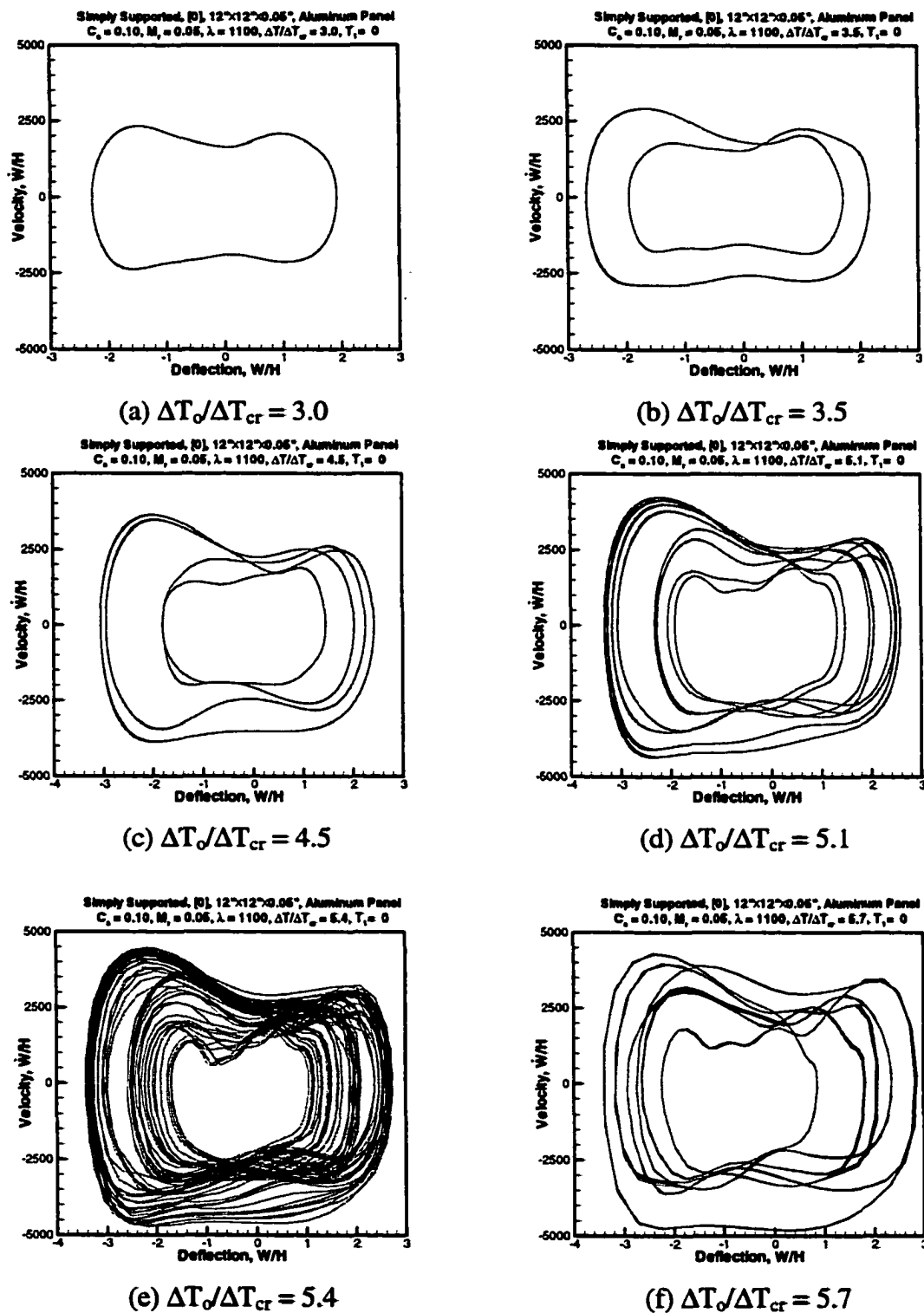
Fig. 4.10 Observation and evolution of chaos in phase plane for a simply supported, $12'' \times 12'' \times 0.05''$ aluminum panel at $\lambda = 1100.0$
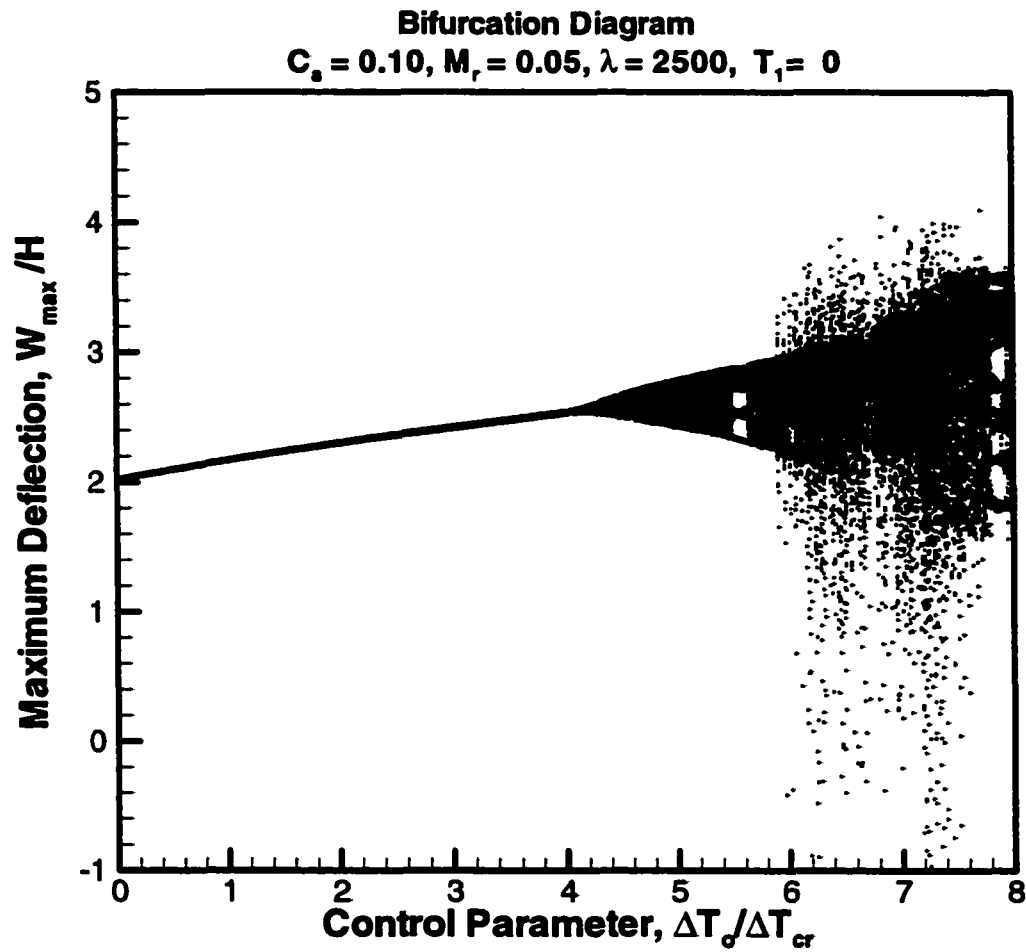
**Fig. 4.12 Bifurcation diagram for a simply supported,
12″× 12″× 0.05″ aluminum panel at λ = 2500.0**
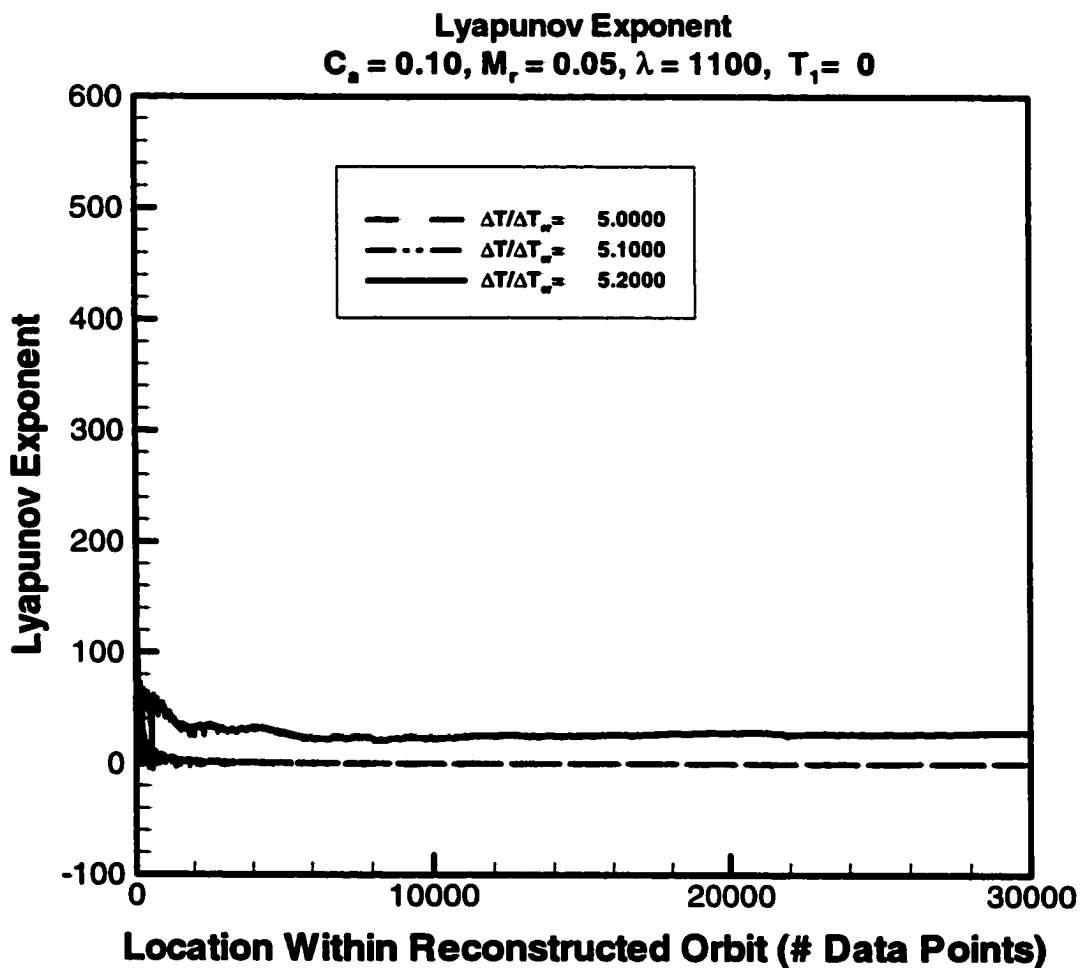
Fig. 4.13 Lyapunov components at the vicinity of first chaos observation for a simply supported, 12″× 12″× 0.05″ aluminum panel at λ = 1100.0
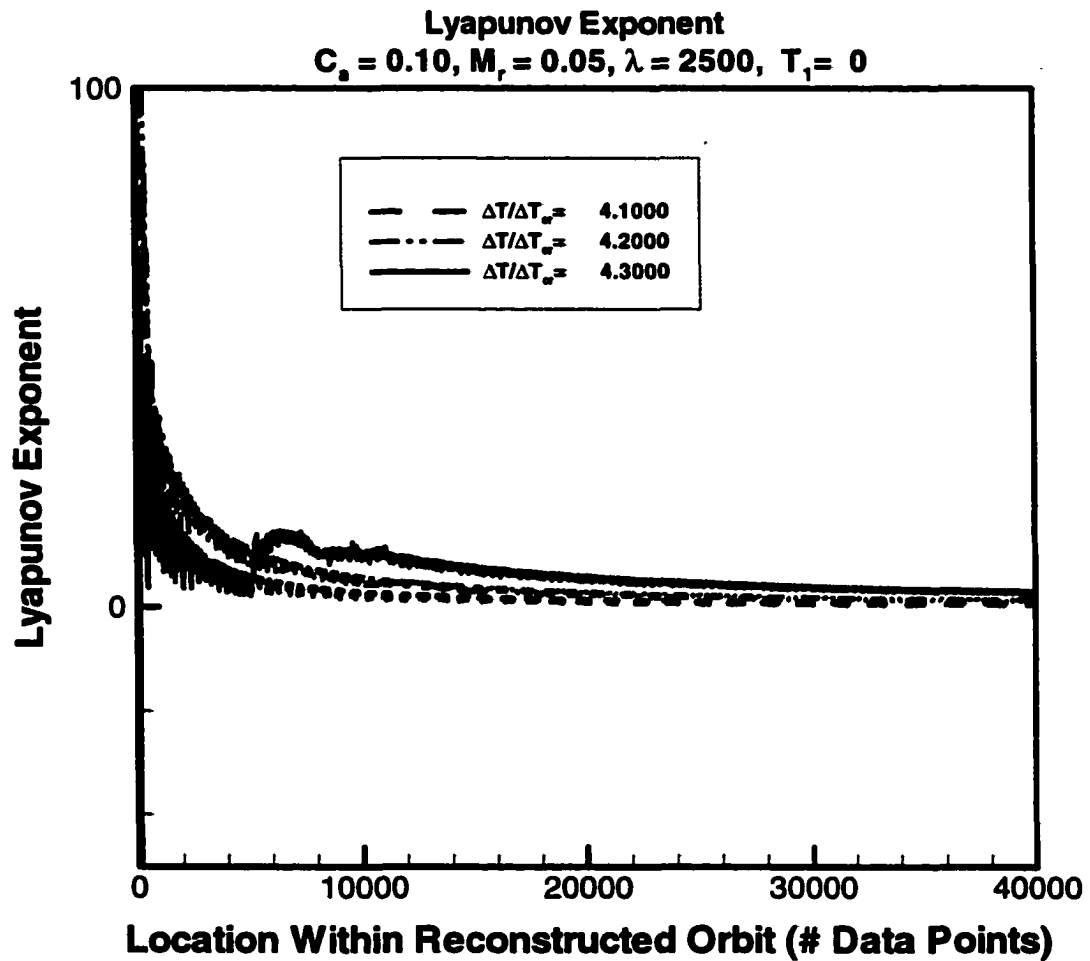
Fig. 4.14 Lyapunov components at the vicinity of first chaos observation for a simply supported, 12"× 12"× 0.05" aluminum panel at λ = 2500.0
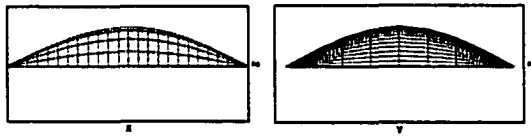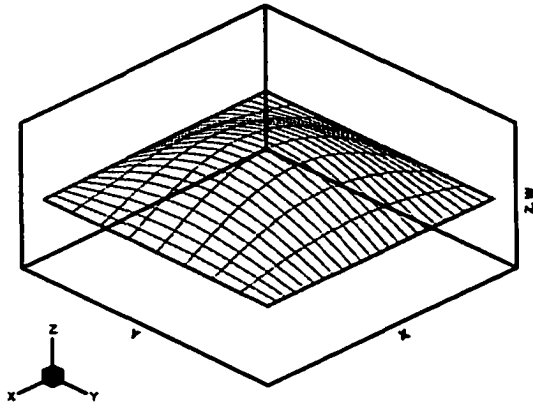
(a) Mode #1(1, 1)
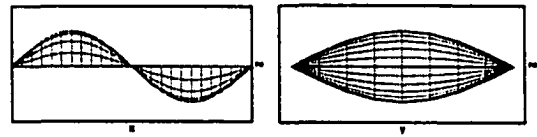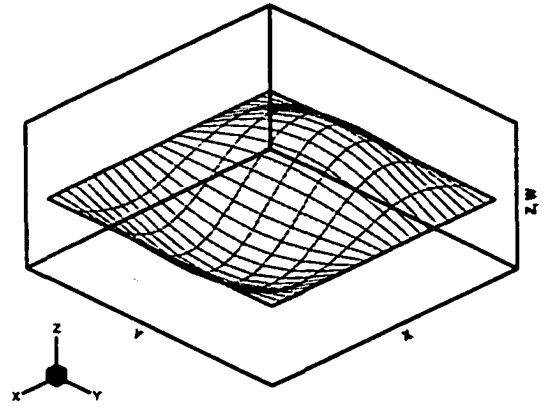
(b) Mode #3(2, 1)
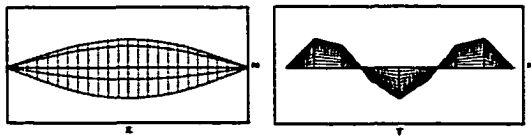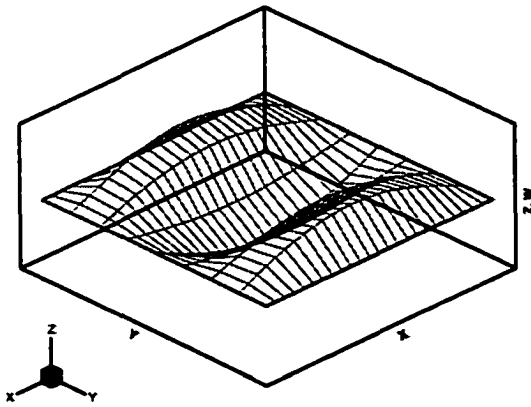
(c) Mode #5(1,3)
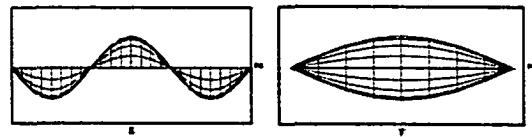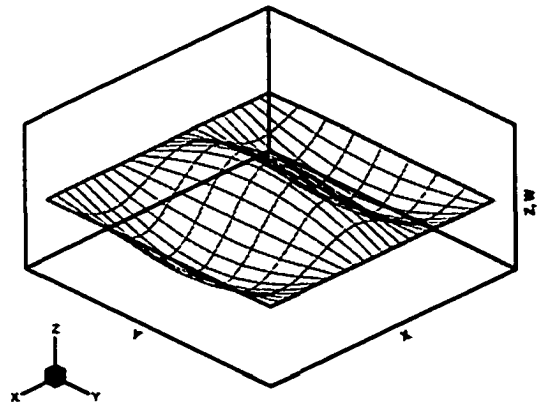
(d) Mode #6(3,1)
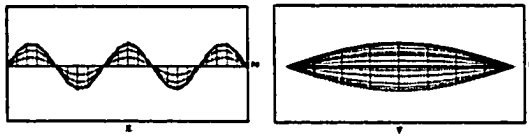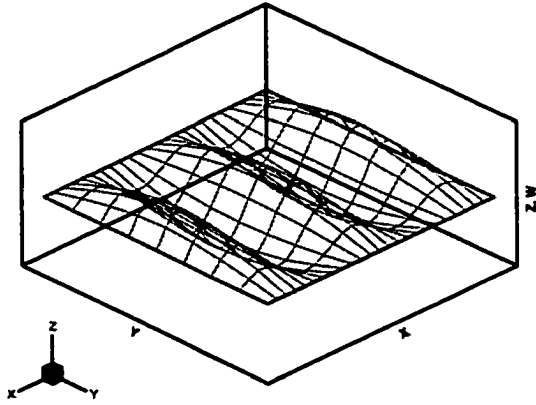
(i) Mode #18(5,1)
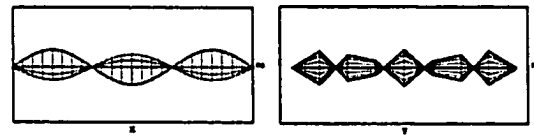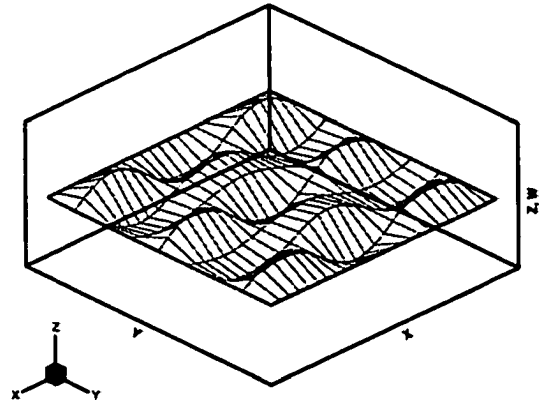
(j) Mode #21(3,5)
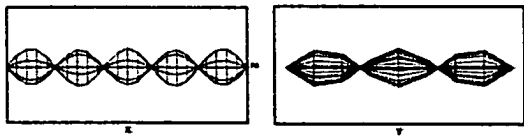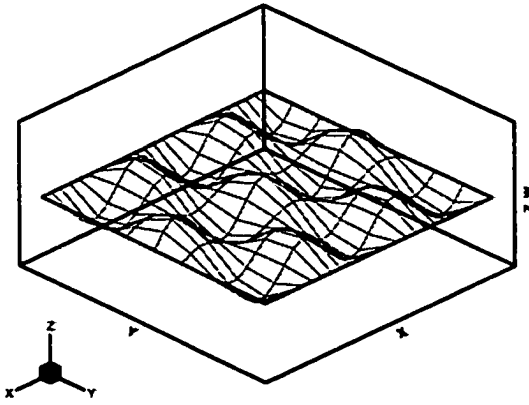
(k) Mode #23(5,3)
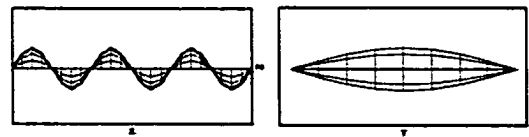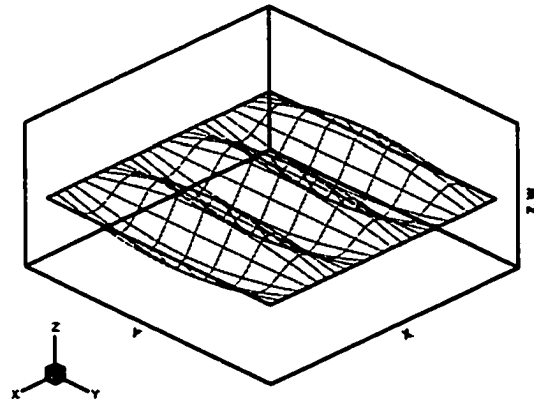
(l) Mode #27(6,1)
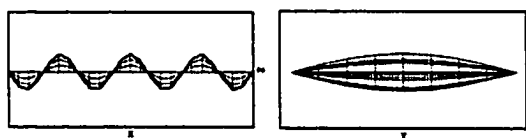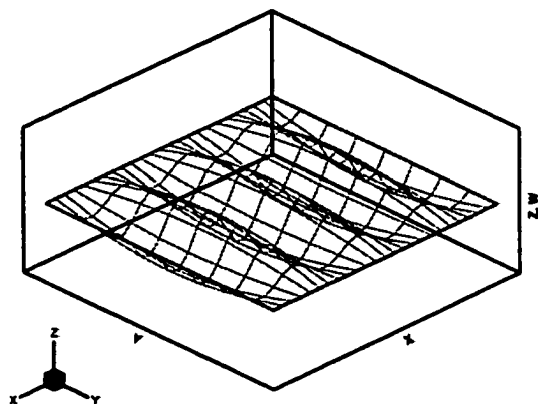
(m) Mode #37(7,1)
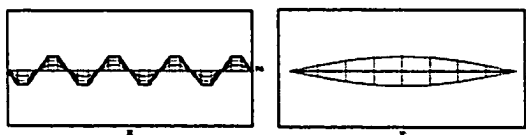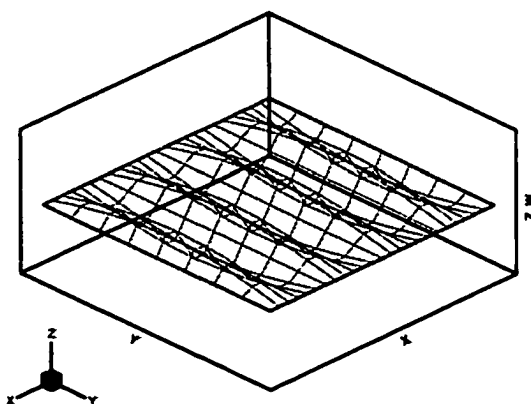
(n) Mode #49(8,1)

Fig. 4.15 Linear vibration mode shapes for a simply supported, 12″× 12″× 0.04″, single layer B/Al panel
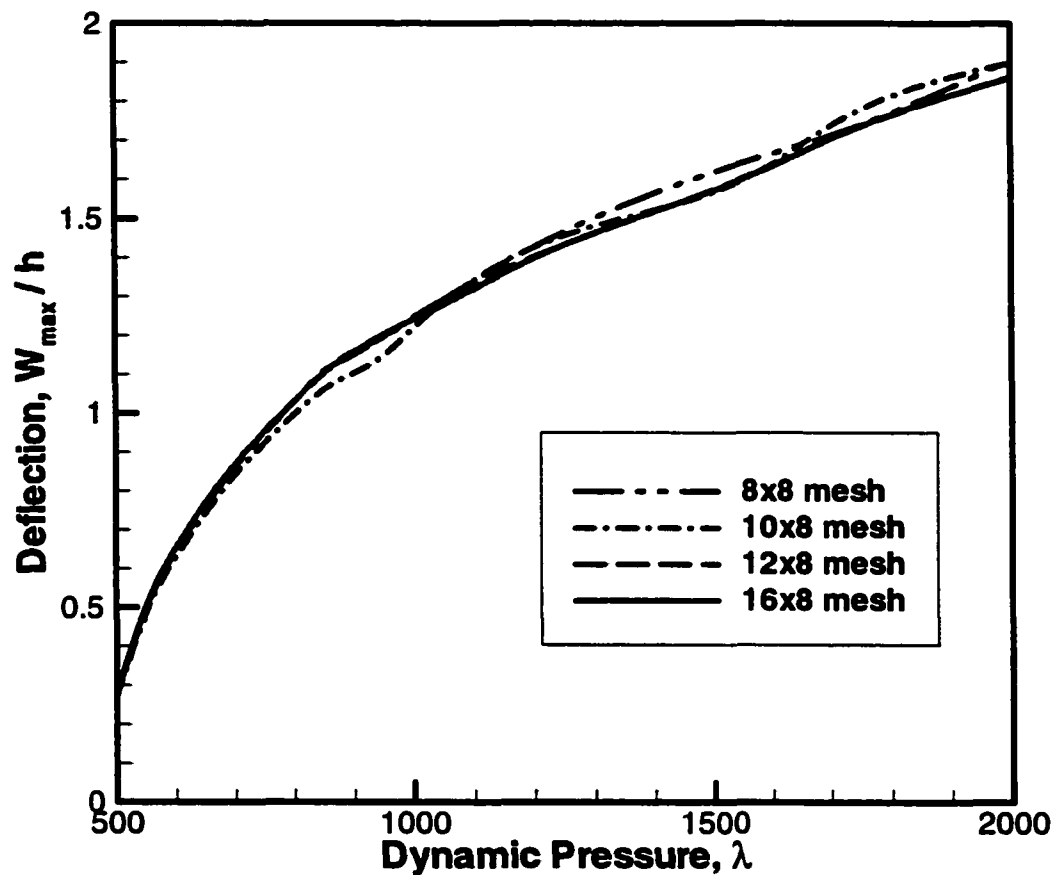
Fig. 4. 17 Mesh convergence study for a simply supported,
12″× 12″× 0.04″, single layer B/Al panel
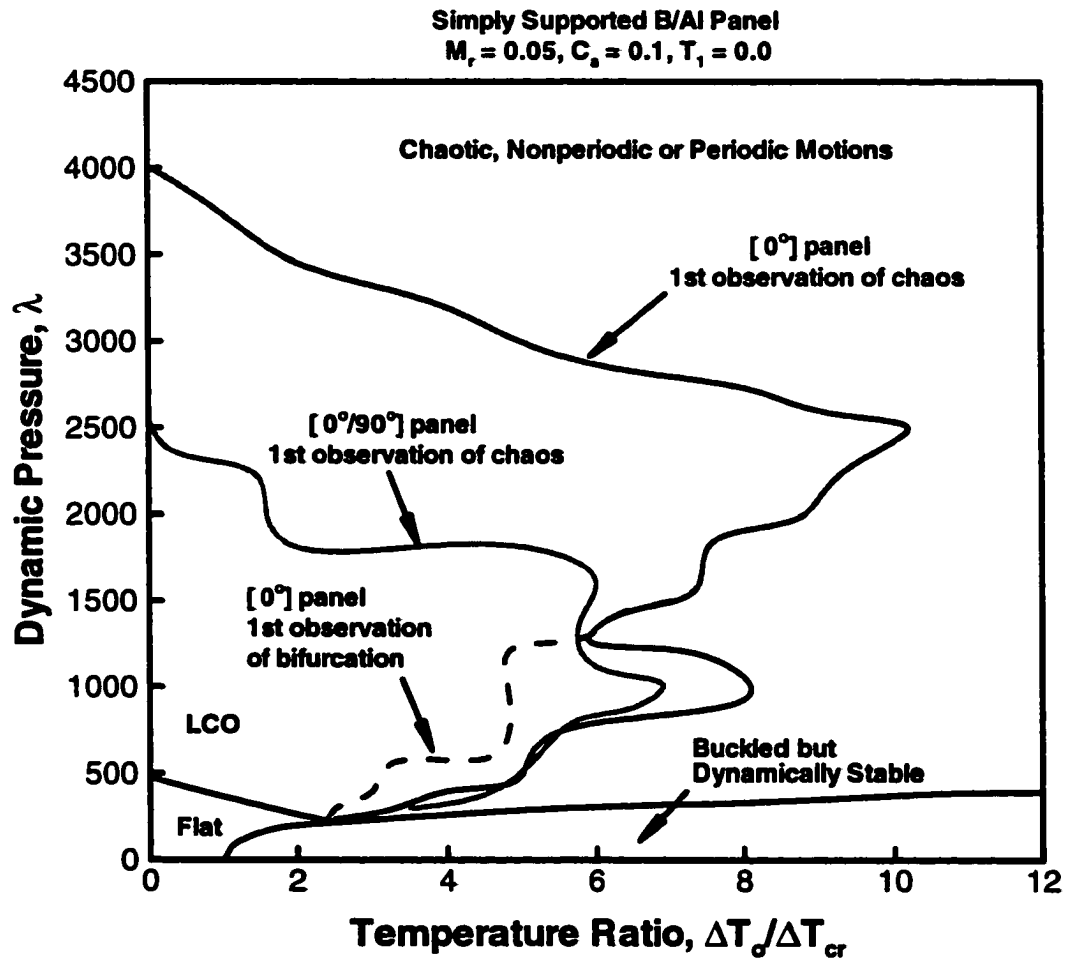
Fig. 4.18 Motion map for simply supported, [0] and [0/90], 12"× 12"× 0.04"B/Al panels

Bifurcation Diagram
$C_a = 0.10$, $M_r = 0.05$, $\lambda = 1200$, $T_1 = 0$
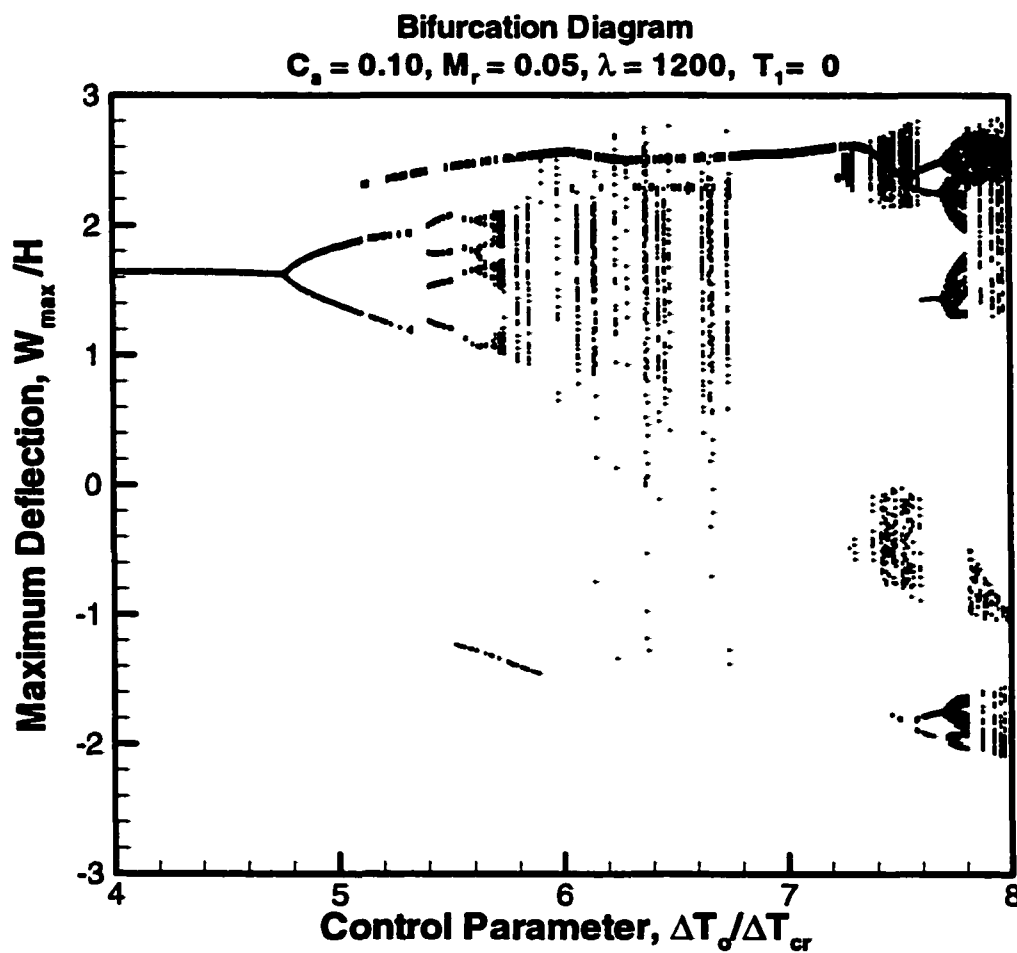
Fig. 4.19 Bifurcation diagram for a simply supported, [0], $12'' \times 12'' \times 0.04''$
B/Al panels at moderately high dynamic pressure

Bifurcation Diagram
$C_a = 0.10$, $M_r = 0.05$, $\lambda = 3200$, $T_1 = 0$

Y-axis: Maximum Deflection, W_{max}/H

X-axis: Control Parameter, $\Delta T_o/\Delta T_{cr}$
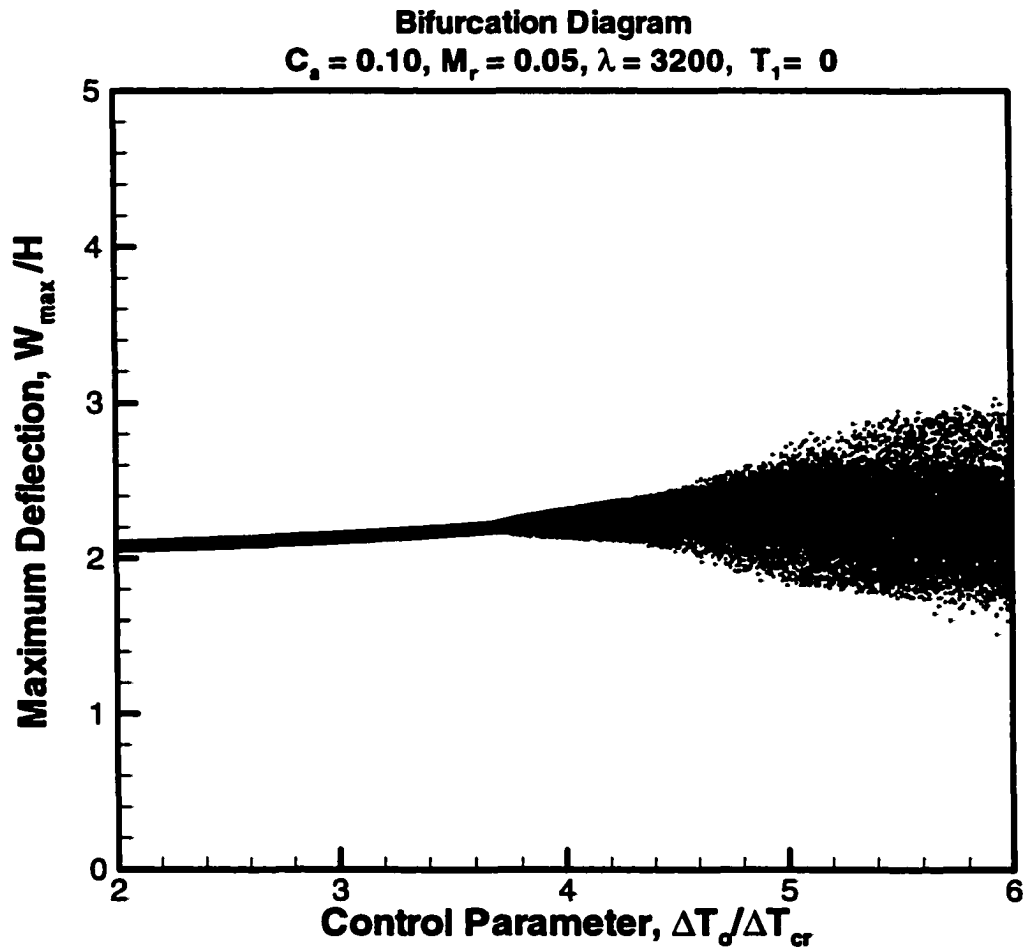
**Fig. 4.20 Bifurcation diagram for a simply supported, [0],
$12'' \times 12'' \times 0.04''$, B/Al panel at high dynamic pressure**

(a) $C_a = 0.01$

(b) $C_a = 0.1$
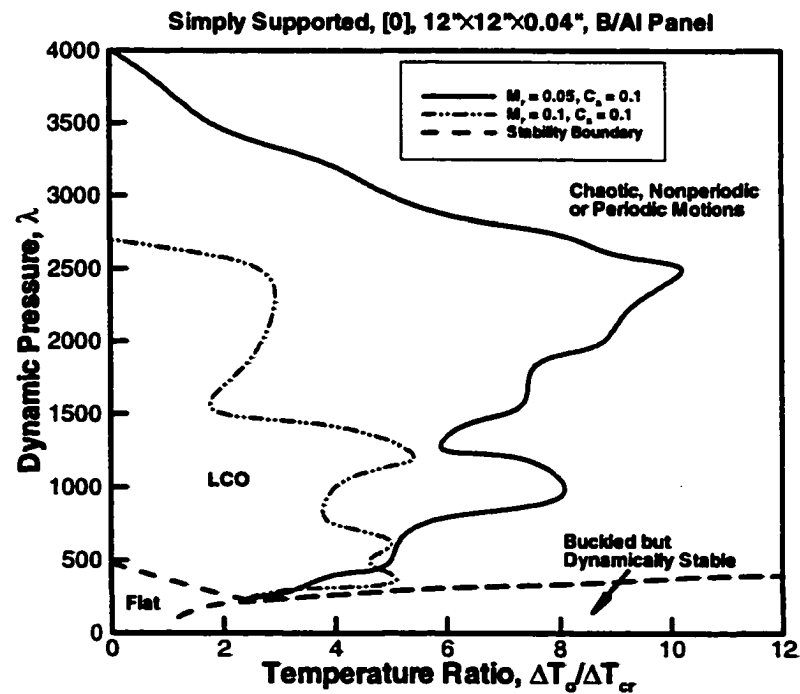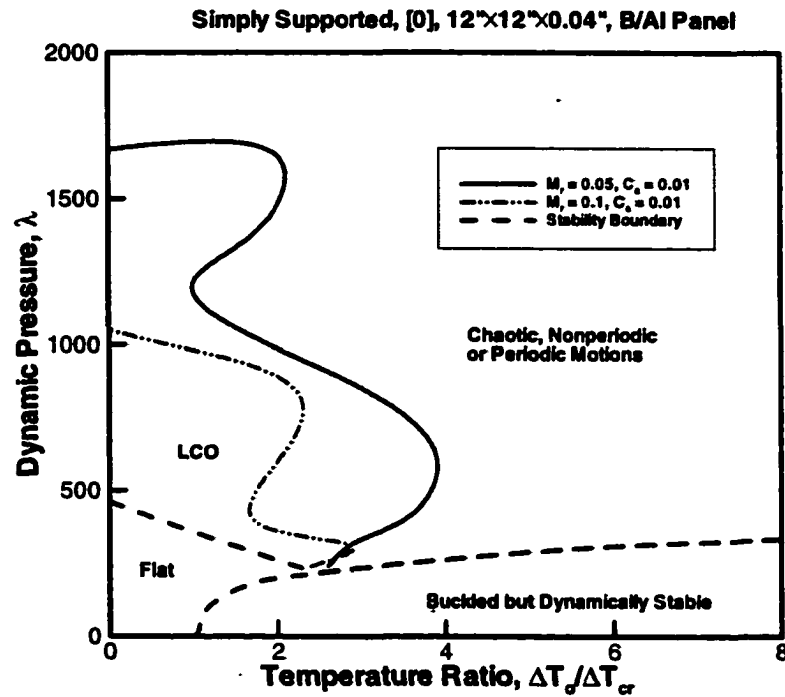
Fig. 4.21 Effects of Mach number on LCO region boundary
for simply supported, [0], $12'' \times 12'' \times 0.04''$B/Al panel

Simply Supported, [0], 12"×12"×0.04", B/Al Panel

Chaotic, Nonperiodic
or Periodic Motions

LCO

Temperature Ratio, $\Delta T_d/\Delta T_{cr}$

(a) $M_r = 0.05$

Simply Supported, [0], 12"×12"×0.04", B/Al Panel

Chaotic, Nonperiodic
or Periodic Motions

LCO

Temperature Ratio, $\Delta T_d/\Delta T_{cr}$

(b) $M_r = 0.1$
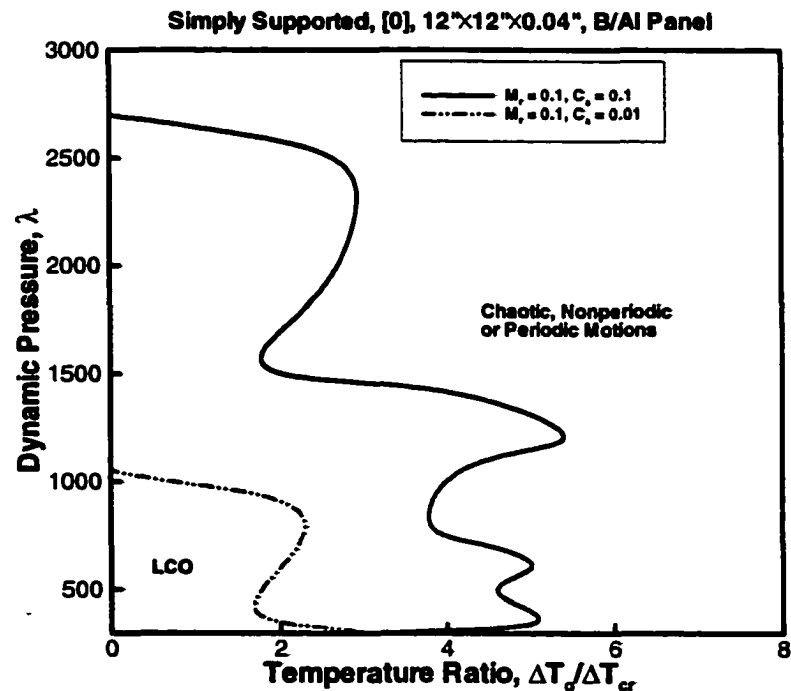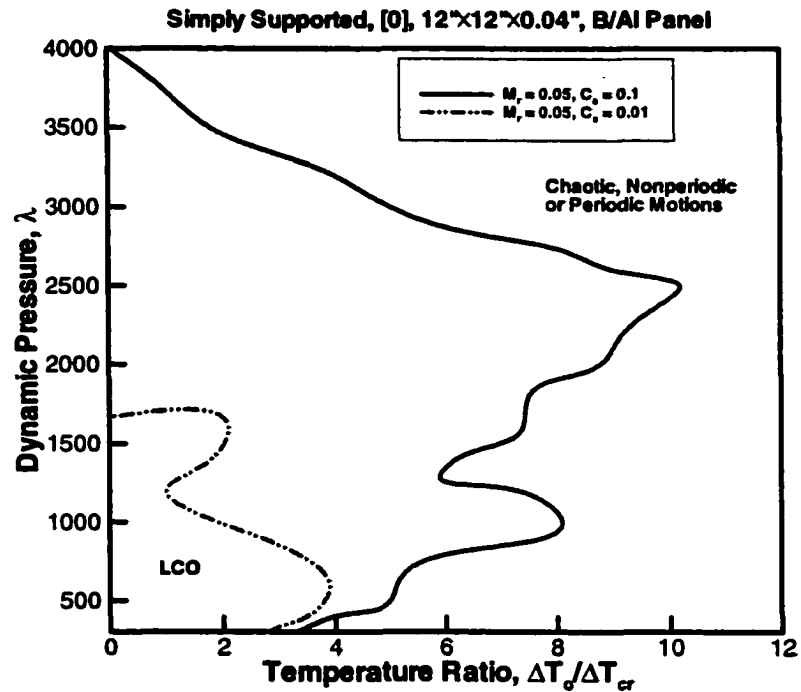
Fig. 4.22 Effects of aerodynamic damping on LCO region boundary for simply supported, [0], 12"× 12"× 0.04"B/Al panel
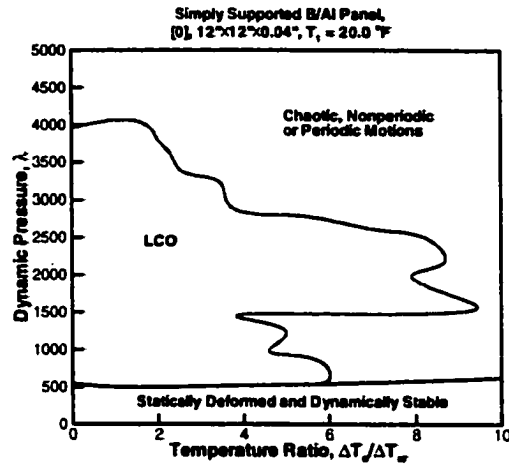
(a) $T_1 = 20.0\ ^\circ F$
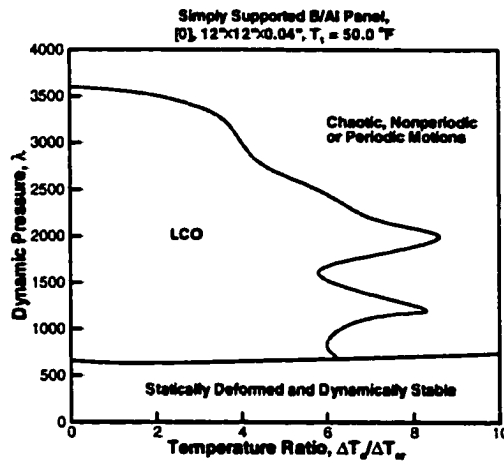
(a) $T_1 = 50.0\ ^\circ F$
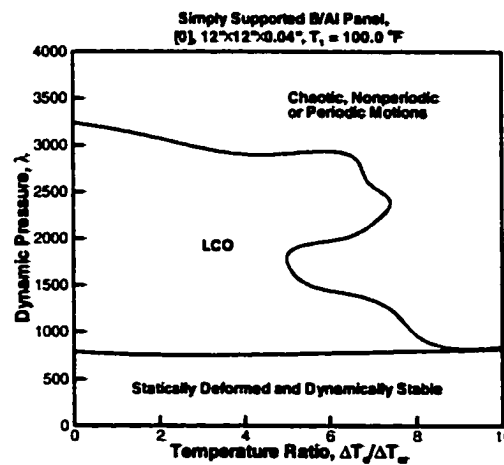
(a) $T_1 = 100.0\ ^\circ F$

Fig. 4.23 Motion maps for simply supported, [0], 12″× 12″× 0.04″B/Al panel with various temperature gradients across thickness
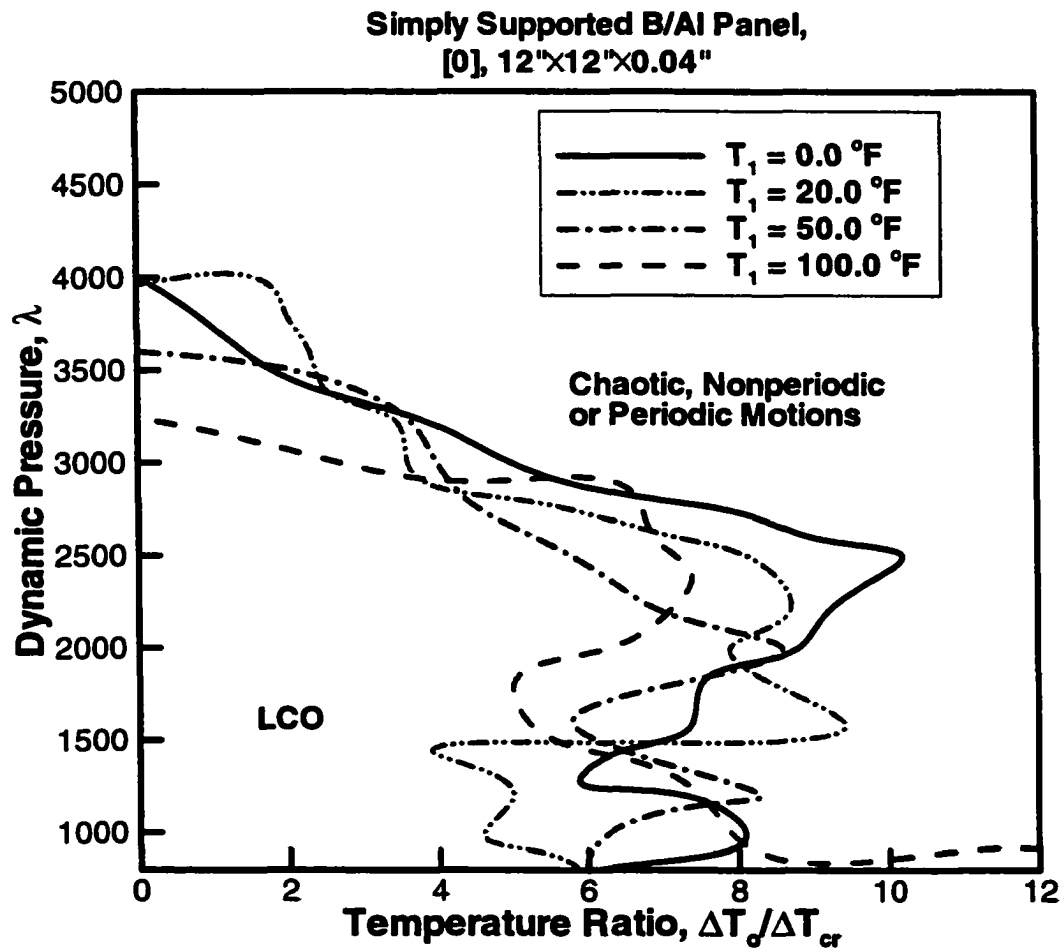
Fig. 4.24 Temperature gradient effects on boundary LCO region for simply supported, [0], 12"× 12"× 0.04"B/Al panel
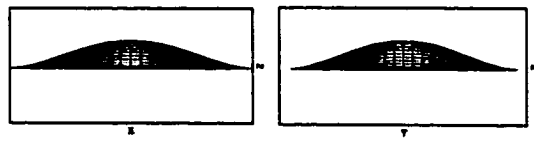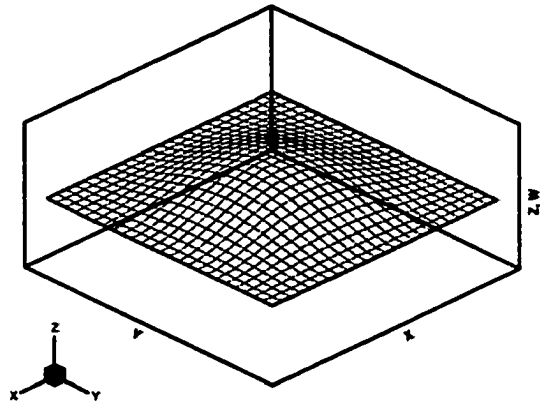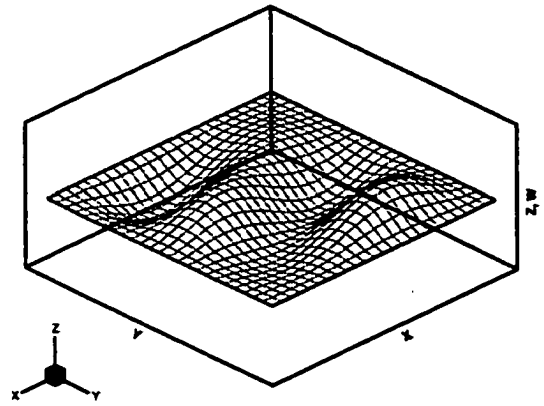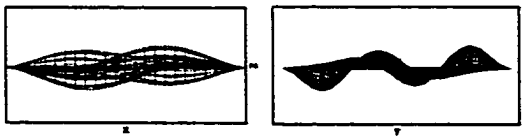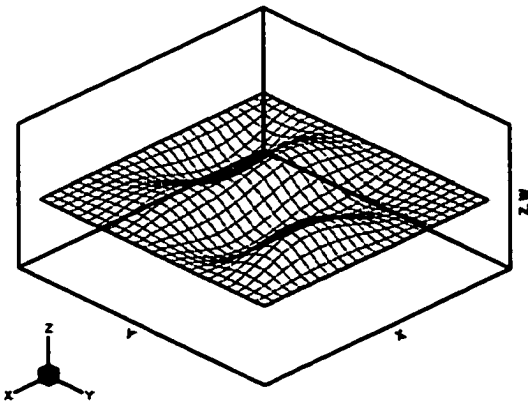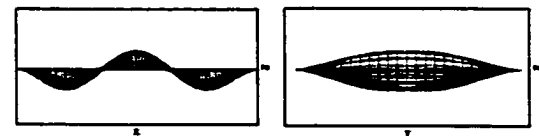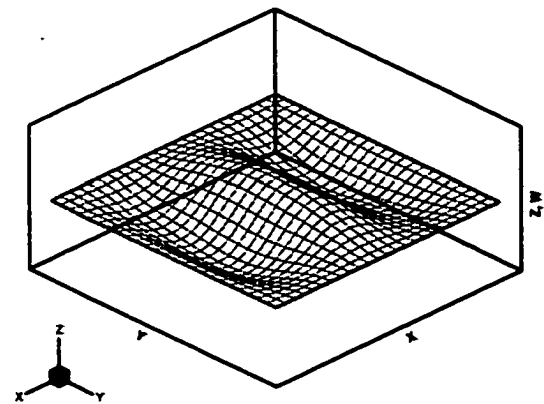
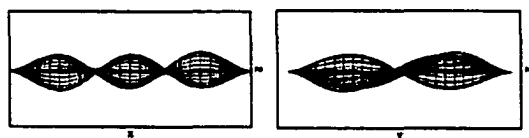(a) Mode #1(1, 1)
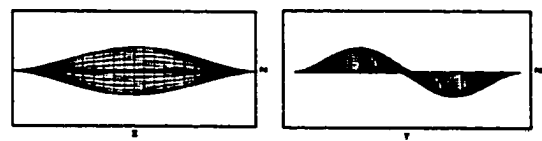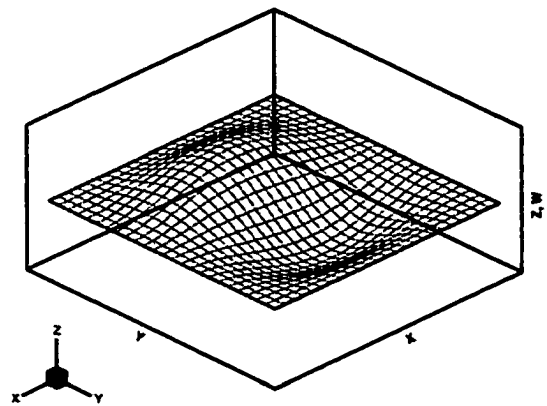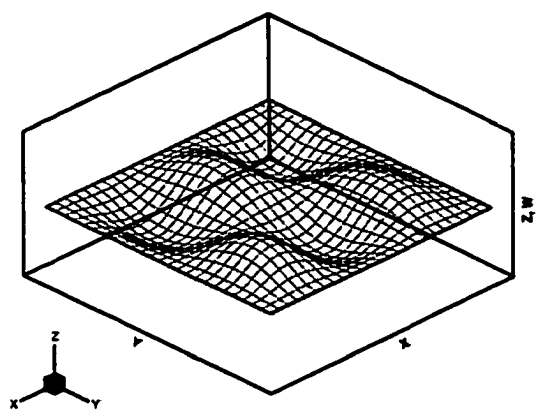
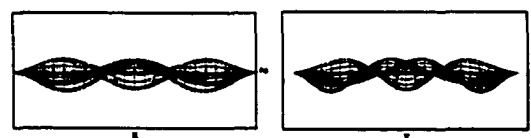(b) Mode #2(1, 2)
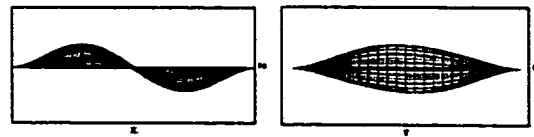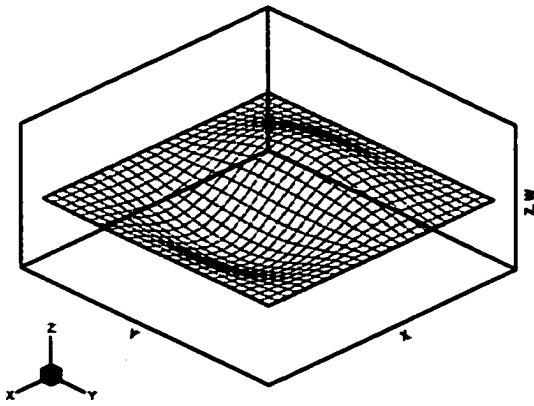
(c) Mode #3(2, 1)
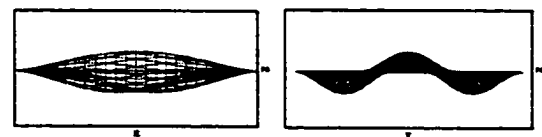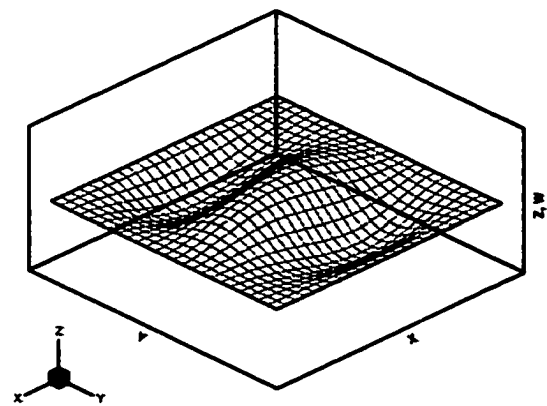
(d) Mode #4(1, 3)
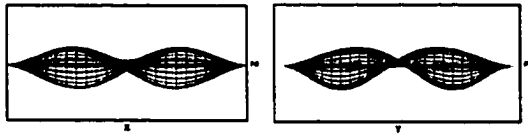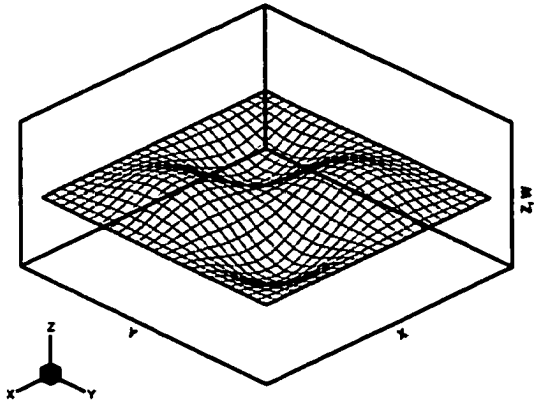
(e) Mode #5(2, 2)
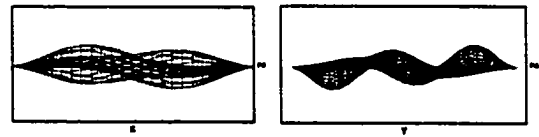
(f) Mode #6(2, 3)

(g) Mode #7(2, x)

(h) Mode #8(3, 1)

(i) Mode #10(3, 2)
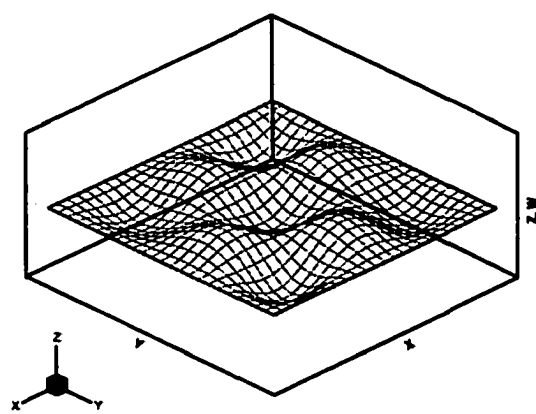
(j) Mode #12(3, 3)
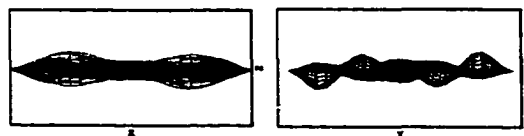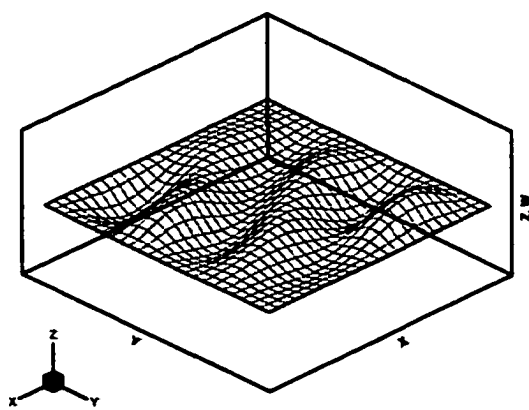
(k) Mode #13(x, x)
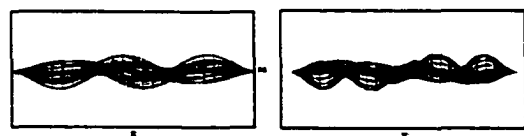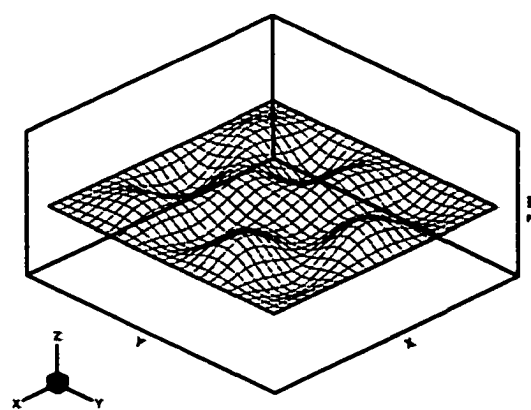
(l) Mode #14(3, x)
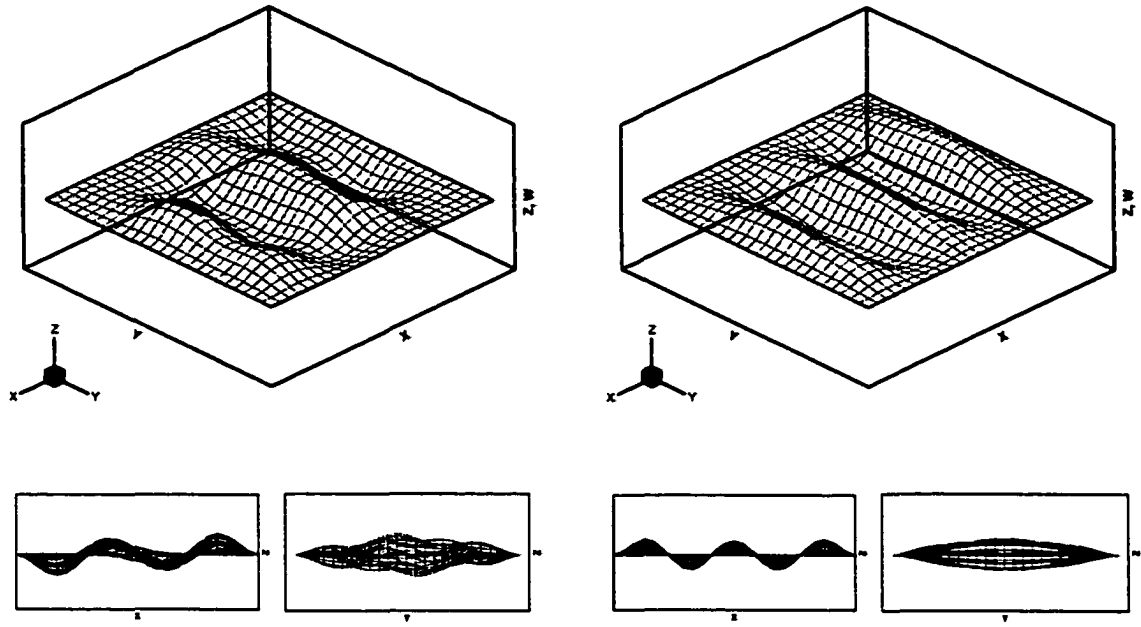
(m) Mode #15(4, 1)

(n) Mode #24(5, 1)
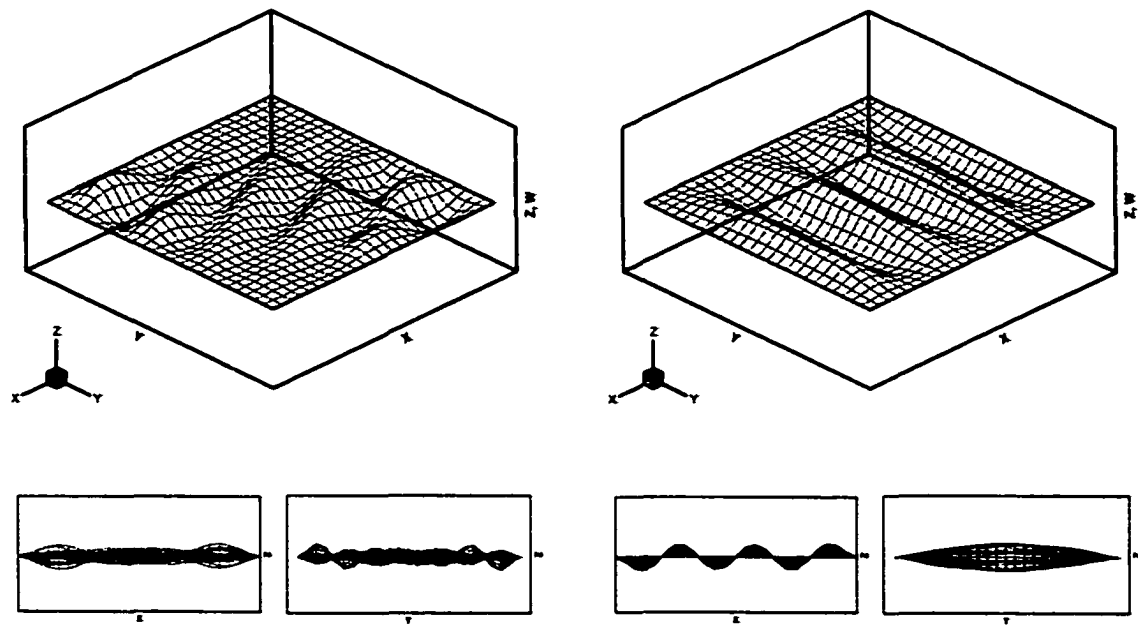
(o) Mode #34(x, x)

(p) Mode #35(6, 1)

**Fig. 4.25 Linear vibration mode shapes for a clamped,
12"× 12"× 0.048", [0/45/-45/90]ₛ, Gr/Ep panel**
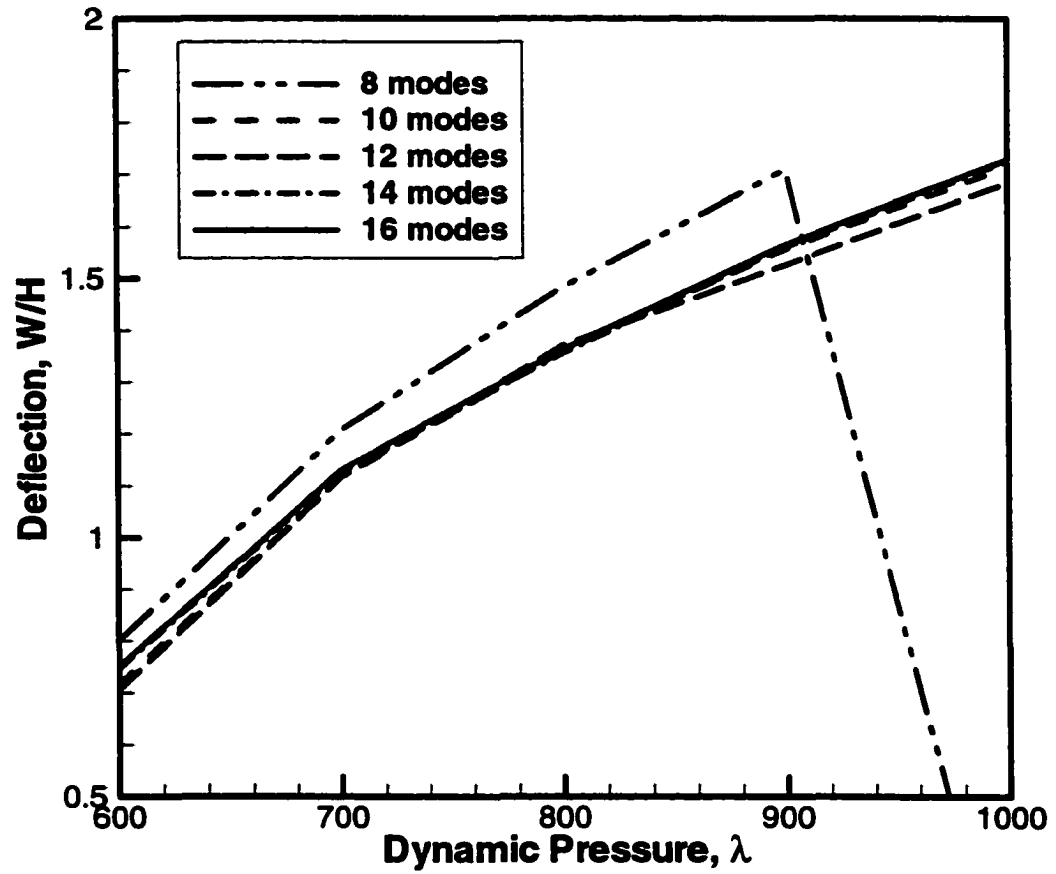
Fig. 4.26 Mode convergence study for a clamped,
12"× 12"× 0.048", [0/45/-45/90]$_s$, Gr/Ep panel
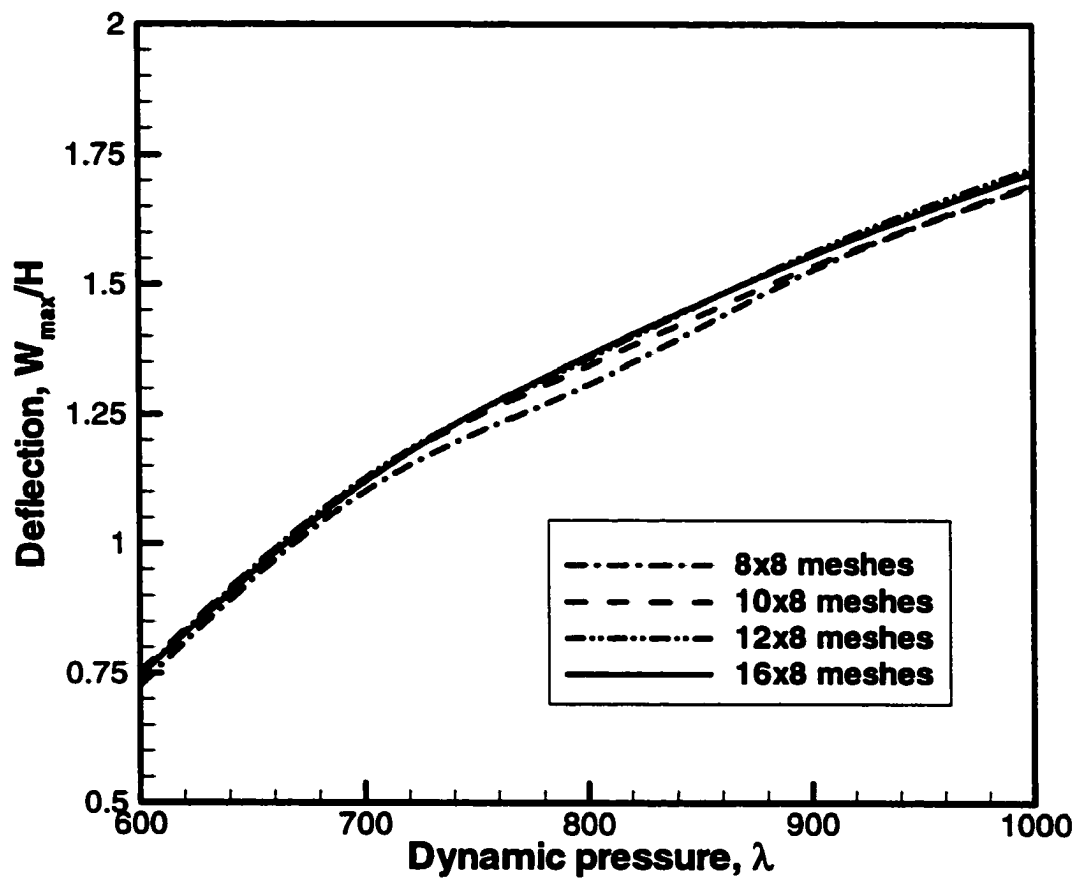
Fig. 4.27 Mesh convergence study for a clamped,
12"× 12"× 0.048", [0/45/-45/90]ₛ, Gr/Ep panel
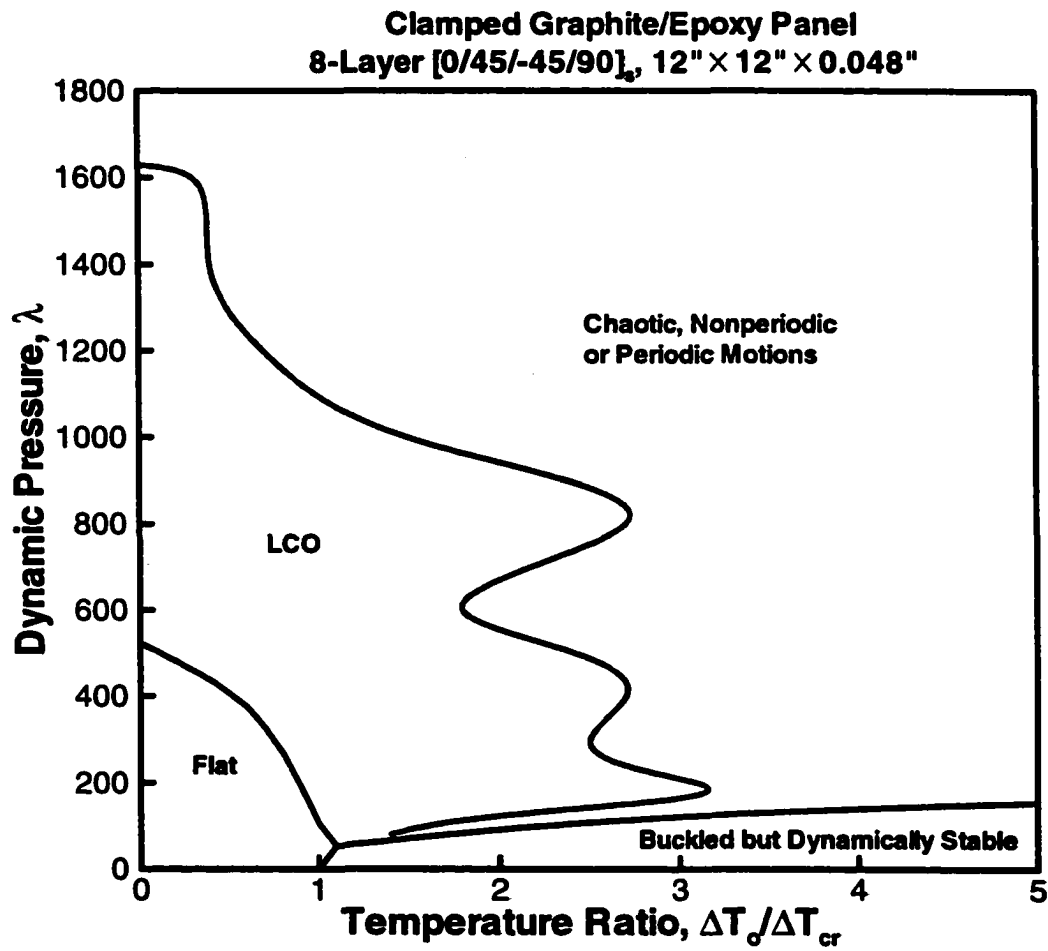
Fig. 4.28 Motion map for a clamped, [0/45/-45/90]$_s$, 12"× 12"× 0.04", Gr/Ep panel
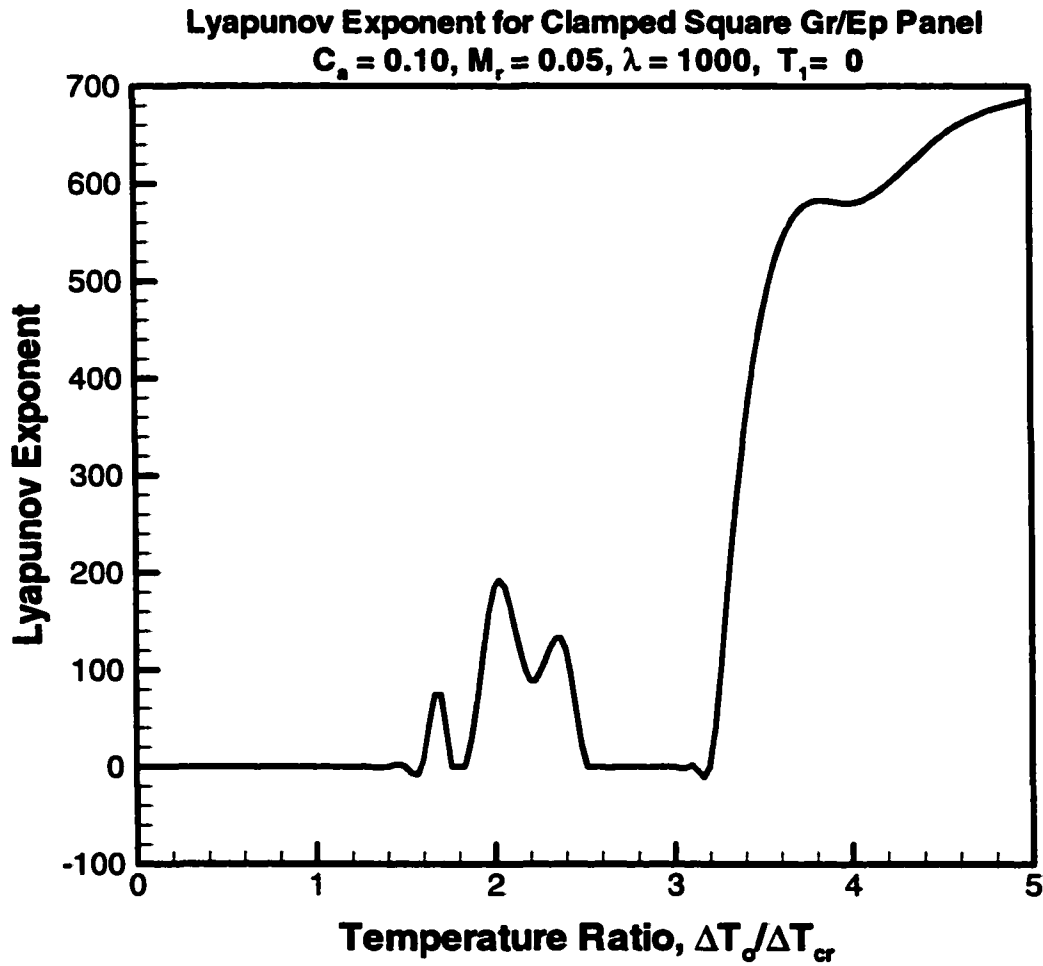
Fig. 4.30 Lyapunov exponents for a clamped, 12″× 12″×0.048″, [0/45/-45/90]ₛ, Graphite/Epoxy panel at λ = 1000.0

(a) 6-mode solution

(b) 8-mode solution

(c) 10-mode solution

(d) 14-mode solution
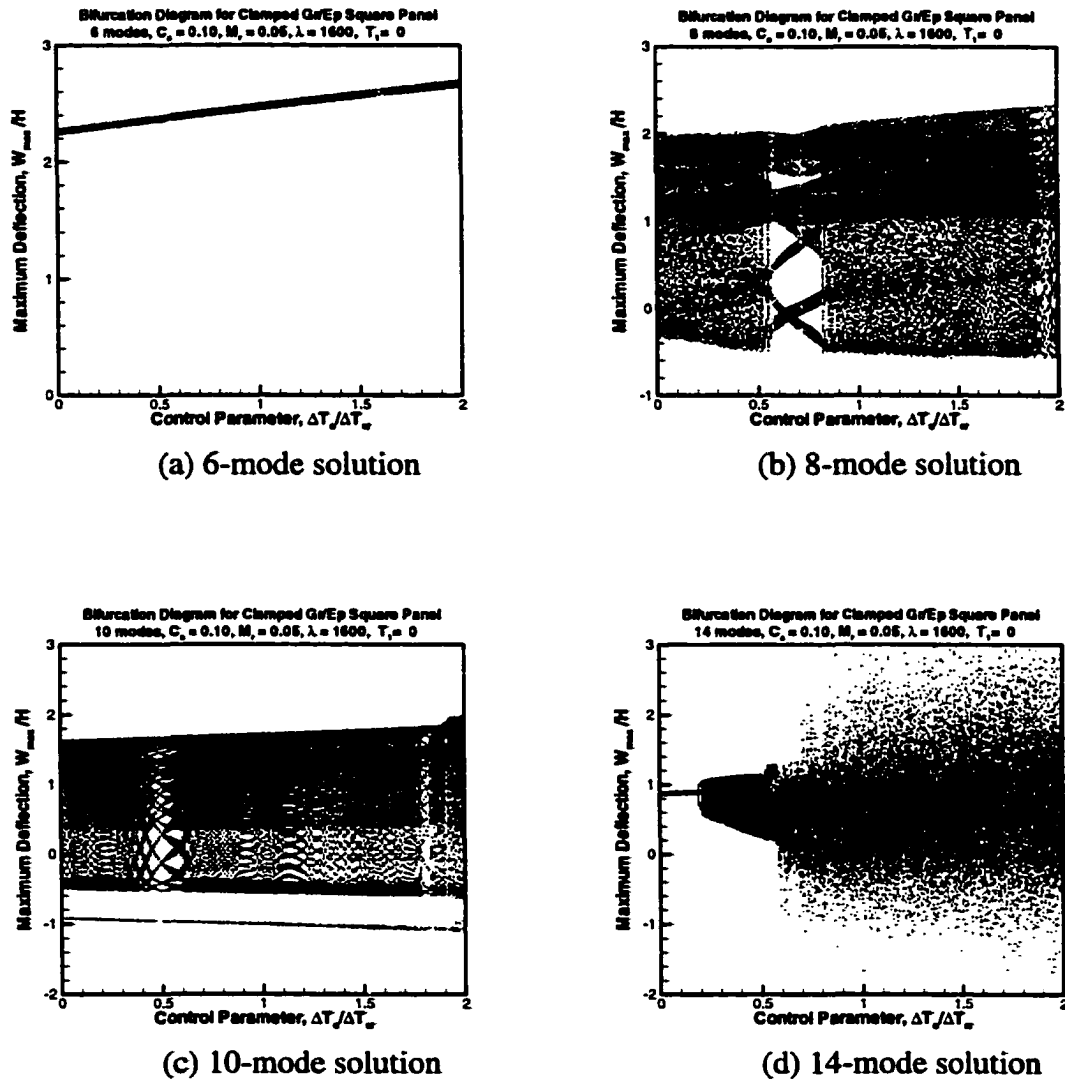
Fig. 4.31 Effects of insufficient modes on chaos evolution of a clamped, 12″× 12″×0.048″, [0/45/-45/90]ₛ, Graphite/Epoxy panel at λ = 1600.0
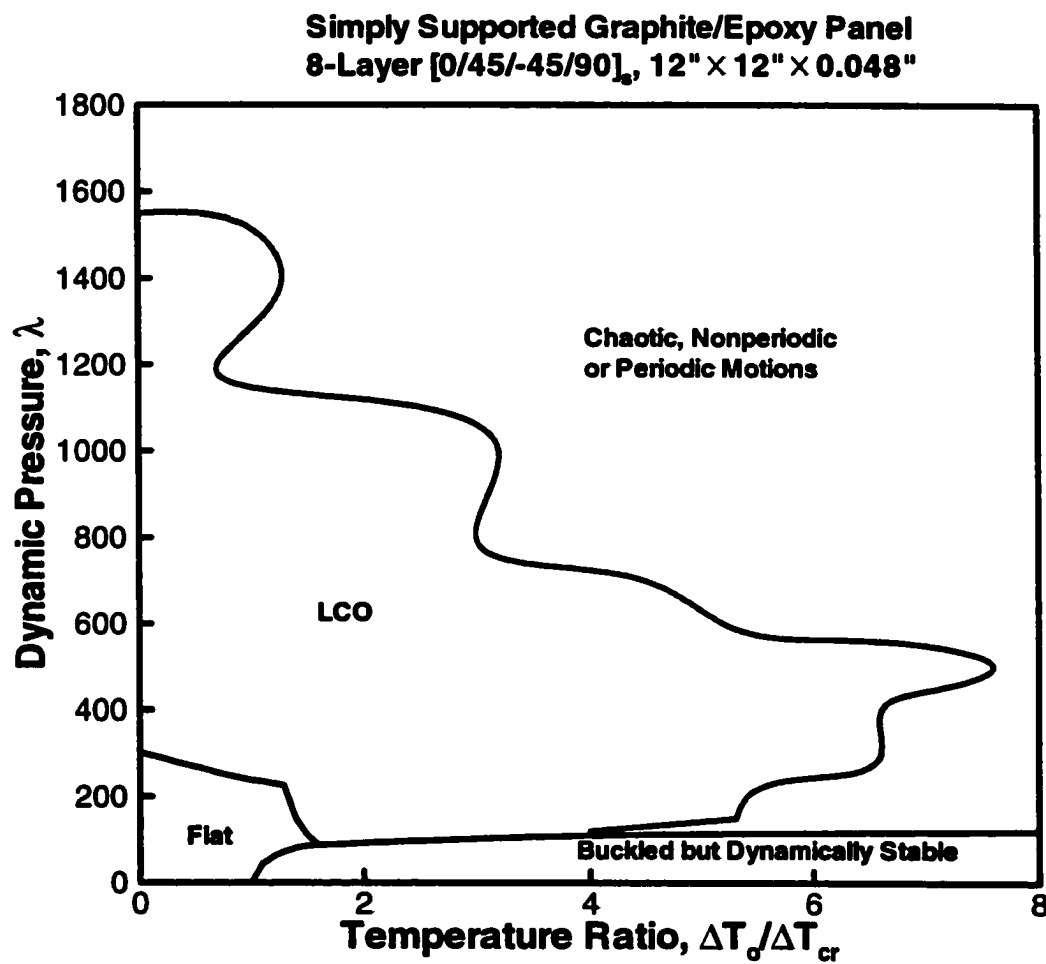
Fig. 4.32 Motion map for a simply supported, [0/45/-45/90]ₛ,
12″× 12″× 0.04″, Gr/Ep panel
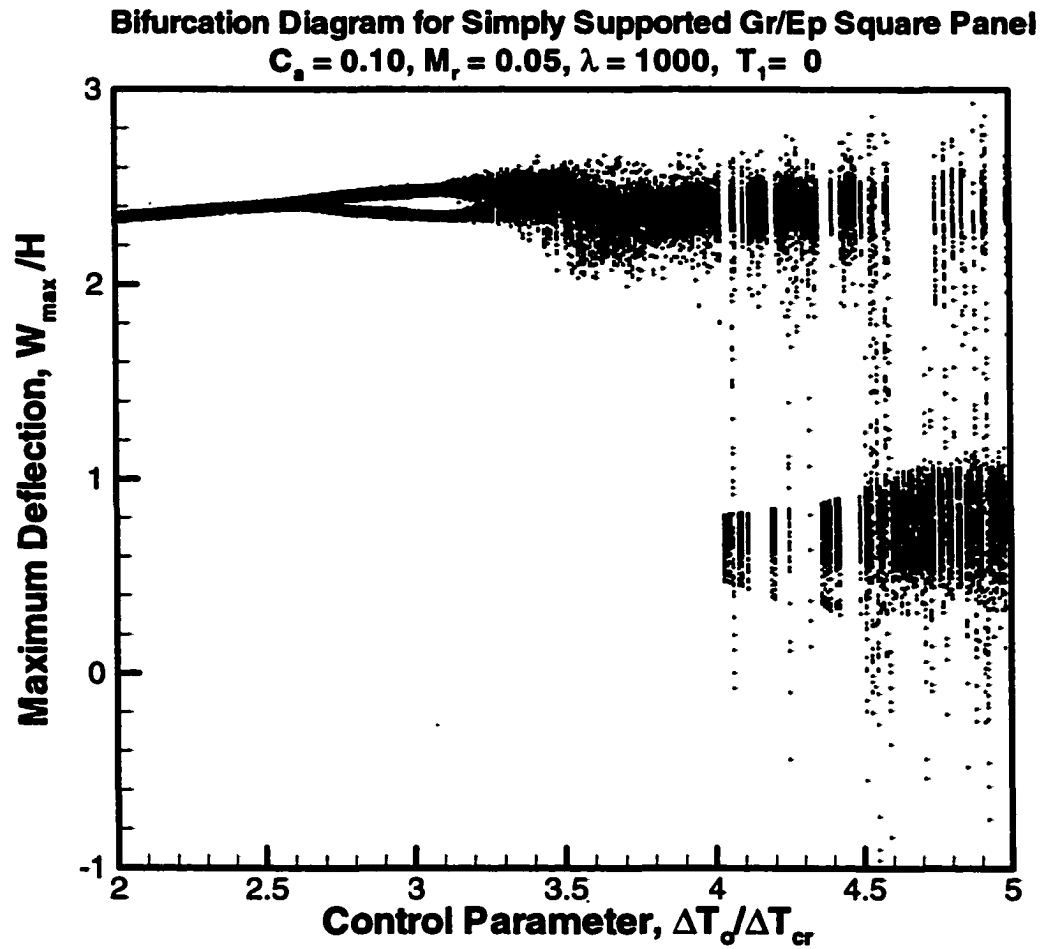
Fig. 4.33 Bifurcation diagram for a simply supported, 12″× 12″×0.048″, [0/45/-45/90]ₛ, Graphite/Epoxy panel at λ = 1000.0
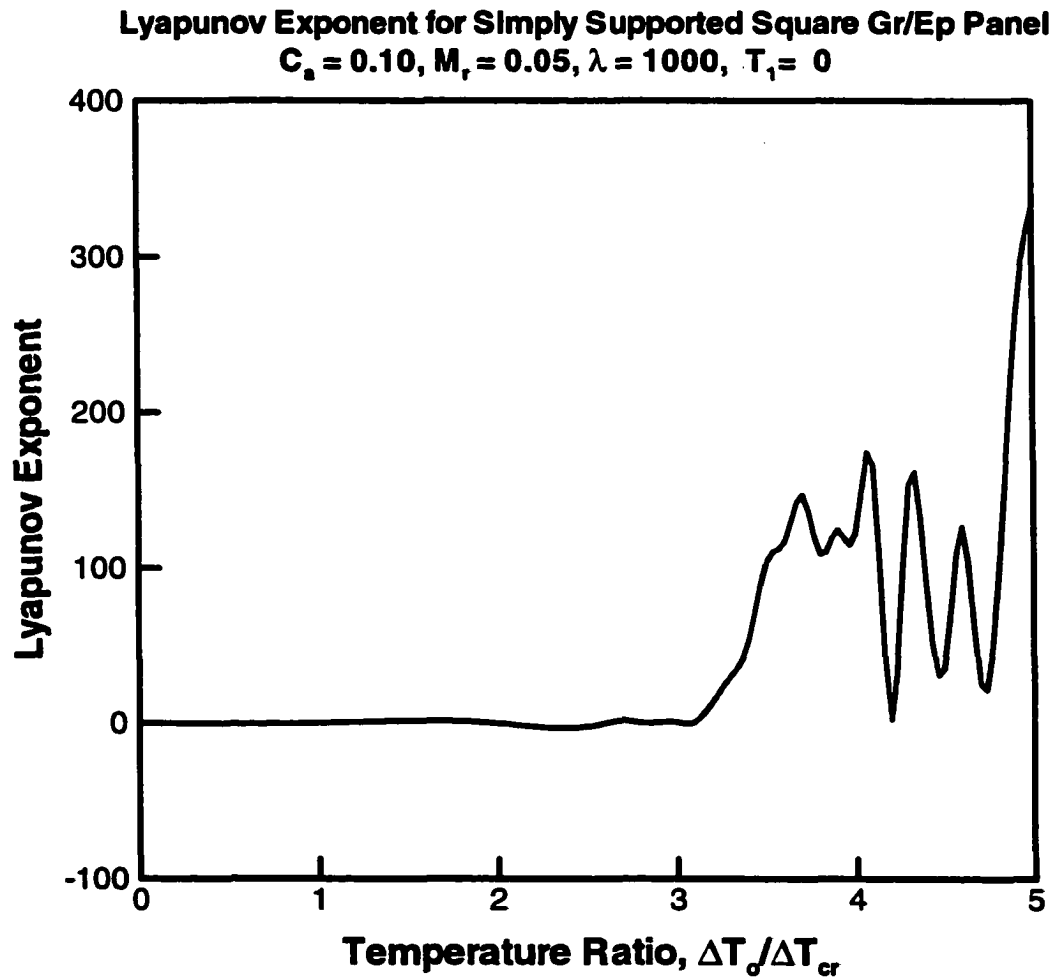
Fig. 4.34 Lyapunov exponents for a simply supported, 12"× 12"×0.048",
[0/45/-45/90]$_s$, Graphite/Epoxy panel at λ = 1000.0
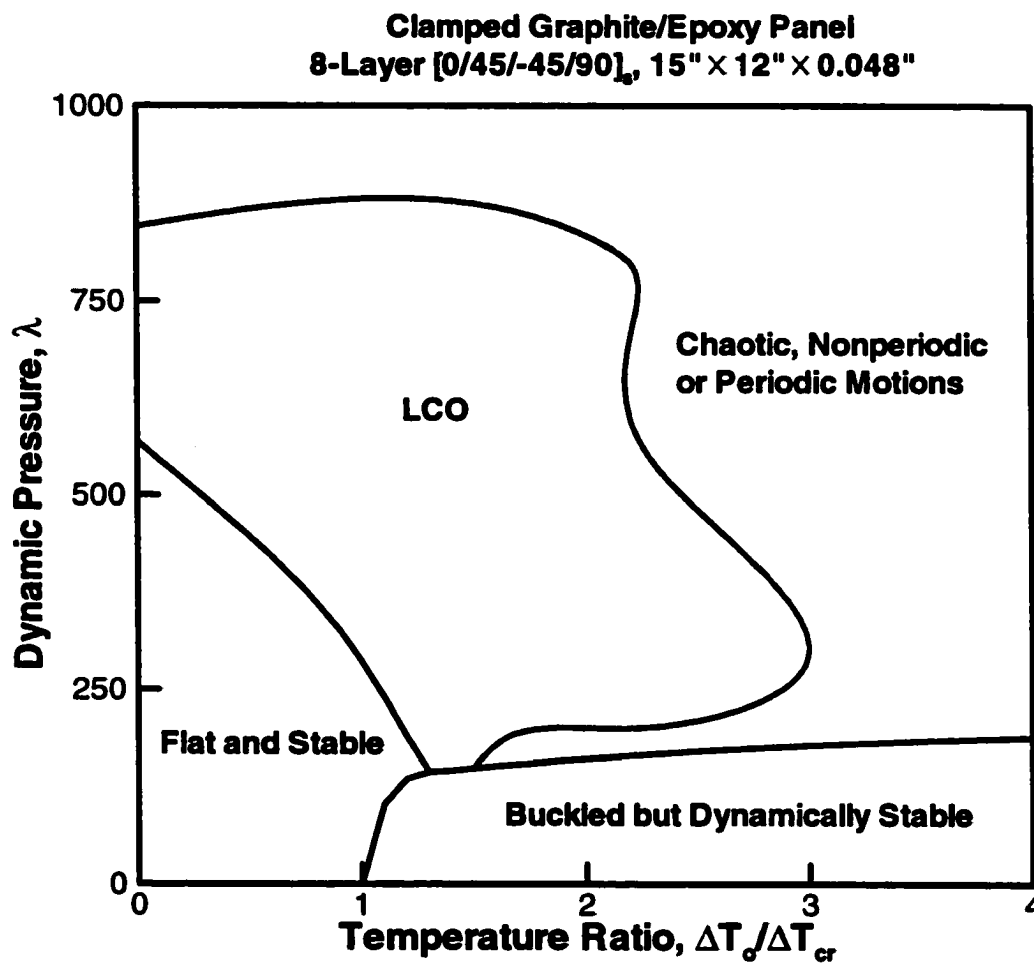
Fig. 4.35 Motion map for a clamped, [0/45/-45/90]$_s$,
15"× 12"× 0.04", Graphite/Epoxy panel
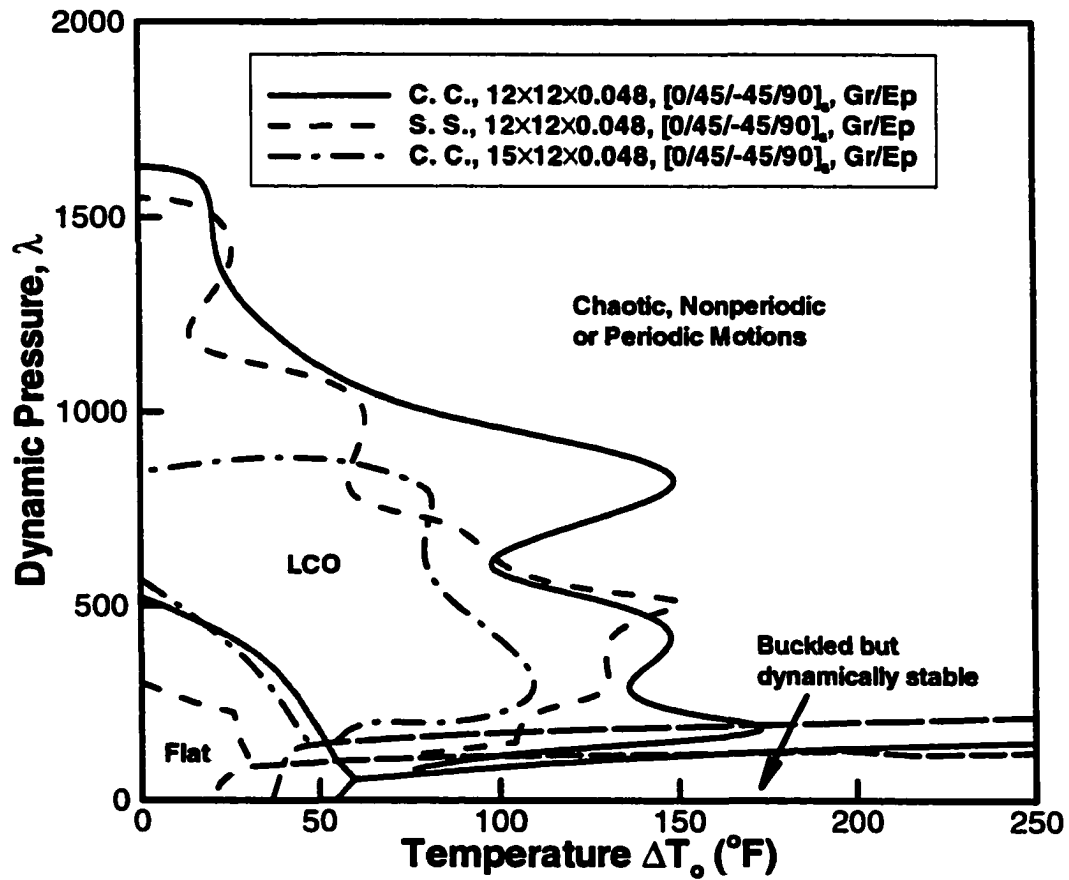
Fig. 4.36 Comparison of motion maps for Gr/Ep panels

CHAPTER V

SUMMARY AND CONCLUSIONS

The primary objective of this dissertation is to develop a finite element time domain modal formulation that could be applied to analyze the panel flutter problems arisen in high supersonic/hypersonic flight vehicle design. There exist analytical and finite element frequency domain methods for hypersonic panel flutter analysis in the literature. The analytical method has intrinsic limitations on processable panel material properties, supporting conditions, etc., so that it is very difficult or almost impossible to apply to advanced composite panels with complicated boundary conditions and/or anisotropic composite properties. The frequency domain method is limited to the LCO response analysis and since it is developed in physical coordinates, the large number of governing equations of motions makes it quite costly in computation time. Since aerodynamic heating is unavoidable in any supersonic/hypersonic vehicle, two types of thermal loading are incorporated into current formulation: the uniform temperature distribution and the temperature gradient across the panel thickness. High temperature induces another structural instability, i.e., thermal buckling, into concern for some panel designs. The two instability mechanisms, thermal buckling and panel flutter, interact with each other so that the panel could experience mainly five types of behavior: flat, buckled but dynamically stable, simple harmonic LCO, periodic LCO, and chaos. The time domain modal formulation presented is capable of identifying and investigating all possible panel behavior in a cost effective way. The efficiency comes from the dramatic reduction on the number of equations to be solved without losing too much accuracy.

In a practical point of view, the issue of mode selection must be clarified for any modal reduction approach. This is an easy task while using analytical methods since the modes are assumed by the analyst. However, the modes for finite element procedures are from eigenanalysis and complexity of material properties and supporting conditions cause a lot of confusions in mode selection. The mode filtering procedure proposed in present work is an initiative try to provide a systematic means to screen out the influential modes based upon the well-defined modal participation factor concept. This procedure is illustrated with examples of specially orthotropic panels and composite panels. For a 20-mode-base mode filtering procedure, typically within five or six runs, the important modes will stand out. Conclusions on mode selection for orthotropic panels by use of the finite element mode filtering procedure agree with conclusions made by applying analytical methods on at least one point, that is the flow direction modes, i.e., mode (n,1), n = 1, 2, 3,..., are important modes when flow angularity is not considered. However, the mode filtering procedure also suggests that modes other than the (n, 1) modes may contribute to the panel motion and are not neglectable, especially when composite panel is studied. Cautions must be taken while making decisions about which mode and how many modes to use while analyzing flutter response at high nondimensional dynamic pressure because higher order modes usually play important roles. The detriment of unwise mode selection scheme is also demonstrated.

Chaos is inevitable no matter there does/does not exist thermal loading. With the efficient finite element modal formulation, it is easy to detect and inspect chaos in many ways, such as time history, phase plane plot, Poincaré map and bifurcation diagram. The largest Lyapunov exponent can be evaluated on basis of data from direct time integration.

REFERENCES

[1] Bishlinghoff, R. L., Ashley, H. and Halfman R. L., "Aeroelasticity," Copyright © 1955 by Addison-Wesley Publishing Company, Inc, Dover Publications, Inc., 1996.

[2] Dowell, E. H., "Aeroelasticity of Plates and Shells," Noordhoff International Publishing, Lyden, the Netherlands, 1975.

[3] Librescu, L. "Elastostatics and Kinetics of Anisotropic and Heterogeneous Shell-type Structures, " Noordhoff International Publishing, Lyden, the Netherlands, 1975.

[4] Fung, Y. C., "A Summary of the Theories and Experiments on Panel Flutter," AFOSR TN 60-224, May 1960, Guggenheim Aeronautical Lab., California Institute of Technology, Pasadena, CA.

[5] Johns, D. J., "The Present Status of Panel Flutter," AGARD Report 484, 1961, Advisory Group for Aeronautic Research and Development.

[6] Johns, D. J., "A Survey on Panel Flutter," Advisory Report 1, Nov. 1965, Advisory Group for Aeronautic & Research and Development.

[7] Dowell, E. H., "Panel Flutter: A Review of the Aeroelastic Stability of Plates and Shells," AIAA Journal, Vol. 8, No. 3, 1970, pp. 385-399.

[8] Mei, C., Abdel-Motagaly, K., and Chen, R., "Review of Nonlinear Panel Flutter at Supersonic and Hypersonic Speeds," Applied Mechanics Reviews, Vol. 52, No. 10, Oct. 1999, pp. 321-332.

[9] Gray, C. E. and Mei, C., "Large Amplitude Finite Element Flutter Analysis of Composites Panels in Hypersonic Flow," AIAA Journal, Vol. 31, No. 6, June 1993, pp. 1090-1099.

[19] Eisley, J. G., "The Flutter of a Two-Dimensional Buckled Plate with Clamped Edges in a Supersonic Flow," OSR-TN-56-296, July 1956.

[20] Houboult, J. C., "A Study of Several Aerothermoelastic Problems of Aircraft Structures in High-Speed Flight", Ph. D. Thesis, Eidenössischen Technischen Hochschule, The Swiss Federal Institute of Technology, Zurich, Switzerland, 1958.

[21] Fung, Y. C., "On Two-Dimensional Panel Flutter," Journal of the Aeronautical Sciences, Vol. 25, March 1958, pp. 145- 160.

[22] Bolotin, V. V., "Nonconservative Problems of the Theory of Elastic Stability," McMillan Co., New York, 1963, pp. 199-312.

[23] Chu, H.-N. and Herrmann, G., "Influence of Large Amplitudes on Free Flexural Vibration of Rectangular Elastic Plates," Journal of Applied Mechanics, Vol. 23, 1956, pp. 532-540.

[24] Ashley, H. and Zartarian, G., "Piston Theory - A New Aerodynamic Tool for the Aeroelastician," Journal of Aeronautical Science, Vol. 23, No. 10, 1956, pp. 1109-1118.

[25] Dowell, E. H., and Voss, H. M., "Experimental and Theoretical Panel Flutter Studies in Mach Number Range 1.0 to 5.0," AIAA Journal, Vol. 3, No. 12, 1965, pp. 2292-2304.

[26] Dowell, E. H., "Nonlinear Oscillation of a Fluttering Plate I," AIAA Journal, Vol. 4, No. 7, 1966, pp. 1267-1275.

[27] Dowell, E. H., "Nonlinear Oscillation of a Fluttering Plate II," AIAA Journal, Vol. 5, No. 10, 1967, pp. 1856-1862.

[28] Fralich, R. W., "Postbuckling Effects on the Flutter of Simply Supported Rectangular Panels at Supersonic Speed," NASA TN D-1615, Mach 1965.

[29] Ventres, C. S., "Nonlinear Flutter of Clamped Plates," Ph.D. Dissertation, Princeton University, 1970.

[30] Librescu, L., "Aeroelastic Stability of Orthotropic Heterogeneous Thin Plates in the Vicinity of Flutter Critical Boundary," Journal de Mecanique, Vol. 4, No. 1, 1965, pp. 51-76.

[31] Kobayashi, S., "Flutter of Simply Supported Rectangular Panels in a Supersonic Flow – Two-Dimensional Panel Flutter, I - Simply supported Panel, II – Clamped Panel," Transaction of Japan Society of Aeronautical and Space Sciences, Vol. 5, 1962, pp. 79-118.

[32] Yuen, S. W., and Lau, S. L., "Effect of In-Plane Load on Nonlinear Panel Flutter by Incremental Harmonic Balance Method," AIAA Journal, Vol. 29, No. 9, 1991, pp. 1472-1479.

[33] Eslami, H., "Nonlinear Flutter and Forced Oscillations of Rectangular Symmetric Cross-Ply and Orthotropic Panels Using Harmonic Balance and Perturbation Methods," Ph. D. Dissertation, Old Dominion University, 1987.

[34] Morino, L., "A Perturbation Method for Treating Nonlinear Panel Flutter Problems," AIAA Journal, Vol. 7, No. 3, 1969, pp. 405-410.

[35] Morino, L. and Kuo, C. C., "Detailed Extensions of Perturbation Methods for Nonlinear Panel Flutter," ASRL TR 164-2, M.I.T., Cambridge, MA (March 1971).

[36] Smith, L. and Morino, L. "Stability Analysis of Nonlinear Differential Autonomous Systems with Applications to Flutter," AIAA Journal, Vol. 14, No. 3, 1976, pp. 333-341.

[37] Kuo, C. C., Morino, L., and Dugundji, L., "Pertubation and Harmonic Balance for Treating Nonlinear Panel Flutter," AIAA Journal, Vol. 10, No. 11, 1972, pp. 1479-1484.

[38] Olson, M. D., "Finite Element Approach to Panel Flutter," *AIAA Journal*, Vol. 5, No. 12, 1967, pp. 226-227.

[39] Olson, M. D., "Some Flutter Solutions using Finite Element," *AIAA Journal*, Vol. 8, No. 4, 1970, pp. 747-752.

[40] Appa, K. and Somashekar, B. R., "Application of Matrix Displacement Methods in the Study of Panel Flutter," AIAA Journal, Vol. 7, No. 1, January 1969, pp. 50-53.

[41] Sander, G., Bon, C. and Geradin, M., "Finite Element Analysis of Supersonic Panel Flutter," *International Journal for Numerical Methods in Engineering*, Vol. 7, No. 3, 1973, pp. 379-394.

[42] Yang, T. Y. and Sung, S. H., "Finite Element in Three-Dimensional Supersonic Unsteady Potential Flow," AIAA Journal, Vol. 15, No. 12, December 1977, pp. 1677-1683.

[43] Mei, C., "A Finite Element Approach for Nonlinear Panel Flutter," AIAA Journal, Vol. 15, No. 8, August 1977, pp. 1107-1110.

[44] Mei, C. and Rogers, J. L., Jr., "Application of NASTRAN to Large Deflection Supersonic Flutter of Panels," NASA TM X-3428, October 1976, pp. 67-98.

[45] Rao, K. S. and Rao, G. V., "Large Amplitude Supersonic Flutter of Panels Elastically Restrained Against Rotation," Computer and Structures, Vol. 11, 1980. pp. 197-201.

[46] Mei, C. and Weidman, D. J., "Nonlinear Panel Flutter – A Finite Element Approach," Computational Method for Fluid-Structure Interaction Problems, AMP-Vol. 26, Ed. By T. Belytsechke and T. L. Geers, ASME, New York, 1977, pp. 944-951.

[47] Mei, C. and Wang, H. C., "Finite Element Analysis of Large Amplitude Supersonic Flutter of Panels," Proceedings of International Conference on Finite Element Methods, Shanghai, China, Gordon and Breach Science Publishers, Inc., 1982, pp.944-951.

[48] Han, A. D., and Yang, T. Y., "Nonlinear Panel Flutter using High Order Triangular Finite Element," *AIAA Journal*, Vol. 21, No. 10, 1983, pp. 1453-1461.

[49] Xue, D. Y., "A Finite Element Frequency Domain Solution of Nonlinear Panel Flutter with Temperature Effects and Fatigue Life Analysis," Ph.D. Dissertation, Old Dominion University, Norfolk, VA, October 1991.

[50] Xue, D. Y., and Mei, C., "Finite Element Nonlinear Panel Flutter with Arbitrary Temperatures in Supersonic Flow," *AIAA Journal*, Vol. 31, No.1, 1993, pp. 154-162.

[51] Dixon, I. R., and Mei, C., "Finite Element Analysis of Large Amplitude Panel flutter of Thin Laminates," *AIAA Journal*, Vol. 31, No. 4, 1993, pp. 701-707.

[52] Green, P. D. and Killey, A., "Time Domain Dynamic Finite Element Modeling in Acoustic Fatigue Design," in: Proc. 6th International Conference on Structural Dynamics, ISVR, 1997, pp.1007-1026.

[53] Robinson, J. H., "Finite Element Formulation and Numerical Simulation of the Large Deflection Random Vibration of Laminated Composite Plates," MS Thesis, Old Dominion University, 1990.

[54] Zhou, R. C., Xue, D. Y., and Mei, C., "Finite Element Time Domain-Modal Formulation for Nonlinear Flutter of Composite Panels," AIAA Journal, Vol. 32, No. 10, 1994, pp. 2044-2052.

[55] McIntosh, S. C., Jr., "Effect of Hypersonic Nonlinear Aerodynamic Loading on Panel Flutter," AIAA Journal, Vol. 11, No. 1, 1973, pp. 29-32.

[56] Eastep, F. E. and McIntosh, S. C., Jr., "Analysis of Nonlinear Panel Flutter and Response under Random Excitation or Nonlinear Aerodynamic Loading," AIAA Journal, Vol. 9, No. 3, 1971, pp. 411-418.

[57] Gray, C. E., Jr., and Mei, C., "Finite Element Method for Large-Amplitude Two-Dimensional Panel Flutter at Hypersonic Speeds," AIAA Journal, Vol. 29, No. 2, 1991, pp. 290-298.

[58] Bein, T., Friedmann, P., Zhong, X., and Nydick, I., "Hypersonic Flutter of a Curved Shallow Panel with Aerodynamic Heating," AIAA 93-1318, 34th Structures, Structural Dynamics and Materials Conference, La Jolla, CA, 1993.

[59] Nydick, I., Friedmann, P. P. and Zhong, X., "Hypersonic Panel Flutter Studies on Curved Panels," 36th Structures, Structural Dynamics and Materials Conference, New Orleans LA, 1995, pp. 2995-3011.

[60] Thuruthimattam, B. J., Friedmann, P. P., McNamara, J. J. and Powell, K. G., "Aeroelasticity of a Generic Hypersonic Vehicle," AIAA 2002-1209, 43rd Structures, Structural Dynamics and Materials Conference, Denver, Colorado, April 22-25, 2002.

[61] Chandiramani, N. K., Plaut, R. H., and Librescu, L. I., "Nonperiodic Flutter of a Buckled Composite Panel," Sādhanā, Vol. 20, Parts 2-4, 1995, pp. 671-689. Also, "Nonlinear Flutter of a Buckled Shear Deformable Composite Panel in a High-supersonic Flow," International Journal of Non-Linear Mechanics, Vol. 30, No. 2, 1995, pp. 149-167.

[62] Chandiramani, N. K. and Librescu, L. I., "Flutter of Geometrically-Imperfect Shear-Deformable Laminated Flat Panels Using Non-Linear Aerodynamics," Journal of Sound and Vibration, 192(1), 1996, pp. 79-100.

[63] Sri Namachchivaya, N. and Lee, A., "Dynamics of Nonlinear Aeroelastic Systems," Symposium of Fluid-Structure Interaction, Aeroelasticity, Flow-Induced Vibration and Noise, Vol. III, Dallas, TX, ASME, 1997, pp. 165-174.

[64] Chen, P. C. and Liu, D. D., "A Harmonic Gradient Method for Unsteady Supersonic Flow Calculations," Journal of Aircraft, Vol. 22, No. 5, 1985, pp. 371-379.

[65] Chavez, F. R., and Liu, D. D., "Unsteady Unified Hypersonic/Supersonic Method for Aeroelastic Applications Including Wave/Shock Interaction," AIAA Journal, Vol. 33, No. 6, 1995, pp. 1090-1097.

[66] Liu, D. D., Yao, Z. X., Sarhaddi, D., and Chavez, F. R., "From Piston Theory to a Unified Hypersonic-Supersonic Lifting Surface Method," Journal of Aircraft, Vol. 34, No. 3, 1997, pp. 304-312.

[67] Goldstein, M. E., "Boundary-Layer Effect in Panel Flutter," AIAA Journal, Vol. 13, No. 9, 1975, pp. 1247-1249.

[68] Muhlstein, L., Jr., Gaspers, P. A., Jr., and Riddle, D. W., "An Experimental Study of the Turbulent Boundary Layer on Panel Flutter," NASA-TN-D-4486, 1968.

[69] Gaspers, P.A., Jr., Muhlstein, L., Jr., and Petroff, D. N., "Further Experimental Results on the Influence of the Turbulent Boundary Layer on Panel Flutter," NASA-TN-D-5798, May, 1970.

[70] Gordnier, R. E. and Visbal, M. R., "Development of a Three-Dimensional Viscous Aeroelastic Solver for Nonlinear Panel Flutter," AIAA 2000-2337, Fluids 2000 Conference and Exhibit, Denver, CO, June 19-22, 2000.

[71] Gordnier, R. E. and Visbal, M. R., "Computation of Three-Dimensional Nonlinear Panel Flutter," AIAA 2001-0571, 39th AIAA Aerospace Sciences Meeting & Exhibit, Reno, NV, 8-11 January, 2001.

[72] Crandall, S. H. and Zhu, W. Q., "Random Vibration: A Survey of Recent Developments," Journal of Applied Mechanics, Transactions of the ASME 50th Anniversary, Vol. 50, 1983, pp. 953-962.

[73] Selvam, R. P., Qu, Z. and Zheng, Q., "Three-Dimensional Nonlinear Panel Flutter at Supersonic Euler Flow," AIAA 2002-1485, 43rd AIAA/ASME/ASCE/AHS/ASC Structures, Structural Dynamics, and Materials Conference, Denver, Co, April 2002.

[74] Yang, T. Y. and Han, A. D., "Flutter of Thermally Buckled Finite Element Panels," *AIAA Journal*, Vol. 14, No. 7, 1976, pp. 975-977.

[75] Xue, D. Y. and Mei, C., "Finite Element Nonlinear Flutter and Fatigue Life of Two-Dimensional Panels with Temperature Effects," *Journal of Aircraft*, Vol. 30, No. 6, 1993, pp. 993-1000.

[76] Liaw, D. G., "Nonlinear Supersonic Flutter of Laminated Composite Plates Under Thermal Loads," *Computers & Structures*, Vol. 65, No.5, 1997, pp. 733-740.

[77] Lorenz, E. N., "Deterministic Non-periodic Flow," Journal of Atmosphere Sciences, Vol. 20, 1963, pp. 103-141.

[78] Alligood, K. T., Sauer, T. D., and Yorke, J. A., "Chaos: An Introduction to Dynamic Systems", Springer-Verlag New York Inc., 1996.

[79] Moon, F. C., "Chaotic and Fractal Dynamics-An Introduction for Applied Scientists and Engineers," John Wiley & Sons, Inc., 1992.

[80] Thompson, J. M. T. and Stewart H. B., "Nonlinear Dynamics and Chaos," John Wiley and Sons Ltd., 1986.

[81] Thompson, J. M. T. and Bishop, S. R., "Nonlinearity and Chaos in Engineering Dynamics," John Wiley and Sons Ltd., 1994.

[82] Hilborn, R. C., "Chaos and Nonlinear Dynamics," Oxford University Press Inc., New York, 2000.

[83] Moon, F. C., and Holmes, P., "A Magnetoelastic Strange Attractor," *Journal of Sound and Vibration*, Vol. 65, No. 2, 1979, pp. 275-296.

[84] Moon, F. C., "Experiments on Chaotic Motions of a Forced Nonlinear Oscillator: Strange Attractors," *Journal of Applied Mechanics*, Vol. 47, No. 3, 1980, pp. 638-644.

[85] Holmes, P., and Moon, F. C., "Strange Attractors and Chaos in Nonlinear Mechanics," *Journal of Applied Mechanics*, Vol. 50, No. 5, 1983, pp. 1021-1032.

[86] Brunsden, V., Cortell, J., and Holmes, P., "Power Spectra of Chaotic Vibration of a Buckled Beam," *Journal of Sound and Vibration*, Vol. 130, No. 1, 1989, pp. 1-25.

[87] Gottwald, J., Virgin, L. N., and Dowell, E. H., "Experimental Mimicry of Duffing's Equation," *Journal of Sound and Vibration*, Vol. 158, No. 3, 1992, pp. 447-467.

[88] Dowell, E. H. and Ilgamov, M., "Studies in Nonlinear Aeroelasticity," Springer-Verlag, New York, 1988.

[89] Dowell, E. H., "Flutter of a Buckled Plate as an Example of Chaotic Motion of a Deterministic Autonomous System," *Journal of Sound and Vibration*, Vol. 85, No. 3, 1982, pp. 333-344.

[90] Dowell, E. H., "Observation and Evolution of Chaos in an Autonomous System," Journal of Applied Mechanics, Vol. 51, 1984, pp. 664-673.

[91] Virgin, L. N. and Dowell, E. H., "Non-linear Aeroelascity and Chaos," In: Computational Non-linear Mechanics in Aerospace Engineering, Atluri, S. H. (Ed), AIAA, Washington DC, 1992, pp. 531-536.

[92] Mittelmann, H. D. and Weber, H., "Bifurcation Problems and their Numerical Solutions," Birkhäuser Verlag Basel, Germany, 1980.

[93] Bruter, C. P., Aragonal, A. and Lichnerowicz, A., "Bifurcation Theory, Mechanics and Physics," D. Reidel Publishing Company, AA Dordrecht, Holland, 1983.

[94] Chen, Y. and Leung, A. Y. T., "Bifurcation and Chaos in Engineering," Springer-Verlag London Limited, London, Great Britain, 1998.

[95] Holmes, P. J., "Bifurcations to Divergence and Flutter in Flow-induced Osillators: A Finite Dimensional Analysis," Journal of Sound & Vibration, Vol. 53, 1977, pp.471-503.

[96] Holmes, P. and Marsden, M., "Bifurcations to Divergence and Flutter in Flow-induced Oscillators: An Infinite Dimensional Analysis," Automatica, Vol. 14, 1978, pp. 367-384.

[97] Bolotin,V. V., Grishko, A. A., Kounadis, A. N., and Gantes, C. J., "Nonlinear Panel Flutter in Remote Post-Critical Domains," International Journal of Nonlinear Mechanics, Vol. 33, No. 5, 1998, pp. 753-764.

[98] Schuster, H. G., "Deterministic Chaos," VCH Verlagsgesellschaft mbH. D-69451 Weinheim (Federal Republic of Germany), 1995.

[99] Shimada, I. and Nagashima, T., "A Numerical Approach to Ergodic Problem of Dissipative Dynamical System," Progress of Theoretical Physics, Vol. 61, No. 6, 1979, pp. 1605-1616.

[100] Benettin, G., Galgani, L., Giorgilli, A. and Strelcyn, J.-M., "Lyapunov Characteristic Exponents for Smooth Dynamical Systems and for Hamiltonian Systems; A Method for Computing All of Them. Part I: Theory," Meccanica, Vol. 15, 1980, pp. 9-20.

[101] Benettin, G., Galgani, L., Giorgilli, A. and Strelcyn, J.-M., "Lyapunov Characteristic Exponents for Smooth Dynamical Systems and for Hamiltonian Systems; A Method for Computing All of Them. Part II: Numerical Application," Meccanica, Vol. 15, 1980, pp. 21-30.

[102] Wolf, A., Swift, J. B., Swinney, H. L. and Vastano, J. A., "Determining Lyapunov Exponents from a Time Series," Physica, 16D, 1985, pp. 285-317.

[103] Abarbanel, H. D. I., Brown, R. and Kennel, M. B., "Lyapunov Exponents in Chaotic Systems: Their Importance and Their Evaluation Using Observed Data," International Journal of Modern Physics B, Vol. 5, No. 9, 1991, pp. 1347-1375.

[104] Pezeshki, C. and Dowell, E. H., "Generation and Analysis of Lyapunov Exponents for the Buckled Beam," International Journal of Non-Linear Mechanics, Vol. 24, No. 2, 1989, pp. 79-97.

[105] Tang, D. M. and Dowell, E. H., "On the Threshold Force for Chaotic Motions for a Forced Buckled Beam," Journal of Applied Mechanics, Transactions of the ASME, Vol. 55, March 1988, pp. 190-196.

[106] Fermen-Coker, M. and Johnson, G. E., "Thermal Effects on Chaotic Vibrations of Plates," AIAA Journal, Vol. 37, No. 12, 1999, pp. 1544-1550.

[107] Kaplan, J. and Yorke, J., "Chaotic Behavior of Multi-dimensional Difference Equations," in: Functional Differential Equations and the Approximation of Fixed Points,

Lecture Notes in Mathematics, Vol. 730, H. O. Peitgen and H. O. Walther, eds., Springer, Berlin, 1978.

[108] Meirovitch, L., "Elements of Vibration Analysis," McGraw-Hill Inc., 1986.

[109] von Karman, T., "Festigkeitsprobleme in Maschinenbau," Encyclopädie der Mathematischen Wissenschaften, Vol. 3, (P. R. Halmos, Ed.), American Mathematical Society, pp. 211-385.

[110] Moorthy, J., "Numerical Simulation of the Nonlinear Response of Composite Plates Under Combined Thermal and Acoustic Loading," Ph.D. Dissertation, Department of Aerospace Engineering, Old Dominion University, December 1994.

[111] Lee, J., "Large-amplitude Plate Vibration in an Elevated Thermal Environment," *Applied Mechanics Reviews*, Vol. 46, No. 11, Part 2, Nov. 1993, pp. S242-S254.

[112] Reddy, J. N., "Mechanics of Laminated Composite Plates: Theory and Analysis," CRC Press Inc., 1997.

[113] Thornton, E. A., "Thermal Structures for Aerospace Applications," American Institute of Aeronautics and Astronautics, Inc., 1996.

[114] Ugural, A. C., "Stresses in Plates and Shells," The McGraw-Hill Compnies, Inc., 1999.

[115] Bathe, K. J., "Finite Element procedures," Prentice Hall, 1996.

[116] Allen, M. B. and Isaacson, E. L., "Numerical analysis for applied science," Wiley-Interscience, 1997.

[117] Shi, Y., Lee, R. Y. Y., and Mei, C., "Thermal Postbuckling of Composite Plates Using the Finite Element Modal Coordinate Method," *Journal of Thermal Stresses*, Vol. 22, 1999, pp. 595-614.

[118] Guckeheimer, J., and Holems, P., "Nonlinear Oscillations, Dynamical Systems and Bifurcation of Vector Fields," Springer-Verlag, New York, 1983.

[119] Abraham, R. H. and Shaw, C. D., "Dynamics: The Geometry of Behavior," Addison-Wesley Publishing, 1992.

[120] Abraham, F. D., Abraham, R. H., and Shaw, C. D., "Dynamical Systems: A Visual Introduction (Science Frontier Express Series)," Dakota Books, 1996.

[121] Hale, J. and Koçak, H., "Dynamics and Bifurcations," Springer-Verlag New York Inc., 1991.

[122] Wiggins, S., "Global Bifurcations and Chaos," Springer-Verlag New York Inc., 1988.

[123] Dowell, E. H., "Nonlinear Oscillations of a Fluttering Plate," AIAA Journal, Vol. 4, No.7, 1966, pp. 1267-1275.

[124] Weiliang, Y. and Dowell, E., "Limit Cycle Oscillation of a Fluttering Cantilever Plate," *AIAA Journal*, Vol. 29, No. 11, 1991, pp. 1929-1936.

[125] Lee, I., Lee, D. -M. and Oh, I. -K., "Supersonic Flutter Analysis of Stiffened Laminated Plates Subject to Thermal Load," *Journal of Sound and Vibration*, 224(1), 1999, pp. 49-67.

[126] Abdel-Motagaly, K., Chen, R. and Mei, C., "Nonlinear Flutter of Composite Panels Under Yawed Supersonic Flow Using Finite Elements," *AIAA Journal*, Vol. 37, No. 9, 1999, pp. 1025-1032.

[127] Cheng, G., Lee, Y. Y. and Mei, C., "Flow Angle and Temperature Effects on Stability Boundary of Supersonic Panel Flutter", tentatively scheduled for appear in Journal of Aircraft, January/February issue, 2003.

[128] Cheng, G., Mei, C. and Chen, R., "A Methodology for Supersonic Panel Flutter Analysis of TPS Seals", Journal of Aircraft, Vol. 38, No. 6, 2001, pp. 1025-1031.

[129] Blosser, M. L., Chen, R. R., Schmidt, I. H., Dorsey, J. T., Poteet, C. C., and Bird, R. K., "Advanced Metallic Thermal Protection System Development," AIAA 2002-0504, 40th Aerospace Sciences Meeting and Exhibit, Reno, Nevada, 14-17 January, 2002.

APPENDIX A

DISPLACEMENT FUNCTIONS FOR BFS PLATE ELEMENT

A BFS plate element (refer to section 2.2.1) has a total of 24 nodal DOFs including 16 transverse bending related DOFs and 8 in-plane DOFs. The DOFs were illustrated in Fig. 2.2. At an arbitrary point in the element, the transverse displacement, w, and the in-plane movements, u and v, can be interpolated from the nodal bending, in-plane displacements through bi-cubic and bi-linear interpolation functions as:

$$
\begin{aligned}
w = &\, a_1 + a_2 x + a_3 y + a_4 x^2 + a_5 xy + a_6 y^2 + a_7 x^3 + a_8 x^2 y + a_9 xy^2 + a_{10} y^3 \\
&+ a_{11} x^3 y + a_{12} x^2 y^2 + a_{13} xy^3 + a_{14} x^3 y^2 + a_{15} x^2 y^3 + a_{16} x^3 y^3
\end{aligned}
\tag{A.1}
$$

$$
u = b_1 + b_2 x + b_3 y + b_4 xy
\tag{A.2}
$$

$$
v = b_5 + b_6 x + b_7 y + b_8 xy
\tag{A.3}
$$

Define the generalized coordinates as

$$
\{a\} = (a_1 \quad a_2 \quad a_3 \quad a_4 \quad a_5 \quad a_6 \quad a_7 \quad a_8 \quad a_9 \quad a_{10} \quad a_{11} \quad a_{12} \quad a_{13} \quad a_{14} \quad a_{15} \quad a_{16})^T
$$

$$
\tag{A.4}
$$

$$
\{b\} = (b_1 \quad b_2 \quad b_3 \quad b_4 \quad b_5 \quad b_6 \quad b_7 \quad b_8)^T
\tag{A.5}
$$

Then Eqs. (A.1) ~ (A.2) can be rewritten as

$$
\begin{aligned}
w = &(1 \quad x \quad y \quad x^2 \quad xy \quad y^2 \quad x^3 \quad x^2 y \quad xy^2 \quad y^3 \quad x^3 y \quad x^2 y^2 \quad xy^3 \quad x^3 y^2 \quad x^2 y^3 \quad x^3 y^3)\{a\} \\
= &[H_w(x,y)]_{1 \times 16}\{a\}_{16 \times 1}
\end{aligned}
\tag{A.6}
$$

$$
\begin{aligned}
u &= [1 \quad x \quad y \quad xy \quad 0 \quad 0 \quad 0 \quad 0]\{b\} \\
&= [H_u]_{1 \times 8}\{b\}_{8 \times 1}
\end{aligned}
\tag{A.7}
$$

$$
\begin{aligned}
v &= [0 \quad 0 \quad 0 \quad 0 \quad 1 \quad x \quad y \quad xy]\{b\} \\
&= [H_v]_{1 \times 8}\{b\}_{8 \times 1}
\end{aligned}
\tag{A.8}
$$

From Eq. (A.6), the other three bending related displacements, $w_{,x}$, $w_{,y}$ and $w_{,xy}$, at the arbitrary point can be evaluated as

$$w_{,x} = \frac{\partial}{\partial x}[H_w(x,y)]\{a\} \tag{A.9}$$

$$w_{,y} = \frac{\partial}{\partial y}[H_w(x,y)]\{a\} \tag{A.10}$$

$$w_{,xy} = \frac{\partial}{\partial x}\left(\frac{\partial}{\partial y}[H_w(x,y)]\{a\}\right) \tag{A.11}$$

Then, the bending related displacements can be expressed in full form as

$$
\begin{Bmatrix} w \\ w_{,x} \\ w_{,y} \\ w_{,xy} \end{Bmatrix} =
\begin{bmatrix}
1 & x & y & x^2 & xy & y^2 & x^3 & x^2y & xy^2 & y^3 & x^3y & x^2y^2 & xy^3 & x^3y^2 & x^2y^3 & x^3y^3 \\
0 & 1 & 0 & 2x & y & 0 & 3x^2 & 2xy & y^2 & 0 & 3x^2y & 2xy^2 & y^3 & 3x^2y^2 & 2xy^3 & 3x^2y^3 \\
0 & 0 & 1 & 0 & x & 2y & 0 & x^2 & 2xy & 3y^2 & x^3 & 2x^2y & 3xy^2 & 2x^3y & 3x^2y^2 & 3x^3y^2 \\
0 & 0 & 0 & 0 & 1 & 0 & 0 & 2x & 2y & 0 & 3x^2 & 4xy & 3y^2 & 6x^2y & 6xy^2 & 9x^2y^2
\end{bmatrix}
\begin{Bmatrix} a_1 \\ \vdots \\ a_{15} \\ a_{16} \end{Bmatrix} \tag{A.12}
$$

The displacement functions in terms of generalized coordinates, $\{a\}$ and $\{b\}$, applies to any point in the element. Therefore, relationships given in Eqs. (A.7), (A.8), and (A.12) could be applied to the four corner nodes shown in Fig. 2.2. This relates the nodal displacement vector to the generalized coordinates as

$$
\begin{Bmatrix} w_1 \\ w_{1,x} \\ w_{1,y} \\ w_{1,xy} \\ w_2 \\ w_{2,x} \\ w_{2,y} \\ w_{2,xy} \\ w_3 \\ w_{3,x} \\ w_{3,y} \\ w_{3,xy} \\ w_4 \\ w_{4,x} \\ w_{4,y} \\ w_{4,xy} \end{Bmatrix} =
\begin{bmatrix}
1 & 0 & 0 & 0 & 0 & 0 & 0 & 0 & 0 & 0 & 0 & 0 & 0 & 0 & 0 & 0 \\
0 & 1 & 0 & 0 & 0 & 0 & 0 & 0 & 0 & 0 & 0 & 0 & 0 & 0 & 0 & 0 \\
0 & 0 & 1 & 0 & 0 & 0 & 0 & 0 & 0 & 0 & 0 & 0 & 0 & 0 & 0 & 0 \\
0 & 0 & 0 & 0 & 1 & 0 & 0 & 0 & 0 & 0 & 0 & 0 & 0 & 0 & 0 & 0 \\
1 & \bar{a} & 0 & \bar{a}^2 & 0 & 0 & \bar{a}^3 & 0 & 0 & 0 & 0 & 0 & 0 & 0 & 0 & 0 \\
0 & 1 & 0 & 2\bar{a} & 0 & 0 & 3\bar{a}^2 & 0 & 0 & 0 & 0 & 0 & 0 & 0 & 0 & 0 \\
0 & 0 & 1 & 0 & \bar{a} & 0 & 0 & \bar{a}^2 & 0 & 0 & \bar{a}^3 & 0 & 0 & 0 & 0 & 0 \\
0 & 0 & 0 & 0 & 1 & 0 & 0 & 2\bar{a} & 0 & 0 & 3\bar{a}^2 & 0 & 0 & 0 & 0 & 0 \\
1 & \bar{a} & \bar{b} & \bar{a}^2 & \bar{a}\bar{b} & \bar{b}^2 & \bar{a}^3 & \bar{a}^2\bar{b} & \bar{a}\bar{b}^2 & \bar{b}^3 & \bar{a}^3\bar{b} & \bar{a}^2\bar{b}^2 & \bar{a}\bar{b}^3 & \bar{a}^3\bar{b}^2 & \bar{a}^2\bar{b}^3 & \bar{a}^3\bar{b}^3 \\
0 & 1 & 0 & 2\bar{a} & \bar{b} & 0 & 3\bar{a}^2 & 2\bar{a}\bar{b} & \bar{b}^2 & 0 & 3\bar{a}^2\bar{b} & 2\bar{a}\bar{b}^2 & \bar{b}^3 & 3\bar{a}^2\bar{b}^2 & 2\bar{a}\bar{b}^3 & 3\bar{a}^2\bar{b}^3 \\
0 & 0 & 1 & 0 & \bar{a} & 2\bar{b} & 0 & \bar{a}^2 & 2\bar{a}\bar{b} & 3\bar{b}^2 & \bar{a}^3 & 2\bar{a}^2\bar{b} & 3\bar{a}\bar{b}^2 & 2\bar{a}^3\bar{b} & 3\bar{a}^2\bar{b}^2 & 3\bar{a}^3\bar{b}^2 \\
0 & 0 & 0 & 0 & 1 & 0 & 0 & 2\bar{a} & 2\bar{b} & 0 & 3\bar{a}^2 & 4\bar{a}\bar{b} & 3\bar{b}^2 & 6\bar{a}^2\bar{b} & 6\bar{a}\bar{b}^2 & 9\bar{a}^2\bar{b}^2 \\
1 & 0 & \bar{b} & 0 & 0 & \bar{b}^2 & 0 & 0 & 0 & \bar{b}^3 & 0 & 0 & 0 & 0 & 0 & 0 \\
0 & 1 & 0 & 0 & \bar{b} & 0 & 0 & 0 & \bar{b}^2 & 0 & 0 & 0 & \bar{b}^3 & 0 & 0 & 0 \\
0 & 0 & 1 & 0 & 0 & 2\bar{b} & 0 & 0 & 0 & 3\bar{b}^2 & 0 & 0 & 0 & 0 & 0 & 0 \\
0 & 0 & 0 & 0 & 1 & 0 & 0 & 0 & 2\bar{b} & 0 & 0 & 0 & 3\bar{b}^2 & 0 & 0 & 0
\end{bmatrix}
\begin{Bmatrix} a_1 \\ a_2 \\ a_3 \\ a_4 \\ a_5 \\ a_6 \\ a_7 \\ a_8 \\ a_9 \\ a_{10} \\ a_{11} \\ a_{12} \\ a_{13} \\ a_{14} \\ a_{15} \\ a_{16} \end{Bmatrix}
$$

$$\tag{A.13a}$$

or in a brief form

$$\{w_b\} = [T_b]^{-1}\{a\}$$ (A.13b)

For the in-plane nodal displacements

$$
\begin{Bmatrix} u_1 \\ v_1 \\ u_2 \\ v_2 \\ u_3 \\ v_3 \\ u_4 \\ v_4 \end{Bmatrix}
=
\begin{bmatrix}
1 & 0 & 0 & 0 & 0 & 0 & 0 & 0 \\
0 & 0 & 0 & 0 & 1 & 0 & 0 & 0 \\
1 & \bar{a} & 0 & 0 & 0 & 0 & 0 & 0 \\
0 & 0 & 0 & 0 & 1 & \bar{a} & 0 & 0 \\
1 & \bar{a} & \bar{b} & \overline{ab} & 0 & 0 & 0 & 0 \\
0 & 0 & 0 & 0 & 1 & \bar{a} & \bar{b} & \overline{ab} \\
1 & 0 & \bar{b} & 0 & 0 & 0 & 0 & 0 \\
0 & 0 & 0 & 0 & 1 & 0 & \bar{b} & 0
\end{bmatrix}
\begin{Bmatrix} b_1 \\ b_2 \\ b_3 \\ b_4 \\ b_5 \\ b_6 \\ b_7 \\ b_8 \end{Bmatrix}
$$ (A.14a)

or $$\{w_m\} = [T_m]^{-1}\{b\}$$ (A.14b)

Clearly, the generalized coordinates, $\{a\}$ and $\{b\}$, can be expressed in terms of nodal displacements as

$$\{a\} = [T_b]\{w_b\}$$ (A.15)

$$\{b\} = [T_m]\{w_m\}$$ (A.16)

The relationships between nodal displacement vectors and displacement vectors at an arbitrary point can be established by substituting Eqs. (A.15) and (A.16) into Eqs. (A.6) ~ (A.8).

$$w = [H_w][T_b]\{w_b\}$$ (A.17)

$$u = [H_u][T_m]\{w_m\}$$ (A.18)

$$v = [H_v][T_m]\{w_m\}$$ (A.19)

Eqs. (A.17), (A.18), and (A.19) are used in Chapter two as Eqs. (2.4), (2.5), and (2.6), respectively.

APPENDIX B

DETERMINATION OF CRITICAL BUCKLING TEMPERATURE

For an isotropic/symmetrically laminated composite panel with uniform temperature distribution, the governing equations of motion for static thermal buckling can be obtained from Eq. (2.61) by dropping the dynamic terms, aerodynamic terms, and bending-extension coupling terms (because $[B] = 0$):

$$\left(\begin{bmatrix} K_b & 0 \\ 0 & K_m \end{bmatrix} - \begin{bmatrix} K_{N\Delta T} & 0 \\ 0 & 0 \end{bmatrix} + \frac{1}{2} \begin{bmatrix} [N1_{Nm}] & [N1_{bm}] \\ [N1_{mb}] & 0 \end{bmatrix} + \frac{1}{3} \begin{bmatrix} [N2] & 0 \\ 0 & 0 \end{bmatrix} \right) \begin{Bmatrix} W_b \\ W_m \end{Bmatrix} = \begin{Bmatrix} 0 \\ P_{m\Delta T} \end{Bmatrix} \qquad (B.1)$$

Prior to buckling, the panel is flat. That means all nonlinear stiffness matrices due to large bending deformations should vanish. Therefore, Eq. (B.1) can be separated as

$$\left([K_b] - [K_{N\Delta T}] + \frac{1}{2} [N1_{Nm}(W_m)] \right) \{W_b\} = 0 \qquad (B.2)$$

$$[K_m]\{W_m\} = \{P_{m\Delta T}\} \qquad (B.3)$$

Matrix $[N1_{Nm}]$ is a linear function of in-plane displacement $\{W_m\}$, which depends on temperature. The truncated Taylor expansion of the left-hand side of Eq. (B.2) leads to

$$\left([K_b] - [K_{N\Delta T}] + [N1_{Nm}] \right) \{\Delta W_b\} = 0 \qquad (B.4)$$

The eigenanalysis equation to solve for critical temperature is

$$[K_b]\{\Phi_b\} = \mu \left([K_{N\Delta T}] - [N1_{Nm}] \right) \{\Phi_b\} \qquad (B.5)$$

and the critical buckling temperature is

$$\Delta T_{cr} = \mu_1 \Delta T_{ini} \qquad (B.6)$$

where μ_1 is the lowest eigenvalue and ΔT_{ini} is the assumed arbitrary initial temperature.

Eqs. (B.5) and (B.6) are used as Eqs. (3.10) and (3.9) in Chapter Three.

CURRICULUM VITA

for

Guangfeng Cheng

DEGREES:

Doctor of Philosophy (Engineering Mechanics), Old Dominion University, Norfolk,

Virginia, December 2002

Master of Science (Aerospace Engineering), Beijing University of Aeronautics and

Astronautics, Beijing, People's Republic of China, April 1995

Bachelor of Science (Aerospace Engineering), Beijing University of Aeronautics and

Astronautics, Beijing, People's Republic of China, July 1992

PROFESSIONAL CHRONOLOGY:

Department of Aerospace Engineering, Old Dominion University, Norfolk, Virginia

Research Assistant, August 1998 - present

ANSYS Inc., Beijing Office, Beijing, People's Republic of China

Application Engineer, March 1998 - June 1998

Tiger Electronics Corp., Beijing, People's Republic of China

Software Engineer, January 1997 - February 1998

Skyship Software Studio, Beijing, People's Republic of China

Mechanical Engineer, July 1996 – December 1996

No. 11th Institute of CASC, Xi'an, People's Republic of China

Mechanical Engineer, May 1995 – June 1996

SCIENTIFIC AND PROFESSIONAL SOCITIES MEMBERSHIP:

AIAA Student Member

HONORS AND AWARDS:

"Aerospace Engineering Faculty Award," Old Dominion University, Norfolk, Virginia, May 2002

"Old Dominion Honor Scholarship," Old Dominion University, Norfolk, Virginia, 1999-2000.

"Excellent Graduate Student," Beijing University of Aeronautics and Astronautics, Beijing, People's Republic of China, 1993-1994

"Excellent Graduate Student Scholarship," Beijing University of Aeronautics and Astronautics, Beijing, People's Republic of China, 1993-1994.

"Outstanding Student," Beijing University of Aeronautics and Astronautics, Beijing, People's Republic of China, 1990-1991.

"Ren-Min Scholarship," Beijing University of Aeronautics and Astronautics, Beijing, People's Republic of China, 1990-1991.

"Ren-Min Scholarship," Beijing University of Aeronautics and Astronautics, Beijing, People's Republic of China, 1989-1990.

SCHOLARLY ACTIVITIES COMPLETED:

1. G. F. Cheng, "Computer Aided Turbo-pump Reliability Analysis and Evaluation System," M. S. thesis, April 1995.

2. G. F. Cheng, C. Mei and R. Chen, "A Methodology for Supersonic Panel Flutter Analysis of TPS Seals," Journal of Aircraft, Vol. 38, No. 6, 2001, pp. 1025-1031.

Also presented at the 41st AIAA/ASME/ASCE/AHS/ASC Structures, Structure Dynamics, and Materials Conference, Atlanta, GA, 3-6 April 2000.

3. G. F. Cheng, C. Mei and R. Y. Y. Lee, "Large Amplitude Vibration of a Cantilever Beam with Tip Mass Under Random Base Excitation," Advances in Structural Engineering - An International Journal, Vol. 4, No. 4, 2001, pp. 203-209. Also presented at the 42nd AIAA/ASME/ASCE/AHS/ASC Structures, Structure Dynamics, and Materials Conference, Seattle, WA, April 16-19, 2001.

4. Y. Y. Lee, K. K. Yuen, C. F. Ng and G. F. Cheng, "Numerical Simulation Model of Vibration Responses of Rectangular Plates Embedded with Piezoelectric Actuators," Thin-Walled Structures, 40, 2002, pp. 1-28.

5. G. F. Cheng, Y. Y. Lee and C. Mei, "Flow Angle and Temperature Effects on Stability Boundary of Supersonic Panel Flutter," tentatively scheduled for appear in Journal of Aircraft, Vol. 39, No. 4, July-August 2002.

6. G. F. Cheng, Y. Y. Lee and C. Mei, "Nonlinear Random Response of Internally Hinged Beams," accepted for publication in Finite Elements in Analysis and Design.